ORNL/TM-12943

ornl

OAK RIDGE NATIONAL LABORATORY

LOCKHEED MARTIN

High-Temperature Mechanical Performance of a Hot Isostatically Pressed Silicon Nitride

A. A. Wereszczak, M. K. Ferber, and M. G. Jenkins

with contributions from

C.-K. J. Lin, K. Breder, and T. P. Kirkland

MANAGED BY
LOCKHEED MARTIN ENERGY SYSTEMS, INC.
FOR THE UNITED STATES
DEPARTMENT OF ENERGY

UCN-14613 (3-95)

ORNL/TM-12943

Metals and Ceramics Division

HIGH-TEMPERATURE MECHANICAL PERFORMANCE OF A HOT ISOSTATICALLY PRESSED SILICON NITRIDE

A. A. Wereszczak, M. K. Ferber, and M. G. Jenkins

with contributions from

C.-K. J. Lin, K. Breder, and T. P. Kirkland

Date Published: January 1996

Prepared for the
Ceramic Technology Project of the Propulsion Systems Materials Program
Office of Transportation Technologies
Assistant Secretary for Energy Efficiency and Renewable Energy
U.S. Department of Energy
EE 51 05 00 0

Prepared by the
OAK RIDGE NATIONAL LABORATORY
Oak Ridge, Tennessee 37831-6285
managed by
LOCKHEED MARTIN ENERGY RESEARCH CORP.
for the
U.S. DEPARTMENT OF ENERGY
under contract DE-AC05-96OR22464

SUMMARY

A program sponsored by the U.S. Department of Energy's Office of Transportation Technologies was initiated to generate high-temperature mechanical data on a silicon nitride ceramic and to contribute to existing data bases for gas turbine rotor development and implementation. The high-temperature strength, creep, dynamic, and cyclic fatigue resistance of hot isostatically pressed (HIPed) PY6 silicon nitride, manufactured by GTE Laboratories, Incorporated, Waltham, Massachusetts, was characterized and examined. PY6 silicon nitride is similar to other HIPed silicon nitrides that are currently available and being considered for advanced gas turbine engine applications. Significant findings were obtained and include the following:

- The tensile strength of the PY6 exhibited little temperature sensitivity for temperatures below 1000°C. However, the strength decreased sharply at temperatures above 1000°C.
- The stress dependencies of the creep rates measured at 1250 and 1370°C were consistent with a diffusional creep mechanism accompanied by cavitation, grain separation by viscous flow, and grain boundary sliding.
- The tensile fatigue data revealed two distinct failure mechanisms. At 1150°C, failure was controlled by a slow crack growth (SCG) mechanism. At 1260 and 1370°C, the accumulation of creep damage in the form of grain boundary cavities dominated the fatigue behavior. Oxidation appeared to play a significant role in the damage accumulation process.
- Two existing lifetime prediction analyses were modified to enhance their predictive capabilities for PY6. A modified Monkman-Grant relationship was developed that acknowledges and predicts temperature dependence of the relationship between time to failure and minimum creep rate (i.e., temperature-dependent stratification). The Sherby-Dorn temperature-compensated time-to-failure and minimum creep rate parameters were obtained using a bilinear fit of the data. Predictions of time to failure and minimum creep rate at 1200°C were found to be quite good.
- Dynamic fatigue results showed that the fatigue susceptibility of PY6 increased with temperature in the range of 1150 to 1370°C. Comparison of effective time to failure and microstructural observations indicated that static and dynamic fatigue results at 1150°C can be correlated in terms of an SCG model. A transition in the fatigue failure mechanism from SCG to creep rupture appeared to occur at stressing rates $\leq 10^{-2}$ MPa/s for 1260 and 1370°C.
- Comparison of stress-life relations between static and cyclic fatigue indicated that cyclic loading provided increased lifetime for PY6 at 1150 to 1370°C. The tensile static and

cyclic fatigue data could not be described by a universal SCG model at temperatures ≥1150°C. Caution is advised in applying the SCG model to predict the stress-life relation for cyclic fatigue based on static fatigue data. This is especially pertinent at elevated temperatures where mechanisms other than SCG, such as creep properties, visoelastic effects, and oxidation, may contribute to the final failure.

- Cyclic loading of PY6 at elevated temperatures generated failures whose kinetics could not be interpreted in terms of static test. Unloading appeared to play a significant role in extending the time to failure for cyclic fatigue over static fatigue under the same maximum applied stress. The act of unloading could inhibit development of creep damage or retard accumulation of creep deformation resulting from the relaxation of local stress concentration and recovery of viscoelastic grain.
- The flexure strength of PY6 significantly decreased with decreasing stressing rates in ambient air at 1370°C. Fractography showed that a stress-corrosion cracking (SCC) damage zone had formed in the fracture plane on all tested specimens. It was evident that oxidation, and not creep damage, ultimately initiated the formation of an SCC damage zone in PY6 which significantly weakened it. Creep damage was observed on those specimens tested at stressing rates slower than 10^{-1} MPa/s and appeared to exacerbate the already deleterious effects of the stress-oxidation damage zone.
- Flexural dynamic fatigue results suggest that manufacturers of silicon nitride components can greatly reduce the deleterious effects that stem from the formation of SCC by appropriately suppressing oxidation in ambient air.
- Although these observations are for a specific commercial silicon nitride, they are expected to apply to other HIPed silicon nitrides.

CONTENTS

LIST OF FIGURES

LIST OF TABLES

HIGH-TEMPERATURE MECHANICAL PERFORMANCE OF A HOT ISOSTATICALLY PRESSED SILICON NITRIDE

A. A. Wereszczak,† M. K. Ferber,† M. G. Jenkins,†
C.-K. Lin,‡ K Breder,‡ and T. P. Kirkland‡

1. INTRODUCTION

Silicon nitride ceramics are an attractive material of choice for designers and manufacturers of advanced gas turbine engine components for many reasons. These materials typically have potentially high temperatures of usefulness (up to 1400°C), are chemically inert, have a relatively low specific gravity (important for inertial effects), and are good thermal conductors (i.e., resistant to thermal shock). In order for manufacturers to take advantage of these inherent properties of silicon nitride, the high-temperature mechanical performance of the material must first be characterized. The mechanical response of silicon nitride to static, dynamic, and cyclic conditions at elevated temperatures, along with reliable and representative data, is critical information that gas turbine engine designers and manufacturers require for the confident insertion of silicon nitride components into gas turbine engines.

This final report describes the high-temperature mechanical characterization and analyses that were conducted on a candidate structural silicon nitride ceramic. The high-temperature strength, static fatigue (creep rupture), and dynamic and cyclic fatigue performance were characterized. The efforts put forth were part of Work Breakdown Structure Subelement 3.2.1, "Rotor Data Base Generation." PY6 is comparable to other hot isostatically pressed (HIPed) silicon nitrides currently being considered for advanced gas turbine engine applications.

2. APPROACH

The goal of the proposed research program was to systematically study the mechanical performance of a domestic silicon nitride ceramic as a function of stressing condition, temperature, and time in an ambient air environment.

---

*Research sponsored by the U.S. Department of Energy, Assistant Secretary for Energy Efficiency and Renewable Energy, Office of Transportation Technologies, as part of the Ceramic Technology Project of the Propulsion Systems Materials Program, under contract DE-AC05-96OR22464 with Lockheed Martin Energy Research Corp. [Work Breakdown Structure Subelement 3.2.1, "Rotor Data Base Generation"].

†Principal investigators.
‡Contributors.

Stress (creep)-rupture data were generated by measuring time to failure for specimens subjected to static, dynamic, and cyclic stresses. The time-dependent deformation was monitored during testing so that the extent of high-temperature creep could be ascertained. Tested samples were characterized using established ceramographic, scanning electron microscopy (SEM), and transmission electron microscopy (TEM) techniques. A major goal of this effort was to better understand the microstructural aspects of high-temperature failure including:

1. extent of slow crack growth (SCG),
2. evolution of cavitation-induced damage and fracture,
3. transition between brittle crack extension and cavitation-induced crack growth,
4. crack blunting, and
5. the evolution and role of oxidation-assisted damage.

The resulting stress-rupture data were used to examine the applicability of a generalized fatigue-life (SCG) model. Model refinements were implemented to account for both crack blunting and creep damage effects. Once a satisfactory model was developed, separate stress-rupture (confirmatory) experiments were performed to examine the model's predictive capability. Consequently, the data generated in this program provided a needed data base for component utilization in automotive gas turbines and also facilitated the development of a design methodology for high-temperature structural ceramics.

The domestic silicon nitride material tested in this program was PY6, manufactured by GTE Laboratories Incorporated, Waltham, Massachusetts. The silicon nitride material was chosen because it was a candidate rotor material for advanced gas turbine engines, and its development was relatively mature at the time. PY6 is comparable to other HIPed silicon nitrides that are currently being considered for advanced gas turbine engine applications.

3. RESULTS: HIGH-TEMPERATURE MECHANICAL PERFORMANCE

3.1 TESTING BACKGROUND

3.1.1 Material

The processing and development of PY6 are described elsewhere.[1] Briefly, the PY6 silicon nitride is fabricated using ~ 6 wt % yttria as the densification aid. The sintering aid tends to reside at the multigrain junctions, as seen in Figs. 1 and 2. The material used in this

ORNL-PHOTO 10586-95

Fig. 1. Transmission electron microscopy showed that the yttria sintering aid was located primarily at multigrain junctions.

ORNL-PHOTO 10587-95

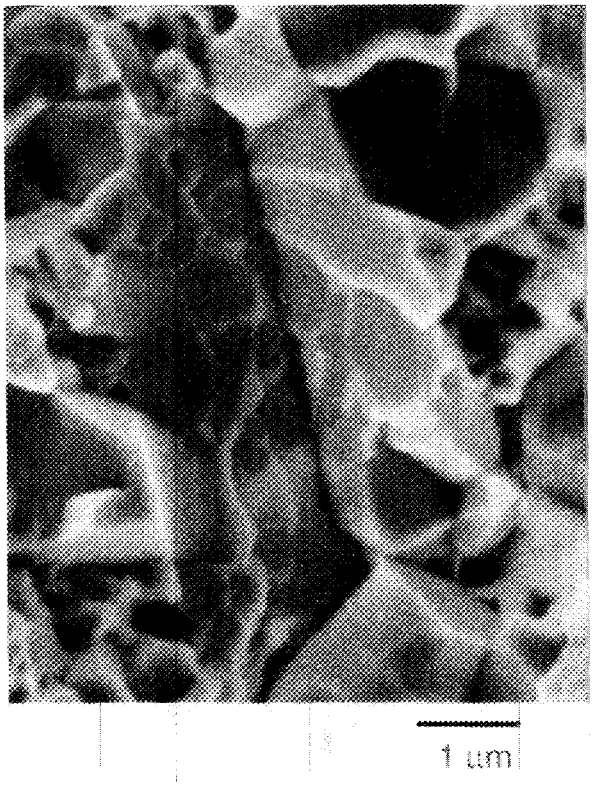

Fig. 2. Scanning electron micrograph of as-received PY6 microstructure.

study was cold isostatically pressed while in its green state and then HIPed at an elevated temperature. It is emphasized that this material was cold isostatically pressed and *not* injection-molded; the injection-molded grade of PY6 has been shown to mechanically perform quite differently at elevated temperatures than the "same" cold isostatically pressed PY6 (ref. 2). The resulting microstructure consisted of 1- to 6-μm-long acicular grains surrounded by equiaxed grains 0.1 to 1.0 μm in diameter. This arrangement leads to a relatively dense microstructure. The silicon nitride grains, which are generally in the form of β-Si_3N_4, are separated by relatively thin layers of an amorphous yttrium silicate. The intergranular phase is also present in the multigrain junctions as a crystalline yttrium silicate [see X-ray diffraction profile in Fig. 3(*a*)], although some specimens did not have a crystalline second phase [see Fig. 3(*b*)]. The specimens that did not possess a crystalline second phase exhibited a poorer high-temperature mechanical performance.[3]

3.1.2 Button-head Tensile Specimen

All button-head tensile specimens were commercially machined to the specifications shown in Fig. 4. The gage section diameter was 6.35 mm, and the gage length was 35 mm. Final machining of the gage section was conducted in a longitudinal orientation to avoid transverse machining damage.

3.1.3 Equipment Used for Tests

Tensile strength evaluation, static creep, dynamic, strain and stress relaxation, and 0.1-Hz tension-tension cyclic fatigue tests were conducted on commercial electromechanical load machines having both load- and strain-control capabilities (Model 1380, Instron Corp., Canton, Massachusetts). The desired load (strain)-time profiles were controlled by trapezoidal function generators. The specimen grips, which were configured for button-head specimens, were located outside the compact two-zone resistance-heated furnaces capable of generating a maximum temperature of 1600°C. The grips were attached to the load frame using hydraulic couplers to minimize bending moments. Oxygen-free copper collets interfaced the upper and lower specimens' button-head radii to the upper and lower grips, respectively; the deformable copper lessened any debilitating stress concentrators associated with the specimen machining. A schematic of the copper collets used is shown in Fig. 5. Specimen displacements were measured over 25-mm gage lengths with direct-contact extensometers employing remote capacitance sensors. A schematic of this arrangement is shown in Fig. 6. By carefully controlling the temperatures of both the measurement hardware and grip cooling

ORNL-DWG95-5926

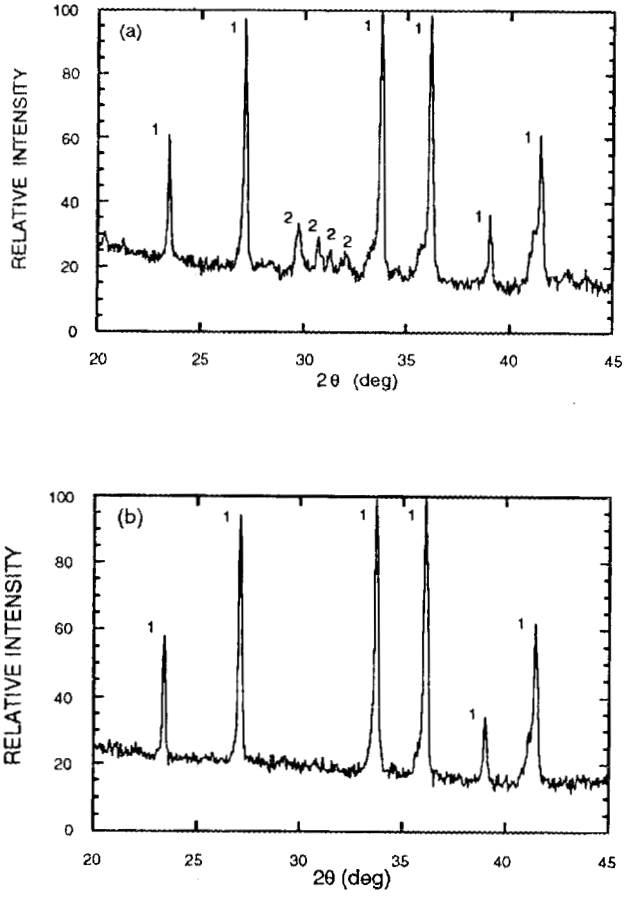

Fig. 3. Most PY6 specimens had (*a*) a crystalline second phase, while (*b*) a few did not (1 = β-Si_3N_4 and 2 = α-$Y_2Si_2O_7$).

ORNL-DWG95-5927

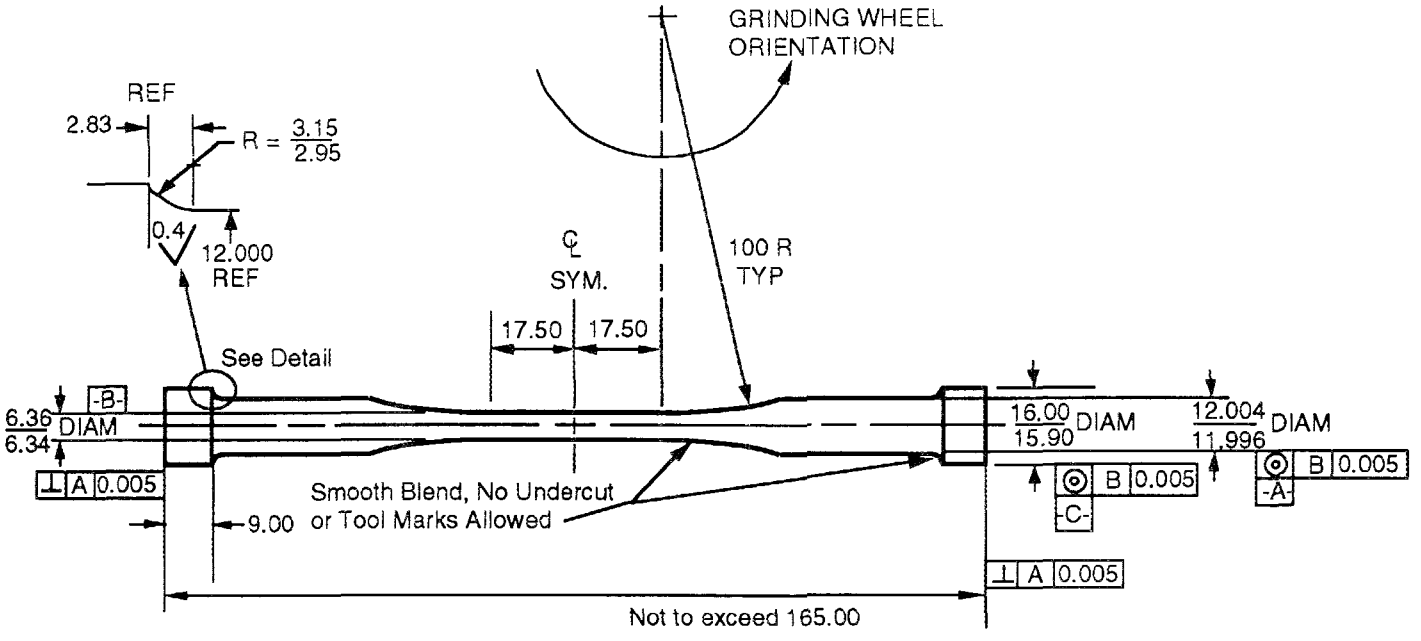

NOTE:
SURFACE FINISH 0.4 ALL OVER
EXCEPT 16.00 DIAM AND
END FACES WHICH CAN BE 0.8

DIMENSIONS IN mm
XX DEC. +/- 0.25
SURF. FINISH IN micrometers

DRAWING MODIFICATION 1C
21 FEBRUARY 1991, M.G. JENKINS

Fig. 4. PY6 Button-head specimens were machined to the dimensions shown. The gage section diameter and length were 6.35 and 35 mm, respectively.

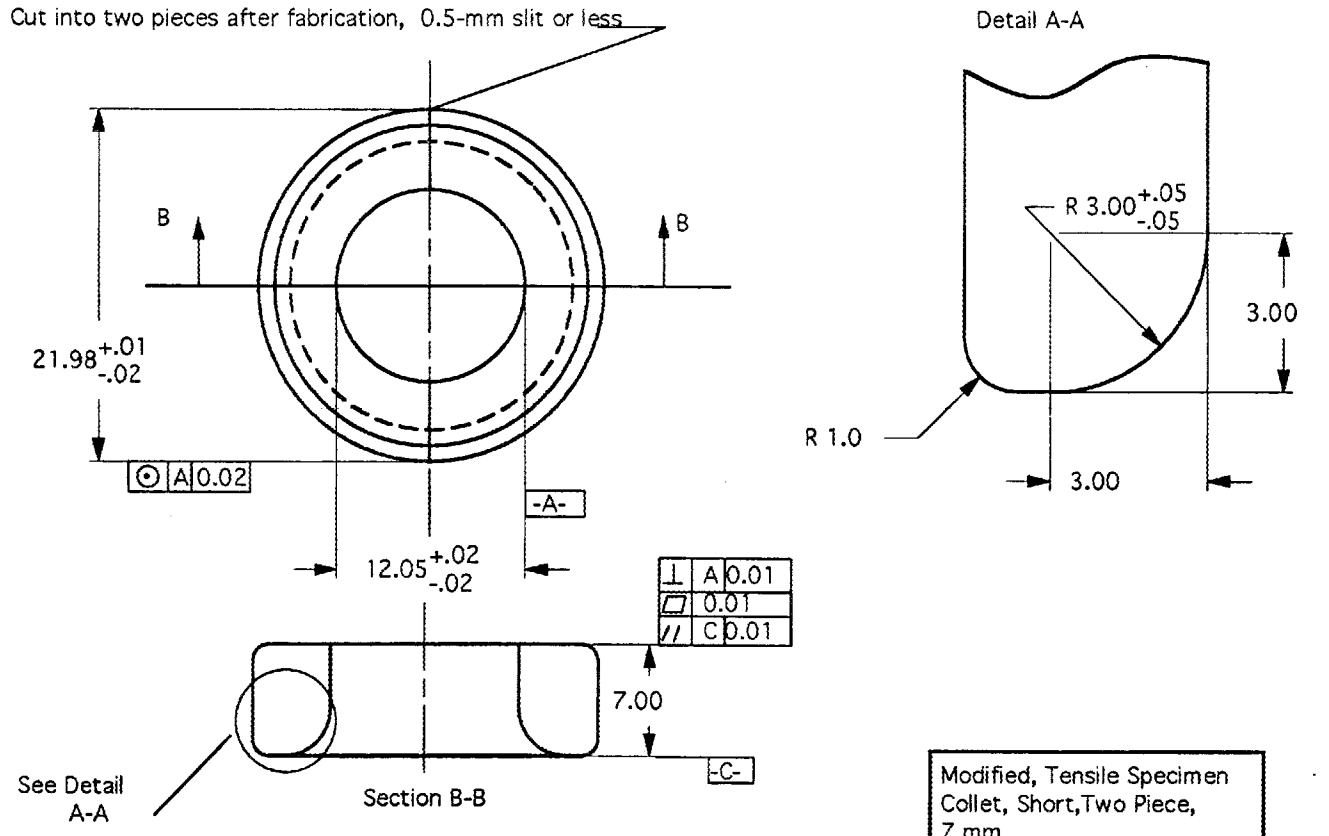

Note: 1) Part must be split at 2 equally spaced places and packaged as a set.
2) Surface finish = 0.5 μm all over.
3) Tolerances and dimensions in mm.
4) Material is oxgen-free copper.
5) After fabrication, vacuum-anneal (10^{-4} Pa) at 800 to 850°C.

Fig. 5. Oxygen-free, copper collets were used for all the tensile tests.

ORNL-DWG95-5929

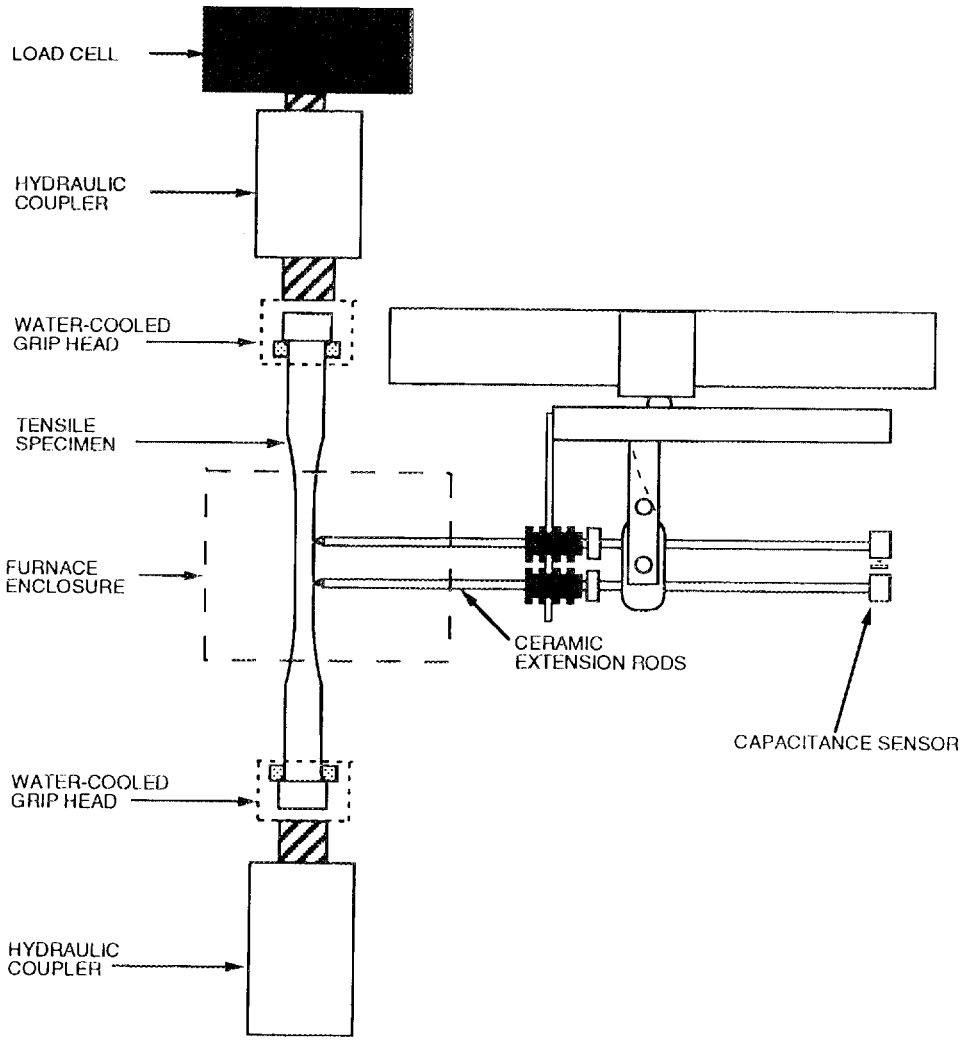

Fig. 6. Schematic diagram of a button-head specimen and the load train system used for all tensile testing.

water, resolutions of ≅ 0.5 μm could be achieved with this arrangement. Personal computers (PCs) and data acquisition systems were used to monitor and store various output signals including displacement, load, load error, and testing temperature. All tests were conducted in ambient air under electronic load control, except the stress relaxation tests, which were conducted in strain control.

Tension-tension cyclic fatigue tests (10 Hz) were conducted on a commercial servohydraulic test machine (Model 8500, Instron Corp, Canton, Massachusetts). The furnace arrangement was the same as that for tests conducted with the electromechanical test machines; however, the specimen gripping was different. The servohydraulic test machine contained adjustable, fixed-grip systems which permitted bending minimization with strain-gaged specimens. Bending was minimized at room temperature, and the strain gages were removed prior to specimen heat-up.

The strength and creep/fatigue flexure tests were conducted using a flexure test facility. This equipment consisted of a load frame capable of separately testing up to three flexure samples concurrently. The test fixtures had inner and outer spans of 20 and 40 mm, respectively. The loads were generated by pneumatically driven air cylinders located at the top of the support frame. The mechanical loads were transmitted into the hot zone of the furnace through SiC rods. A PC monitored the displacement, as well as the load on each specimen, and provided necessary adjustments in the air pressure (via the electropneumatic transducer) such that the desired load (stress) level was maintained. The required test temperature was maintained by a resistance-heated box furnace. The time dependence of the flexural creep deformation was determined by measuring the load-point deformation based upon linear variable differential transformer (LVDT) readings representing the downward movement of the SiC load rams. In order to account for the effects of thermal fluctuations on the displacement data, the front load station in each test frame was "dead" loaded (i.e., specimen removed from fixture). The resulting displacement-time data, which were indicative of the background thermal fluctuations, were used to correct the displacement-time profiles for the two adjacent load stations.

3.2 TENSILE STRENGTH

Table 1 lists the number of tensile and flexure specimens tested and the temperatures used for the strength measurements; flexure strengths were measured to compare with tensile strengths. The stressing rate range for all fast fracture strength tests was 35 to 37 MPa/s. Load-tensile displacement curves were recorded. Least-squares regression of the resulting stress-strain curves was used to determine the elastic modulus for each test.

Table 1. Test matrix for PY6 strength measurements

	Tension		Flexure	
Test type	Temp (°C)	No. Tested	Temp (°C)	No. Tested
Strength	25 1000 1260 1370	26 3 3 2	25 1100 1300 --	49 50 44 --

The temperature dependence of the tensile and flexure strengths (designated S_t and S_{MOR}, respectively) measured for the PY6 material is shown in Fig. 7 (ref. 3). Similar data reported by the University of Dayton Research Institute (UDRI)[4] are included in the graph for comparison. For the room-temperature tensile tests, strain-gaged specimens were used to measure the strain, and least-squares regression of the stress-strain curves yielded an average elastic modulus at room temperature of 305 GPa with a standard deviation of 3.5 Gpa.

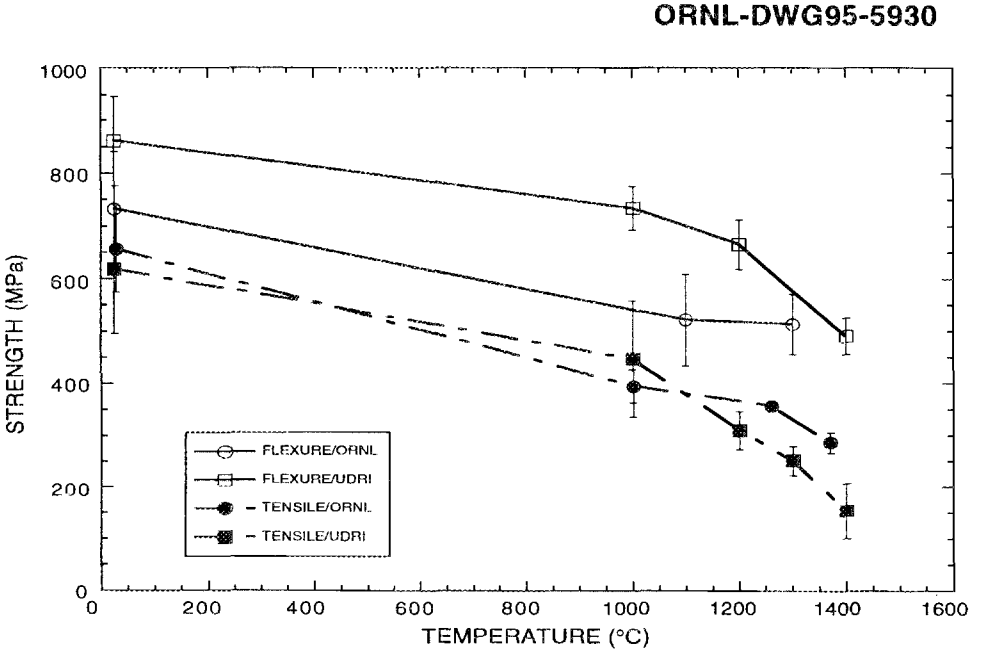

Fig. 7. Tensile and flexure strength of PY6 silicon nitride as a function of temperature.

The strength exhibited a gradual decrease as the temperature was increased to 1000°C. Both S_t and S_{MOR} decreased sharply as the temperature exceeded 1100°C, with the exception of the Oak Ridge National Laboratory (ORNL) flexure data. However, the ORNL flexure strength values increased slightly as the temperature increased from 1100 to 1300°C. This behavior may have been a consequence of enhanced creep-assisted crack blunting in the ORNL flexure specimens due to the high α-Si_3N_4 content in the starting material. The presence of α-Si_3N_4 in the ORNL flexure specimens suggests that the α-to-β transformation was not completed during the HIPing process.

As shown in Fig. 7, S_t was significantly less than S_{MOR} at a given temperature. Considering that the lower tensile strength was a result of either a larger surface area (surface area $\cong$ 80 mm^2 for flexure and 698 mm^2 for tension) or gage section volume (effective volume $\cong$ 2.5 mm^3 for flexure and 1108 mm^3 for tension), it is expected that Weibull statistics would likely describe these strength differences.

3.3 TENSILE STATIC CREEP

3.3.1 Creep and Fatigue Performance

The analysis of creep data is frequently based on steady-state creep rate ($d\varepsilon_S/dt = \dot{\varepsilon}_S$) behavior. For this case, the stress and temperature dependencies of $\dot{\varepsilon}_S$ are acknowledged in the expression:[5,6]

$$\dot{\varepsilon}_S = A_o (\sigma_a/\sigma'_o)^n \exp(-Q_c/RT) \quad , \tag{1}$$

where A_O is a pre-exponential factor, σ_a is the applied stress, σ'_o is a normalizing parameter (i.e., σ'_o = 1 MPa), n is the creep (or stress) exponent, Q_c is the activation energy, R is the universal gas constant, and T is the absolute temperature. Similarly, the fatigue life, t_f, can be described by the equation:[7]

$$t_f = B_o (\sigma_a/\sigma'_o)^{-N} \exp(Q_f/RT) \quad , \tag{2}$$

where N, Q_f, and B_o determine the stress and temperature dependencies of the dominant fatigue mechanism. When failure is controlled by the accumulation of creep damage, t_f is often found to be a unique function of $\dot{\varepsilon}_S$, independent of applied stress and temperature.[8,9] The relationship between t_f and $\dot{\varepsilon}_S$ is described by the Monkman-Grant relation:[10]

$$t_f = C \dot{\varepsilon}_S^{-m} \quad , \tag{3}$$

where C and m are constants. Combining Eqs. (2) and (3) shows that $N = n \bullet m$ for $m \cong 1$ and $Q_c \cong Q_f$.

The mechanical reliability of PY6 was evaluated by measuring the tensile creep and fatigue behavior at 1150, 1200, 1260, and 1370°C. Table 2 lists the number of specimens tested at each temperature and the corresponding number of flexure specimens that were tested as a supplement to the tensile testing.

Table 2. Test matrix for PY6 creep/fatigue measurements

	Tension		Flexure	
Test Type	Temp. (°C)	No. Tested	Temp. (°C)	No. Tested
Creep/Fatigue	1150 1200 1260 1370	5 6 6 10	1150 1200 1260 1370	0 0 4 5

Tensile and flexural creep/fatigue tests of the PY6 material were conducted in the temperature range 1150 to 1370°C. The lowest temperature, 1150°C, is closer to the glass transition temperature of the secondary intergranular phase than the higher two temperatures. It was expected that the fatigue behavior at this temperature would be dominated by SCG since creep damage mechanisms would be limited by lower temperature kinetics. The higher two temperatures, 1260 and 1370°C, were significant as temperatures because they were the design temperatures for the turbine rotor and stator inlet, respectively, for advanced gas turbine engine applications. As will be discussed, there was a failure mode transition between 1150 and 1260°C, so 1200°C testing was chosen for further examination of the failure mode transition and for confirmatory testing. The tensile and flexural creep results in this study were examined to provide insights into the possible differences between compression and tension creep behavior. For a more detailed discussion of the flexure test, see ref. 3. Table 3 summarizes the applied stresses, minimum strain rates, times to failure, and the total strains to failure for all the specimens that were static creep tested.

Table 3. Summary of static creep results

Temp and Specimen I.D.	Stress (MPa)	Minimum strain rate (s^{-1})	Time to failure (h)	Total strain to failure (με)
1150°C				
5S11	225	2.2×10^{-10}	1190*	2450*
3S11	250	1.0×10^{-8}	23	2100
4S11	275	1.8×10^{-7}	2	2180
2S11	287	9.0×10^{-8}	1	1170
1S11	300	2.7×10^{-8}	3	1250
1200°C				
B17	160	4.4×10^{-10}	3806	5500
C2	175	1.5×10^{-9}	596	5890
1S120	165	3.7×10^{-9}	5998*	6920*
4S120	188	1.5×10^{-9}	≅810	≅6000
3S120	200	7.9×10^{-8}	26	1470
2S120	225	1.0×10^{-7}	23	2120
1260°C				
4S12	100	4.9×10^{-10}	2261	6160
6S12	113	1.0×10^{-9}	1750*	8120*
5S12	125	4.7×10^{-9}	502	14200
7S12	138	2.9×10^{-9}	329	6800
8S12	150	3.3×10^{-9}	178	3280
9S12	175	1.6×10	60	8110
1370°C				
5S13	50	5.0×10^{-9}	863	37300
8S13	60	1.7×10^{-8}	230	18930
9S13	62	1.2×10^{-8}	410	28620
4S13	68	2.0×10^{-8}	106	13370
1PH137	68	3.7×10^{-8}	82	15100
7S13	70	9.3×10^{-9}	886	37030
3S13	75	2.6×10^{-8}	90	14180
0S13	85	3.4×10^{-8}	93	19800
2S13	87	4.8×10^{-8}	41	10760
1S13	100	1.5×10^{-7}	8	10070

*Test interrupted; specimen did not creep rupture.

The time and stress dependencies of the tensile creep rates at 1150, 1260, and 1370°C are shown in Figs. 8(*a*)-(*c*), respectively, which were taken from ref. 3. There was a strong primary creep component in the 1260 and 1370°C strain-time curves. The primary creep regime has been attributed to viscoelastic deformation arising from grain boundary sliding accommodated by elastic deformation of grain boundary asperities. In the case of the 1150°C data, the large increase in strain at the onset of the test was due primarily to the elastic strain component (900 to 980 με). A dominant secondary creep region was observed in the strain histories generated at both 1150 and 1260°C. Specimen failure (vertical arrows) marked the end of this steady-state creep. However, at 1370°C, a tertiary creep regime preceded failure. This tertiary creep was attributed to the development of multiple cracks in the gage section.

The 1370°C data exhibited a trend of increasing strain rate with increasing stress. However, the creep curves for the 1260°C tests were somewhat inconsistent. In particular, the data generated at 125 and 150 MPa did not follow the trend of increasing creep strain rate with increasing stress. This behavior, which was also apparent in the strain rate versus stress curves, was found to be a result of specimen-to-specimen variations in the crystallinity of the intergranular phase; see ref. 3 for explanation of this observation. For a given stress level, samples containing an amorphous intergranular phase would be expected to creep at faster rates than samples containing a highly crystallized grain boundary phase.

Figures 9(*a*) and (*b*) show log-log plots of the minimum strain rate, $\dot{\varepsilon}_s$, versus applied stress, σ_a, for tension and flexure, respectively. Note that the stress dependency of the strain rate associated with the 1150°C tests exhibited more variability than that measured at 1260°C. The increased scatter in the 1150°C data was not due to variations in intergranular phase crystallinity but rather a change in failure mechanism due to the lower test temperature.

The n values [see Eq. (1)] calculated for each curve in Fig. 9 using regression analysis were 16.1 at 1150°C, 5.6 at 1260°C, and 4.7 at 1370°C. Based upon microstructural observations as well as results from previous creep studies in the literature (see ref. 3 for more detailed discussion), it is believed that the deformation at 1260 and 1370°C was due to diffusional creep ($n = 1$) accompanied by cavitation, grain separation by viscous flow, and possibly grain boundary sliding. These mechanisms are expected to give a nonlinear stress dependence ($2 < n < 4$). The extremely high value of n measured at 1150°C is indicative of a change in the dominant failure mechanism.

Fig. 8. Creep histories of PY6 silicon nitride at (*a*) 1150, (*b*) 1260, and (*c*) 1370°C.

ORNL-DWG95-5932

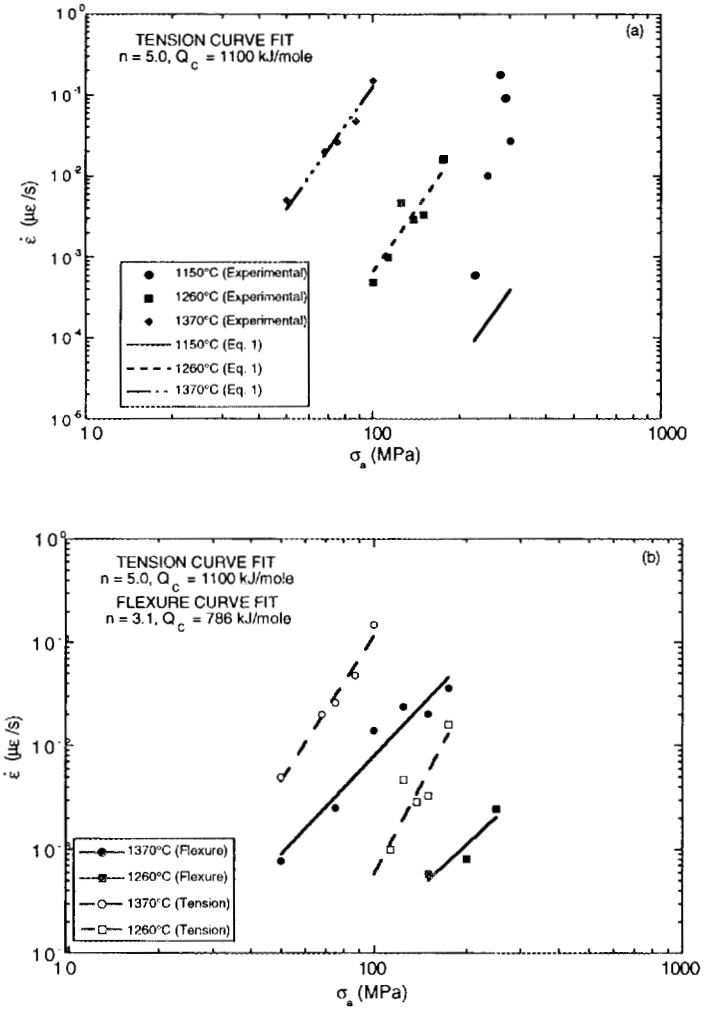

Fig. 9. Stress and temperature dependencies of the minimum creep rate for (*a*) tension and (*b*) flexure.

Values of Q_C and n in Eq. (1) were estimated from a multiple linear regression analysis of the tensile creep data in Fig. 9(*a*). The tensile results obtained at 1150°C were not considered because failure was dominated by a different mechanism. The resulting estimates of n and Q_C for tension were 5.0 and 1102 kJ/mole, respectively. As shown by the solid lines in Fig. 9(*a*), these estimated values provide a satisfactory description of the 1260 and 1370°C tensile data. Activation energies measured for other silicon nitride ceramics are typically in the range of 550 to 700 kJ/mole; see ref. 3 for more detailed discussion.

A series of flexural creep tests were also conducted at 1260 and 1370°C. In order to eliminate the problem of batch-to-batch material variations, all flexural specimens were machined from the as-received tensile rods. Figure 9(*b*) compares the creep rate-stress

dependencies obtained from the tensile and flexure tests. The flexural creep rate was significantly lower than the tensile value at a given stress and temperature. The estimates of n and Q_C were 3.1 and 786 kJ/mole, respectively, which were obtained by fitting the flexural strain rate-stress data in Fig. 9(*b*) to Eq. (1). These values are again significantly lower than their tensile test counterparts. This discrepancy can be attributed to the use of a formulation [see Eq. (32) in Sect. 3.7.1] in the calculation of the flexural creep strains. This formulation considers the creep rate to be independent of the sign of the stress. However, compression and tension creep data for similar silicon nitrides suggest that this assumption is not valid; see ref. 3 for more detailed discussion.

All tensile creep tests were continued until the samples failed in order to examine the fatigue performance. The resulting tensile fatigue relations are shown in Fig. 10. The tensile fatigue exponents [N in Eq. (2)] estimated from linear regression were 18.0 at 1150°C, 6.4 at 1260°C, and 6.0 at 1370°C. The similarity of the creep and fatigue exponents indicates that the failure process is ultimately controlled by the same creep mechanism. This relationship is illustrated by expressing t_f as a function of $\dot{\varepsilon}_S$ [i.e., Eq. (3)]. An application of the tensile data to this relationship is shown in Fig. 11. Note that the data for the 1260 and 1370°C tests fall within a narrow band; this indicates that the dominant fatigue mechanisms were identical for these two temperatures. The failure process probably involved the time-dependent accumulation of creep damage in the form of cavities and facet-size cracks based upon SEM observations; see ref. 3 for more detail. Although the slope of the Monkman-Grant curve at

ORNL-DWG95-5933

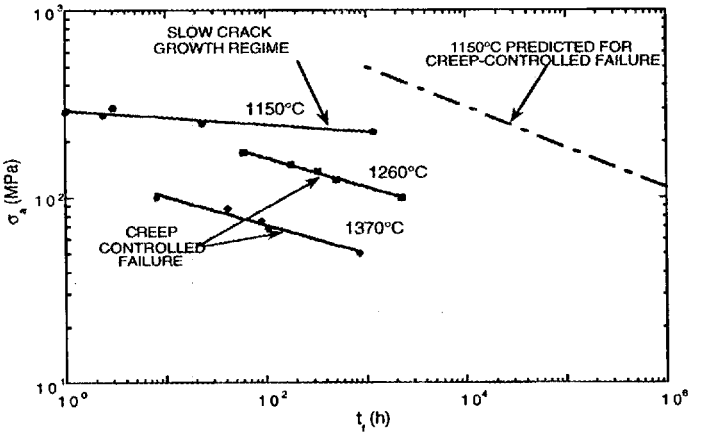

Fig. 10. Static fatigue behavior of PY6 at 1150, 1260, and 1370°C.

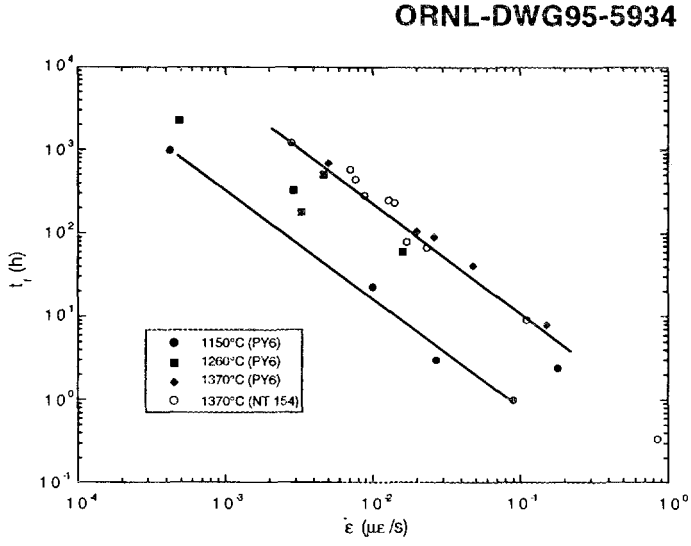

Fig. 11. Fatigue life as a function of creep strain rate.

1150°C was similar to that of 1260 and 1370°C data, it was displaced to a lower fatigue-life regime. While still controlled by the creep rate, this result implies that the fatigue mechanism was altered as the temperature was decreased. The fact that the fracture surfaces at 1150°C showed evidence of SCG indicates that a localized creep crack extension process was responsible for the fatigue behavior.

Values of m were in the range of 0.98 to 1.15 (see Fig. 11) and were relatively independent of temperature. Taking $m \cong 1$ leads to the prediction that $N = n \bullet m \cong n$, which is in agreement with experimental observations. It is interesting to note that the fatigue-life versus strain rate relation recently measured for NT 154 (Norton Company, Northboro, Massachusetts) was quite similar to that for the PY6 implying similar failure mechanisms for both materials at temperatures > 1200°C; see ref. 3 for more detailed discussion.

Optical microscopy of the tensile fracture surfaces revealed a transition in the fracture markings as the test temperature increased from 1150 to 1370°C. This transition is schematically shown in Fig. 12. At 1150°C, the fracture surfaces contained well-defined mirror, mist, and hackle regions. At 1260°C, the fracture surface was characterized by a relatively small creep damage zone (a region of high surface roughness) originating at the gage section surface. At 1370°C, the creep damage zone covered as much as 50% of the fracture surface with the mirror region comprising the rest. The fact that hackle markings were absent indicates that the mirror size exceeded the specimen cross section. The creep damage zone was similar to that observed on surfaces generated at 1260°C in that both cavitation and microcracking were predominate features. In addition, the size of the creep damage zone

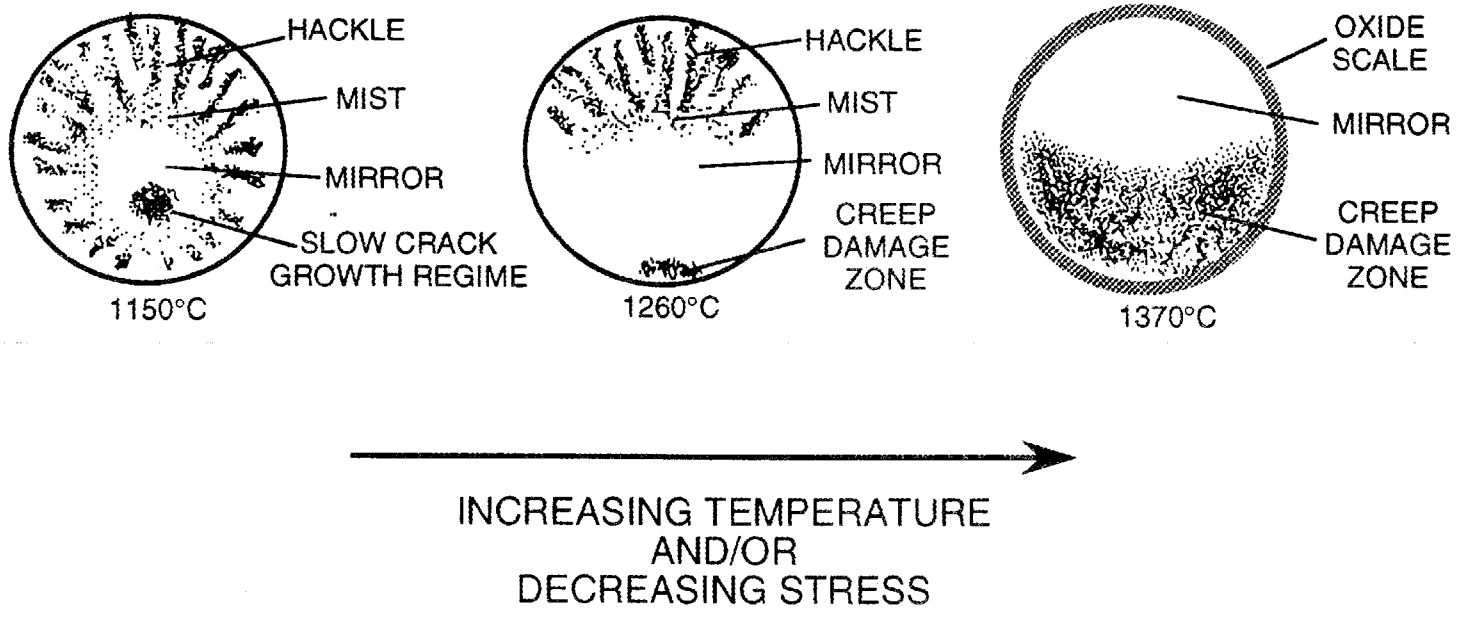

Fig. 12. Schematic diagram showing the transition from fast fracture markings for tests conducted at low temperatures and/or high stresses to creep damage-like markings produced at higher temperatures and/or lower stresses.

increased slightly with decreasing stress indicating a slight stress dependency of the damage accumulation process.

The oxide scale inhibited detailed SEM examination of the cavities observed along the fracture surface of specimens tested at 1260 and 1370°C. However, analogous cavities could be observed by generating a secondary fracture surface parallel to the test fracture surface at room temperature. Extensive cavitation was found along two-grain junctions.[3] These lenticular-shaped cavities were present throughout the gage section volume. Furthermore, the extension of the cavities into the silicon nitride grains suggests that the growth mechanism involved solution/precipitation rather than viscous flow.[3] There was a tendency for the number of cavities in the 1370°C specimens to decrease dramatically as the applied stress was lowered to 50 MPa.

A common feature observed in specimens tested at 1260 and 1370°C was the skeletal pattern of the intergranular phase outlining the interfaces between small grain clusters and a single large grain.[3] The formation of this pattern is believed to be a consequence of grain separation by viscous flow of the boundary phase. Such patterns could lower the local fracture resistance in the intergranular phase thereby providing a preferred failure path for a secondary fracture. This viscous flow process would ultimately lead to the formation of facet-sized microcracks. The absence of extensive creep damage at 1150°C was a consequence of the increased viscosity of the intergranular phase.

3.3.2 Damage Occurring During Static Tests

3.3.2.1 Creep Mechanisms

The accommodated creep deformation in the PY6 at 1260 and 1370°C was most likely controlled by grain boundary diffusion. This mechanism would require the transport of species from the boundaries under compression to those under tension with no net change in volume. The microstructural observations also revealed the presence of unaccommodated creep strain (i.e., creep damage), which resulted from both cavitation and viscous flow between small and large grain interfaces. Although grain boundary sliding is often cited as a deformation mechanism in the creep of silicon nitride, it was not expected to be the dominant or rate-controlling step during the creep of the PY6 material. This conclusion is based on a study by Lange[11] showing that sliding in the presence of a viscous intergranular phase is faster than the rate of grain deformation required to accommodate the sliding. During the first stage of creep, this accommodation is by elastic deformation while for long-term creep, grain deformation will be controlled by either diffusion or viscous flow; see Fig. 13 for examples of these mechanisms. Grain boundary sliding may, however, play a secondary role by

ORNL-PHOTO 10588-95

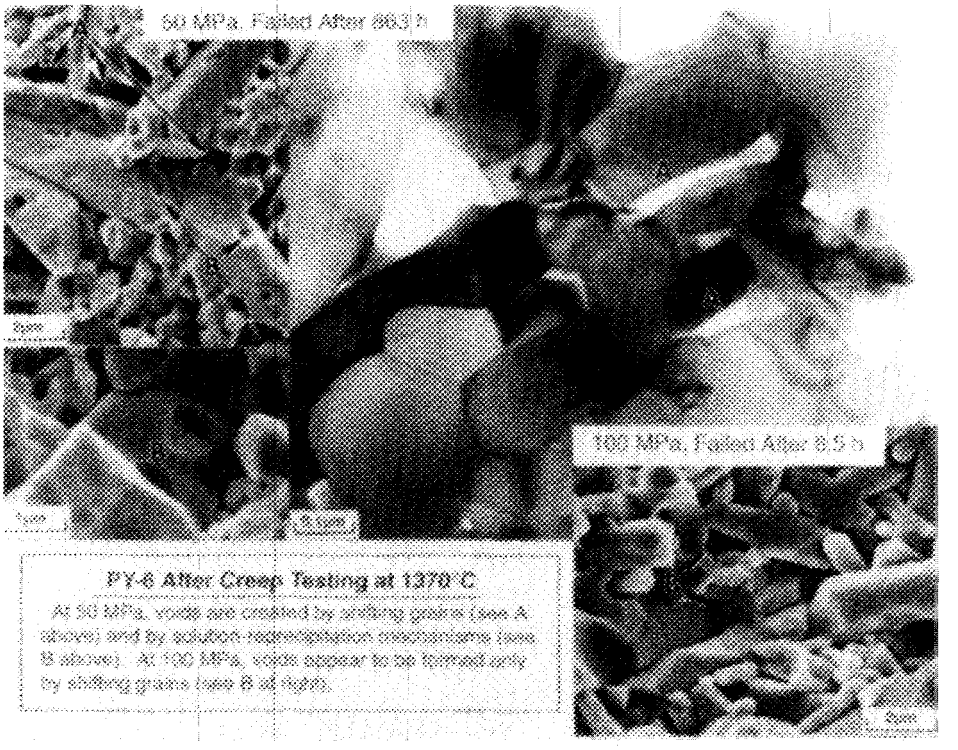

Fig. 13. Examples of grain boundary sliding and diffusion-associated mechanisms revealed by transmission electron microscopy.

generating large transient stresses during abrupt sliding events, which increases the cavity nucleation rate.[12]

One key indicator of the dominant creep mechanism is the creep stress exponent, n. In the present study, n was equal to 5.0, which is greater than values (1 to 3) reported for similar silicon nitrides in previous flexural creep studies; see ref. 3 for more detailed discussion. This discrepancy is due to creep-induced stress relaxation and stress redistribution in the flexure tests. The fact that n is greater than that expected for pure diffusional creep (n = 1) is due to the stress dependency of the creep damage mechanisms. This damage gives rise to an additional (unaccommodated) strain rate component, $\dot{\varepsilon}_c$, which is equal to the product of the steady-state creep rate measured in the absence of the cavities, $\dot{\varepsilon}_{so}$, and a parameter, ρ, which is proportional to the number of cavities (microcracks) per unit volume, N_{mc}, and d^3, where d is the cavity (microcrack) diameter.[5] The total creep strain rate, $\dot{\varepsilon}_{st}$, is then given as:

$$\dot{\varepsilon}_{st} = \dot{\varepsilon}_{so}(1 + \rho) = \dot{\varepsilon}_{so}(1 + D\, N_{mc}\, d^3) \quad , \tag{4}$$

where D is a constant (~ 0.5). For the case of diffusional creep, $\dot{\varepsilon}_{st}$ ($= \dot{\varepsilon}_{so}$) is proportional to the applied stress. The stress and time dependencies of ρ will dictate the deviation of the measured strain rate from that expected for solely diffusional creep. One may assume that at a given stress, ρ will increase from zero (at time, $t = 0$) to some critical value, ρ_c, at failure. During this time, if ρ becomes significantly larger than one, the $\dot{\varepsilon}_{st}$ will exceed $\dot{\varepsilon}_{st}$ prior to failure; see discussion of stress dependence of ρ in ref. 3. Such behavior is consistent with the tertiary creep regime observed at 1370°C.

The creep exponent increased to 16.1 at 1150°C suggesting a change in the deformation mechanism. This hypothesis is confirmed by the results in Fig. 9, which illustrates poor agreement between the experimental strain rate-stress data at 1150°C and the curve predicted from the application of the 1370 and 1260°C data to Eq. (1). Microstructural observations of the 1150°C fracture surfaces revealed the presence of an SCG zone consisting of extensive microcracking; see ref. 3 for more discussion. It is possible that the measured deformation was due to the compliance changes resulting from the generation and extension of these microcracks. This problem has been treated by Suresh and Brockenbrough[13] for the case of aligned slit cracks and random penny cracks. By assuming that the growth rate is a power-law function of the applied stress ($da/dt \propto \sigma a^p$), the authors showed that the strain rate should be proportional to σa^{p+1} for short-term creep and σa^{2p+1} for long-term creep. Considering the relatively short times involved in the 1150°C tests, the first relationship is expected to apply. Further, by assuming that $p \cong N$, the fatigue exponent in Eq. (2), the predicted creep exponent is equal to 19 (i.e., $19 = N + 1$ where $N \cong 18$), which is in fair agreement with the measured value of 16.1; see ref. 3 for additional discussion.

The activation energy, Q_c, describing the temperature dependence of the creep strain rate is another key indicator of the rate-controlling mechanism. Possible controlling mechanisms (for the 1260 and 1370°C data) include cavity nucleation, solution/precipitation of the silicon nitride in the intergranular phase, grain boundary diffusion, and viscous flow of the intergranular phase. Typical Q_c values for silicon nitride ceramics are in the range of 550 to 700 kJ/mole. Assuming that solution/precipitation is the underlying deformation mechanism, Raj and Morgan[14] showed that a major component to the activation energy is the heat of solution of silicon nitride (333 to 460 kJ/mole). However, a more recent analysis[15] of possible creep mechanisms has suggested that nitrogen diffusion is the rate-controlling step. This would explain the similarities in activation energies reported for creep and oxidation.[16]

For the PY6, Q_c was determined to be 1102 kJ/mole, which is considerably greater than the values discussed in the preceding paragraph. There are several possible explanations for this discrepancy. First, it is possible that the temperature dependence of the

viscosity of the intergranular phase was the dominant factor of Q_C. Raj and Morgan[14] showed that for viscosity-controlled creep, the activation energy can be quite high, particularly near the glass transition temperature. A second possibility is that the strain rate at 1370°C was increased by the activation of additional volume-generating mechanisms. Since Q_C is simply the slope of the $\dot{\varepsilon}_S$ versus 1/T curve, an incremental increase in $\dot{\varepsilon}_S$ would increase the calculated activation energy. In the present study, the two most likely sources for this incremental increase in $\dot{\varepsilon}_S$ were the generation of multiple gage section cracks and recrystallization of the intergranular phase. Optical microscopy provided evidence for both mechanisms.

3.3.2.2 Fatigue Mechanisms

For tests conducted at 1260 and 1370°C, failure was the result of the coalescence of creep damage followed by the generation of creep cracks. Although the predominant damage mechanisms were operative throughout the gage section, the accumulation process appeared to originate from the specimen surface; see ref. 3. This result suggests that the oxygen in the ambient environment played a significant role in the formation of the damage zone. The increased oxidation rate at 1370°C would explain the multiple surface cracks, resulting from the coalescence process, that were observed at this temperature. At 1150°C, damage in the form of microcracks was restricted to a well-defined region or zone; see ref. 3. Zone extension could be attributed to an SCG mechanism similar to that observed for hot-pressed silicon nitrides.[17]

A fracture surface that has a small creep damage zone (or a stress-corrosion cracking damage zone, as will be described in Sect. 3.7) is shown in Fig. 14(*a*) and is compared with its polished cross section in Fig. 14(*b*). An annular ring that appeared to advance from the surface toward the specimen center consistently was observed in tested specimens. The radial advance of the creep damage zone was equivalent to the thickness of the annular ring; this suggested that a change in the material microstructure within the volume of material in the annular ring was promoting the growth of the creep damage zone. The advance of the damage zone was found to be a consequence of long-term oxidation at elevated temperatures, and it was also found to be stress enhanced. In Fig. 15(*a*), a specimen that was dynamically fatigued at 10^{-4} MPa/s at 1370°C (see Sect. 3.5 for discussion of dynamic fatigue testing) and failed after 216 h at 86 MPa is compared with [see Fig. 15(*b*)] a specimen that was only aged (experienced no stress) for 216 h. The aged specimen was

ORNL-PHOTO 10589-95

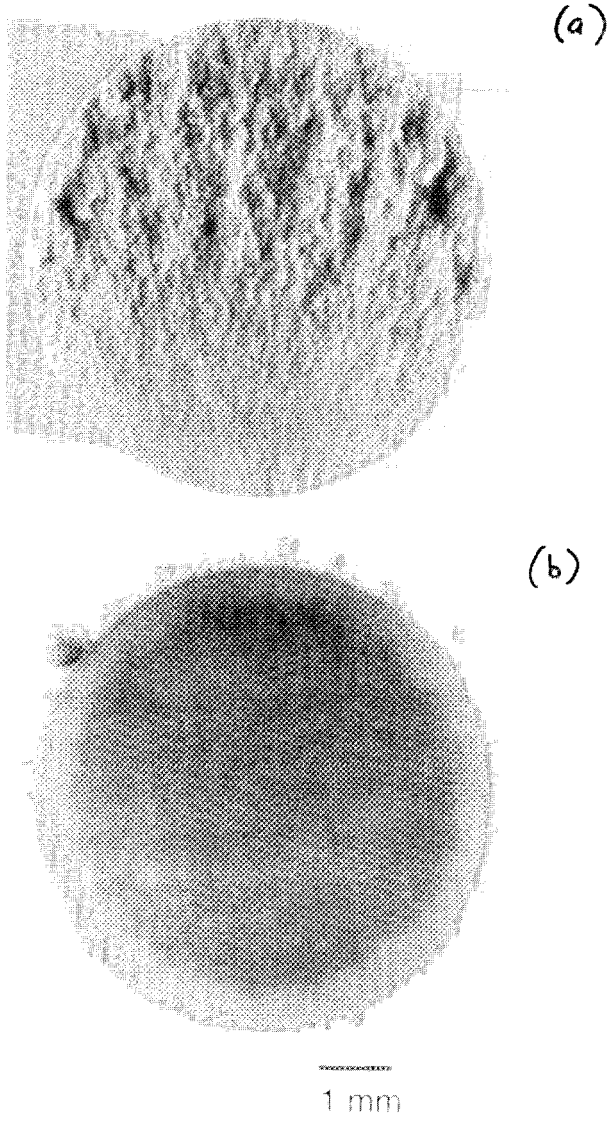

Fig. 14. Example of (*a*) a fracture surface from a specimen tested at 1200°C and 160 MPa (time to failure = 3806 h) and (*b*) its polished cross section showing the presence of an annular ring that formed due to long-term oxidation in the ambient environment.

ORNL-PHOTO 10590-95

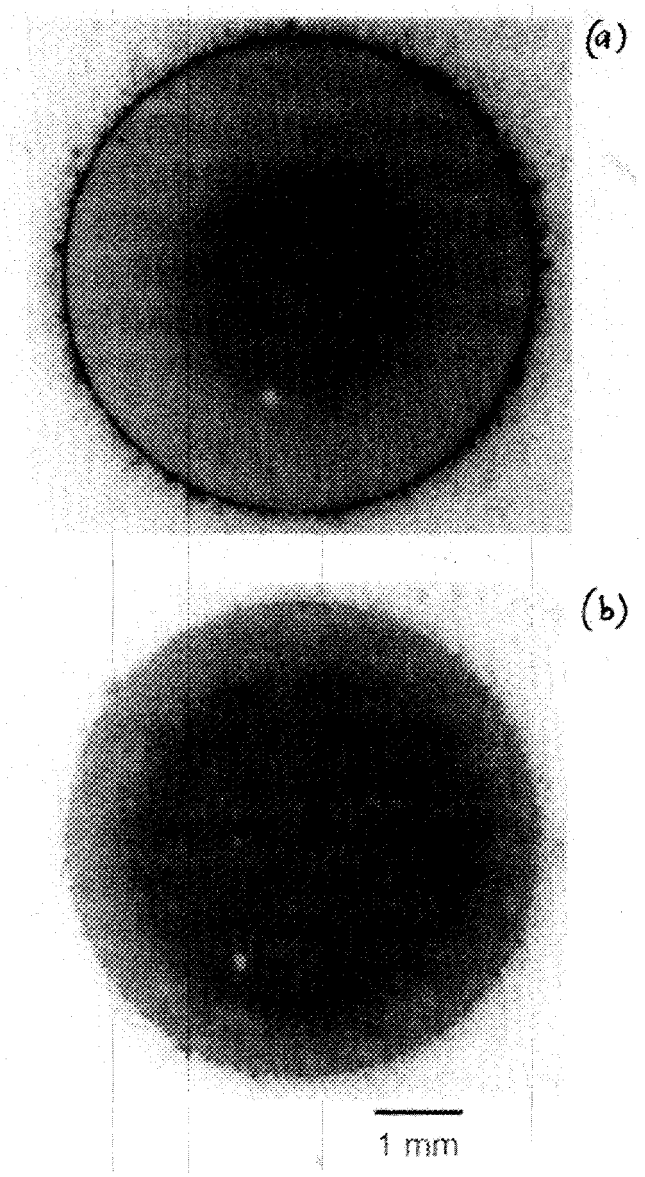

Fig. 15. The formation of the annular ring from long-term oxidation was stress enhanced. An example of a specimen that was (*a*) dynamically fatigued at 10^{-4} MPa/s at 1370°C (failed at 86 MPa after 216 h) is compared to (*b*) a specimen that was *only* aged (no stress) for 216 h. The ring is thicker for the specimen subjected to both stress and temperature than the specimen subjected only to temperature.

machined from the button-head shank of the tested specimen to avoid any specimen-to-specimen material variation. The outer annular ring is clearly thicker in the tested specimen [see Fig. 15(*a*)] that was subjected to stress and temperature than [see Fig. 15(*b*)] the specimen that was only subjected to temperature for the same amount of time. This finding was significant because it suggested that the specimen geometry (i.e., cross section-to-perimeter relationship) may be a function of how the specimen mechanically performs. For example, if two specimens have the same cross-sectional area, but one is round while the other is square, then the square specimen will have more surface area to react with ambient oxygen; the two specimens may mechanically perform differently as a consequence (see Sect. 3.7.2 for more discussion on this topic).

Competition between the two failure mechanisms may have been responsible for the duality in the fatigue-life characteristics measured for the PY6 silicon nitride. Similar behavior has been observed in polycrystalline alumina.[18] Microstructural observations (see ref. 3) indicate that the size of the associated damage zone was a critical factor in determining the dominate mechanism. For example, SCG, which controlled the fatigue behavior at lower temperatures and/or higher stresses, was a result of subcritical extension of a localized microcrack zone. Fracture occurred when the product of the damage zone size, a_Z, and applied stress, σ_a, reached a critical value, possibly in accordance with a Griffith-type expression, $\sigma_a (a_Z)^{1/2} = K_{IC}$ (i.e., stress-controlled fracture). In this sense, the localized microcrack zone was analogous to a large defect. As the temperature was increased, the creep rate increased at relatively low stresses thereby promoting a rapid extension of the creep damage zone. The creep-induced relaxation of crack-tip stresses precluded failure via the stress-controlled mechanism. In this case, fracture resulted when the strain associated with the creep damage reached a critical value dictated by the Monkman-Grant relationship (i.e., strain-controlled fracture).

The applicability of the Monkman-Grant relationship to the experimental data has several implications. First, it indicates that the rate of damage generation (cavitation and viscous sliding) was dictated by the bulk creep response of the material. In the case of cavitation, such a situation occurs when local diffusion processes associated with cavity growth are greater than the bulk creep deformation of the surrounding material. The cavity growth thus becomes constrained by the ability of the surrounding material to accommodate the volume generation.[5] The fatigue life, which is determined by damage generation rate, will be controlled by the creep rate as well. The Monkman-Grant relationship also provides a powerful tool for predicting fatigue lifetimes from creep deformation rates. As shown in Fig. 11, the fatigue life is uniquely determined by strain rate independent of applied stress and

temperature (for temperatures > 1200°C), but temperature-associated stratification was evident at 1150°C. More discussion of this follows.

3.3.3 Lifetime Prediction with Static Stress

The applicability of the Monkman-Grant and the Sherby-Dorn lifetime prediction analyses was examined. Static creep data (time to failure and minimum creep rate) generated at 1150, 1200, 1260, and 1370°C were used to modify the Monkman-Grant relationship in order to predict temperature-induced stratification. Static creep data generated at 1150, 1260, and 1370°C were used to predict the time to failure and minimum creep rate at an intermediary temperature of 1200°C using the Sherby-Dorn approach. Experimental confirmatory tests at 1200°C were conducted, and the resulting times to failure and minimum creep rates were compared to what was previously predicted from the lifetime prediction analyses.

3.3.3.1 Modification of the Monkman-Grant Relationship

Efforts were made to take into account the stratification of the Monkman-Grant relationship shown in Fig. 11 over the temperature range of 1150 to 1370°C. If the activation energies and stress exponents for static creep and fatigue [Q_C, n and Q_f, and N in Eqs. (1) and (2), respectively) are equal and their equivalence is temperature independent, then the Monkman-Grant relationship between the time to failure and minimum (or steady-state) creep rate is represented by Eq. (3). However, it was shown in Fig. 11 that temperature independence of n and N (i.e., $m = N/n \neq 1$) did not exist at 1150°C. For the case where $m \neq 1$, the time to failure may be represented as:

$$t_f = C\,\dot{\varepsilon}_S^{-m} \exp\left[\frac{Q_C\,(1-m)}{RT}\right] . \qquad (5)$$

More generally, if $Q_C \neq Q_f$ (letting $Q_C = Q_f + \Delta Q$), then the time to failure may be represented as:

$$t_f = C\,\dot{\varepsilon}_S^{-m} \exp\left[\frac{Q_C(1-m) + \Delta Q}{RT}\right] . \qquad (6)$$

Any inequality of the activation energies and stress exponents of Eqs. (1) and (2) is acknowledged by this modified Monkman-Grant relationship. The values for m and for the numerator in the exponential term in Eq. (6) [$Q_C(1 - m) + \Delta Q$] were obtained using multiple

linear regression analysis and were 1.19 and -249 kJ/mole, respectively. They were obtained using the time-to-failure and minimum strain rate data for static creep tests at 1150, 1200, 1260, and 1370°C, which are shown in Fig. 16. For m = 1.19, the value of ΔQ constitutes only -45 of the -249 KJ/mole total. It follows that most of the temperature dependence represented by the modified Monkman-Grant curves is due to the $Q_C(1 - m)$ term in Eq. (6).

ORNL-DWG95-8938

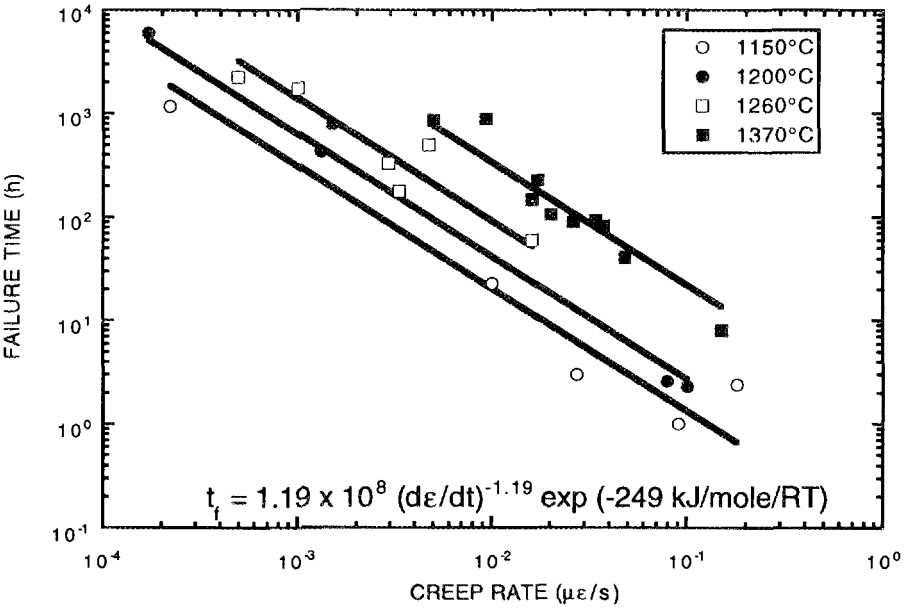

Fig. 16. Stratification of the time to failure-minimum creep rate data at 1150, 1200, 1260, and 1370°C was described by the modified Monkman-Grant relation; see Eq. (6).

3.3.3.2 Sherby-Dorn Relationship

The lifetime prediction utility of Sherby-Dorn temperature-compensated time to failure and minimum creep rate parameters were examined (see ref. 19 for review). The temperature-compensated time to failure is represented by:

$$\theta_f = t_f \exp\left[\frac{-Q_f}{RT}\right], \tag{7}$$

where θ_f is the Sherby-Dorn temperature-compensated time-to-failure parameter, while the temperature-compensated minimum creep rate is represented by:

$$\theta_C = \dot{\varepsilon}_S \exp\left[\frac{Q_C}{RT}\right], \tag{8}$$

where θ_C is the Sherby-Dorn temperature-compensated minimum creep rate parameter. Both θ_f and θ_C are a function of stress only. Figure 17 shows θ_C and θ_f as a function of stress for static creep tests conducted at 1150, 1260, and 1370°C. A bilinear expression (see ref. 20 for analogous analysis) was used to fit the experimental data because a linear expression was not satisfactory due to the "knee-like" transition in the data.

The obtained relation illustrated in Fig. 17 was extended to predict the time to failure and minimum creep rate for static creep tests at 1200°C, which are shown in Figs. 18(*a*) and (*b*), respectively. For the prediction of time to failure and minimum creep rate at 1200°C, the Sherby-Dorn analysis had good predictive capabilities, as evidenced by the confirmatory experimental data also shown in Figs. 18(*a*) and (*b*).

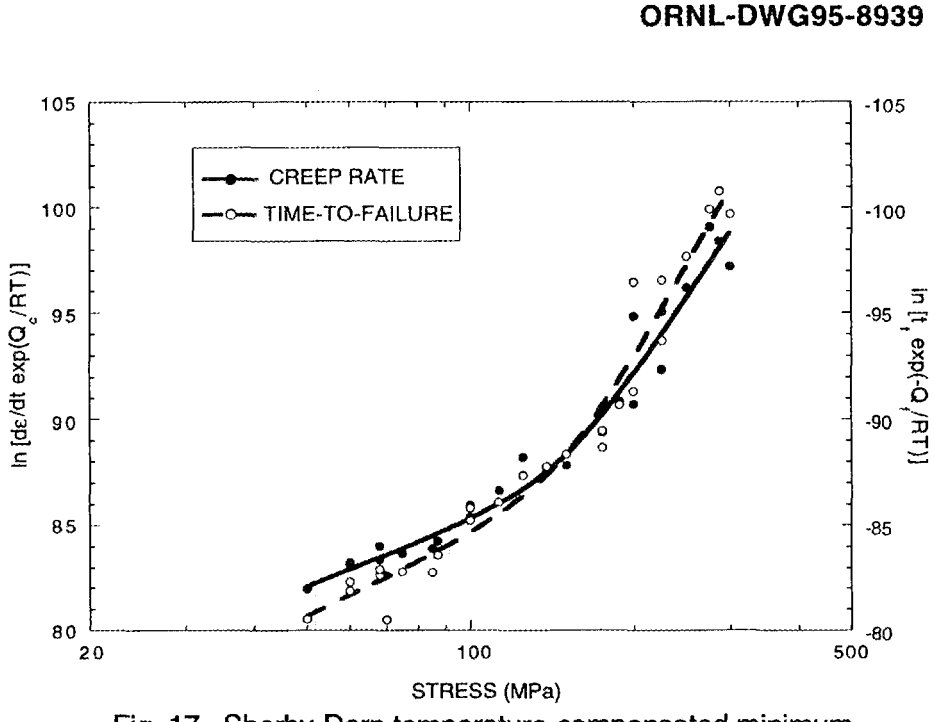

Fig. 17. Sherby-Dorn temperature-compensated minimum creep rate and time to failure as a function of stress.

ORNL-DWG95-8940

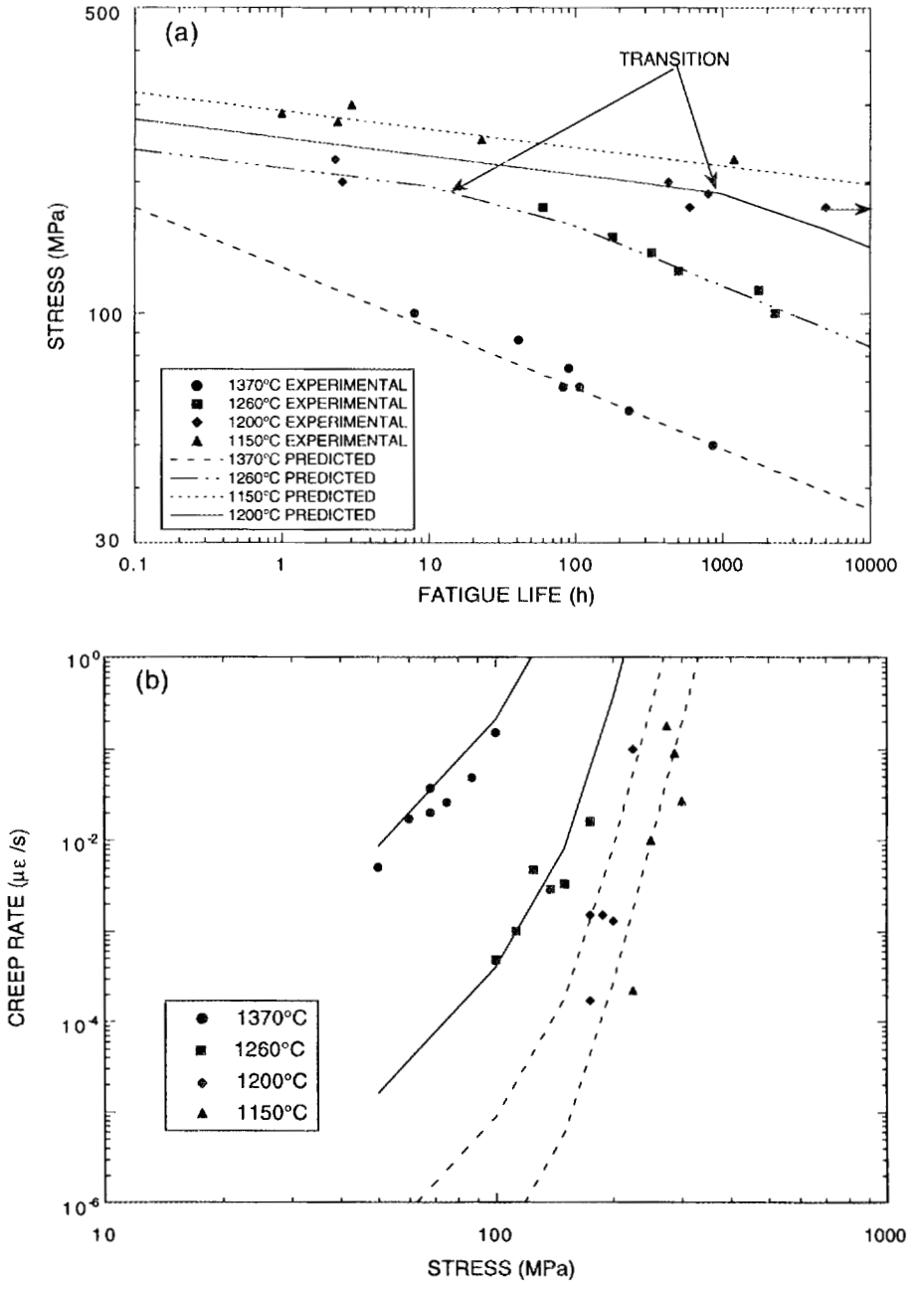

Fig. 18. Time to failure (*a*) and minimum creep rate (*b*) were predicted at 1200°C from information obtained from static creep tests at 1150, 1260, and 1370°C using the Sherby-Dorn temperature-compensated time-to-failure and minimum creep rate approaches. Data from confirmatory static creep tests conducted at 1200°C are shown with that predicted for 1200°C.

3.4 TENSILE RELAXATION BEHAVIOR

3.4.1 Strain Relaxation

Strain relaxation tests (i.e., creep recovery) were conducted at 1370°C to experimentally determine the values of the parameters which describe the anelastic strain recovery, ε_a. The total creep strain, ε_t', may be represented by:

$$\varepsilon_t' = \varepsilon_e + \varepsilon_a + \varepsilon_p \ , \tag{9}$$

where ε_e is the elastic strain, ε_a is the anelastic strain, and ε_p is the plastic strain. The elastic strain is totally recoverable and is time independent, while the anelastic strain is recoverable but is time *dependent*. The plastic strain is not recoverable. The strain relaxation testing was conducted to seek the time-dependent behavior of ε_a.

The motivation behind strain relaxation testing was to identify how the strain of PY6 silicon nitride recovers on unloading, information that was deemed important for understanding dynamic and cyclic performance of PY6 silicon nitride. As will be seen in Sect. 3.6, the results obtained from these strain relaxation tests are to be used for the prediction of cyclic creep strain as a function of time. Tests were only conducted at 1370°C because there was a limited number of specimens. The strain recovery and the primary creep mechanisms are believed to be equivalent (see ref. 21 for further consideration of this congruency) and result from the anelastic response of the amorphous grain boundary phase and the sliding of the grain boundaries, which is accommodated by the elastic deformation of the material adjacent to grain asperities between the grains.[22]

Several relaxation tests were conducted to examine any dependence of q, the relaxation time constant, on: (1) the hold time (0.1, 1, and 10 h) at 100 MPa prior to load removal, (2) different amounts of total creep strain, and (3) the amount of stress removed ($\Delta\sigma$). It was found that q was independent of the hold time at peak stress prior to unloading and also independent of the total strain accumulated.[21] The total amount of ε_a recovered (ε_a') was found to be linearly dependent on $\Delta\sigma$ over the changes in stress examined. It exhibited the relation $\varepsilon_a' \cong 6 \bullet \Delta\sigma$ for 54 MPa $\leq \Delta\sigma \leq$ 93 MPa where ε_a' and σ have units of $\mu\varepsilon$ and MPa, respectively. An example of a strain relaxation test history is shown in Fig. 19. The elastic load, ε_e, is subtracted out from the strain shown in Fig. 19, so the decay shown is strictly due to anelastic recovery. The relaxation time constant is equal to the time it took for 63% (i.e., e^{-1}) of ε_a' to recover. Although it was debatable whether or not ε_a' was indeed ever attained (i.e., $\dot{\varepsilon}_a = 0$), even after *days* at the unloaded stress, in practicality $\dot{\varepsilon}_a \cong 0$ after

ORNL-DWG95-8941

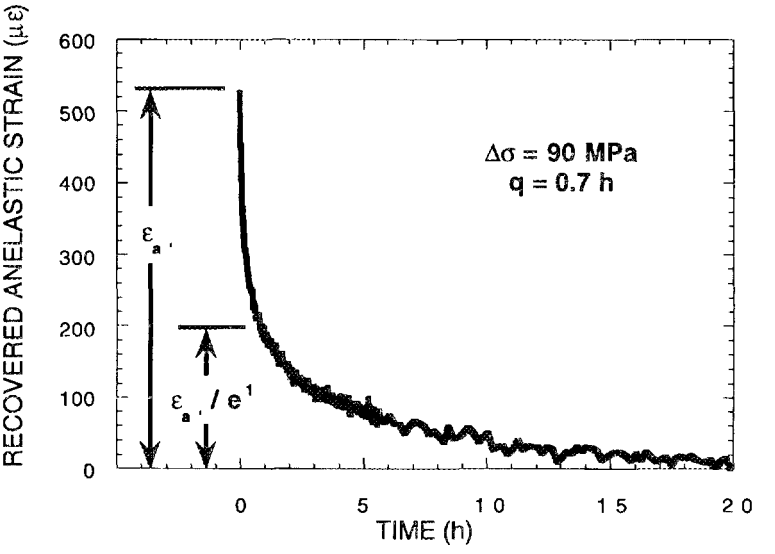

Fig. 19. Strain relaxation behavior of PY6 at 1370°C. The relaxation time constant, q, was determined to be 0.7 h.

~ 4 to 5 h. It was determined that q = 0.7 h = 2500 s. A single relaxation time constant was determined to represent the relaxation behavior for the sake of simplicity; however, evidence suggests that a spectrum of relaxation constants may be more representative.[22,23] The fraction of recoverable anelastic creep strain is relatively small compared to the total, as illustrated in Fig. 20. Because of its small magnitude, creep recovery in PY6 may be of practical interest only for low applied stresses that yield correspondingly small total strains.

3.4.2 Stress Relaxation

Stress relaxation testing is a technique that permits the survey of several decades of creep rates and stresses in a duration of hours, whereas the alternative, static creep testing, may take hundreds or even thousands of hours to generate equivalent data. The understanding of how a material stress relaxes is important information for designers of components that are to be constrained at elevated temperatures. Fasteners, joined components, and rotors that are shrink-fitted to shafts are examples of components that require continued constraint at elevated temperatures in order for them to maintain their usefulness.

ORNL-DWG95-8942

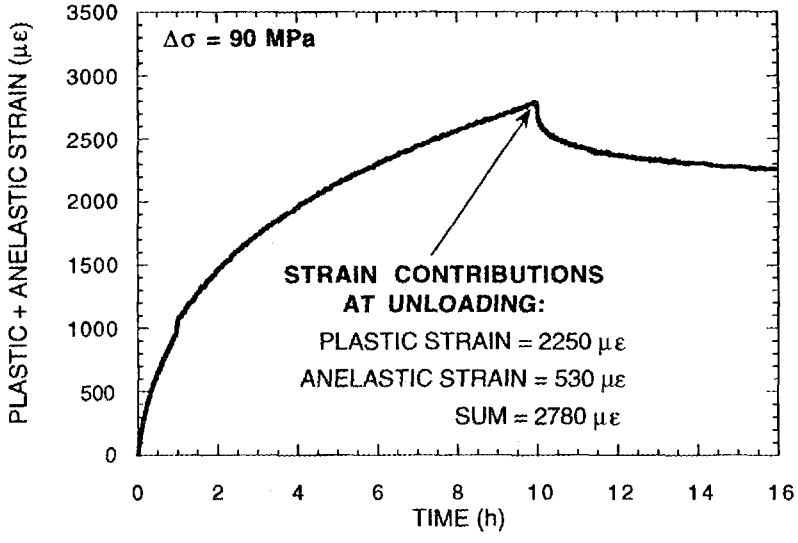

Fig. 20. The contribution of the anelastic strain to the total creep strain is small. Shown here is a PY6 specimen strain relaxed at 1370°C with the initial stress = 100 MPa. Strain relaxation testing showed that most of the creep strain is plastic, non-recoverable strain.

Although proposed more than 20 years ago,[24] few studies (e.g., ref. 25) before the efforts stemming from this project have reported the use of the stress relaxation technique on ceramics. The method and utility of using stress relaxation testing to represent strain rate-stress parameters at elevated temperatures were explored using PY6 silicon nitride in a preliminary fashion. Stress relaxation testing involved loading the button-head specimen to a predetermined stress in load control, then switching to strain control to maintain a constant strain; this activated stress decay. Usage of the extensometer described in Sect. 3.3.3 in strain control eliminated the need to incorporate machine compliance effects in the data analysis. Stress relaxation tests were conducted at 1260 and 1370°C.

As described by Eq. (9), the total creep strain (ε_t) is the sum of elastic strain (ε_e) and inelastic (ε_i) strain; furthermore, ε_i is the sum of viscoelastic (ε_a) and plastic strain (ε_p). When the total creep is held constant in a stress relaxation test, the following relationship may be considered:

$$\dot{\varepsilon}_i = -\dot{\varepsilon}_e = -\frac{1}{E}\frac{d\sigma}{dt} , \qquad (10)$$

where the dots denote time derivatives, and the last term relates the elastic stressing rate with the elastic straining rate.

An example of a stress relaxation history for PY6 at 1370°C is shown in Fig. 21. The maintained strain for this stress relaxation test was 420 με, which is represented in Fig. 21. The accumulation of plastic and anelastic strain during the test results in the relaxation of stress. The asymptotically attained, relaxed stress of ≅ 25 to 30 MPa is significant and useful for design purposes because this is the stress range where no more plastic and anelastic strain is accumulated.

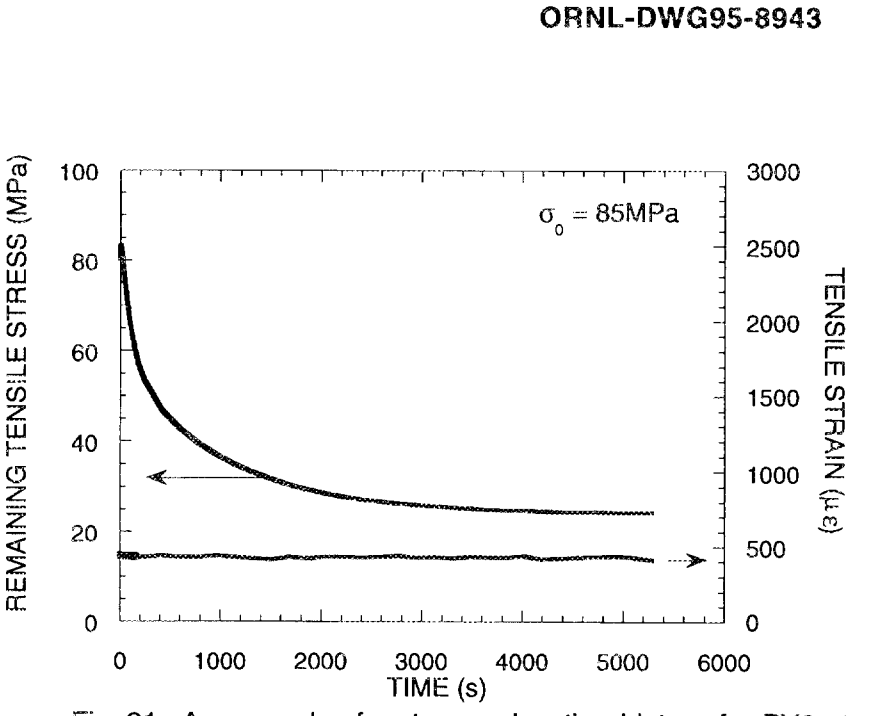

Fig. 21. An example of a stress relaxation history for PY6 at 1370°C and the constant strain that was held during the test.

The creep rate as a function of stress for the stress relaxation tests illustrated in Fig. 21 is illustrated in Fig. 22. Data generated from the stress relaxation test are compared to data generated from static creep tests. The power law curve-fitted stress (or creep) exponents are equivalent for both types of tests. However, the creep rates for the stress relaxation tests are much larger than the static creep tests for equivalent stresses. The stress relaxation test was conducted at 420 με; with reference to Fig. 8, this was most likely in the primary regime for PY6 at this temperature. The fact that the stress relaxation test yielded a creep exponent equivalent to that generated from static creep tests (where minimum creep rates occurred in the primary creep region at relatively high stresses and the secondary creep region at relatively low stresses) may have been a coincidence; however, the creep

ORNL-DWG95-8944

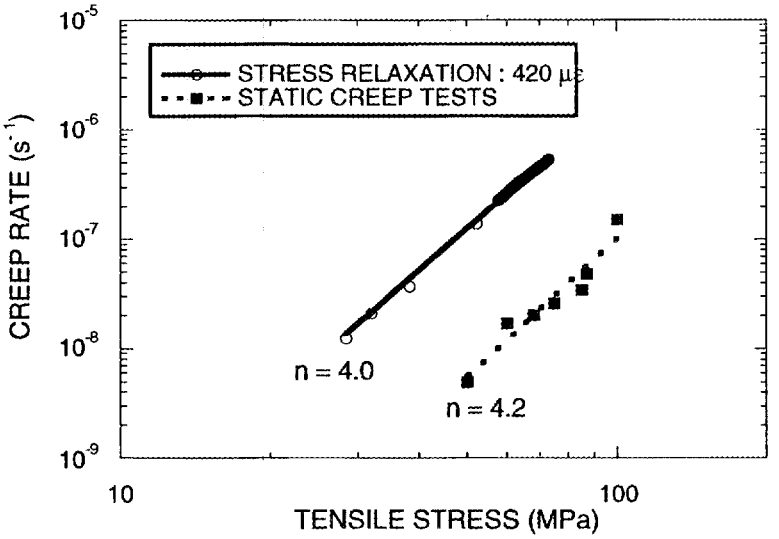

Fig. 22. Comparison of creep rate as a function of stress from one stress relaxation test versus several static creep tests for PY6 at 1370°C. Power-law curve-fitted values of the stress (or creep) exponents are shown.

exponents for primary and secondary creep have been reported to be equivalent for a similar HIPed silicon nitride.[20] Again, acknowledgment of these subtle issues with data such as that presented in Fig. 22 is important; recognition of these issues and the generated data may be used in conjunction to validate the utility of using stress relaxation testing.

3.5 TENSILE DYNAMIC FATIGUE

The purpose of the dynamic fatigue effort was to characterize dynamic behavior of PY6 in the elevated-temperature regime of advanced heat engine designs and compare its results with those generated from static fatigue or static creep results, which were described in Sect. 3.3. Stress-life relations in static fatigue and strength-stress rate relations in dynamic fatigue were examined in terms of temperature sensitivity. Direct comparisons between dynamic and static fatigue results were made to gain additional insight into the failure mechanisms in PY6 at elevated temperatures. This effort included the evaluation of the applicability of an SCG model to correlate dynamic and static fatigue properties. In addition,

fractographic analysis for determining the key features of failure modes was utilized. The activity of SCG, creep rupture, or a combination of both were examined.

Dynamic fatigue tests were carried out at 1150, 1260, and 1370°C in ambient air. Specimens were tested to failure at various stressing rates: 3.7×10^{1}, 10^{0}, 10^{-1}, 10^{-2}, 10^{-3}, and 10^{-4} MPa/s. Stress-strain curves were recorded for each test to monitor the progress of macroscopic deformation.

3.5.1 Slow Crack Growth Modeling

For most ceramics, subcritical crack growth can be expressed by the following power law relation:[26]

$$V = da/dt = AK_I^N = A(Y\sigma\sqrt{a})^N \quad , \tag{11}$$

where V is the crack growth rate, a is the crack size, t is time, A and N are material constants, K_I is the Mode I stress-intensity factor, Y is a geometric factor, and σ is the applied stress.

The time to failure in static fatigue, t_{sf}, is the time required for the initial flaw to grow to the critical size under a constant applied stress, σ_a. It may be approximated by integrating Eq. (11) such that:[27]

$$t_{sf} = BS_i^{N-2}\sigma_a^{-N} \quad , \tag{12}$$

where $B = 2/[AY^2(N-2)K_{Ic}^{N-2}]$, S_i is the inert strength, and K_{Ic} is the plane strain fracture toughness.

In a similar approach, the fracture strength, S_f, for a specimen under a constant stress rate, $\dot{\sigma}$, can be derived from Eq. (11) as the following approximation:[27]

$$S_f^{N+1} = B(N+1)S_i^{N-2}\dot{\sigma} \quad . \tag{13}$$

Equation (13) provides an indication of the stressing rate dependence of strength in that fracture strength increases with increasing stress rate as the crack or cracklike flaw has less time to grow.

The time to failure in dynamic fatigue, t_{df}, for a constant stressing rate, $\dot{\sigma}$, can also be related to t_{sf}:

$$t_{df} = (N+1)\, t_{sf} \ , \tag{14}$$

where the applied stress, σ_a, for constant stress loading is equal to the fracture strength, S_f, under a constant stress rate, $\dot{\sigma}$. One can predict the failure time of either static or dynamic fatigue given one of the failure times, if both failure modes are dominated by SCG with a simple power law as described in Eq. (11). The crack growth exponent, N, can be determined from static fatigue results or dynamic fatigue results using Eqs. (12) or (13), respectively. That is, N can be obtained from the slope of the best-fit curve of the log σ_a vs log t_f static fatigue data or from the log S_f vs log $\dot{\sigma}$ dynamic fatigue data.

3.5.2 Dynamic Fatigue Behavior

A summary of the failure stresses and strains to failure as a function of stressing rate for 1150, 1260, and 1370°C dynamic fatigue tests is listed in Table 4. The dynamic fatigue results with tensile strength plotted against stressing rate at three different temperatures are illustrated in Fig. 23. A general trend of decreasing tensile strength with decreasing stressing rate at 1150°C was found. For 1260 and 1370°C, this trend was also present but in two regions: stressing rates > and $\leq 10^{-2}$ MPa/s, respectively. However, the tensile strengths for 10^{-2} MPa/s at 1260 and 1370°C exceeded the tensile strengths for the nearest higher applied stressing rate at each corresponding temperature. For stress rates > 10^{-2} MPa/s, the values of N were estimated as 24 at 1260°C and 7.1 at 1370°C. The N values for stress rates $\leq 10^{-2}$ MPa/s were estimated as 18 and 3.9 at 1260 and 1370°C, respectively. No such transition in the dynamic fatigue curve at 1150°C was observed for selected stressing rates in the current study, and the value of N was determined as 98. This fairly high value on N indicated that this material was not very sensitive to dynamic fatigue at 1150°C, in that the tensile strength did not substantially decrease with decreasing stressing rate. However, at 1260 and 1370°C, the N values lessened and the susceptibility of dynamic fatigue was more substantial.

Table 4. Summary of dynamic fatigue results

Temp. and Specimen I.D.	Stressing rate (MPa/s)	Failure stress* (MPa)	Total strain to failure (με)
1150°C			
5D115	37	367	1150
1D115	1	372	1270
2D115	0.1	311	1010
6D115	0.1	338	1450
3D115	0.01	322	1980
4D115	0.001	320	1560
7D115	0.0001	341	2520
1260°C			
1S126	37	350	1250
2S126	37	363	1250
3S126	37	368	--
1D126	1	324	--
2D126	0.1	289	2230
5D126	0.1	276	1810
3D126	0.01	339	3890
4D126	0.001	204	3390
7D126	0.001	304	5310
6D126	0.0001	269	9130
1370°C			
1S137	37	274	1500
2S137	37	302	--
1D137	1	197	2640
2D137	0.1	135	4070
3D137	0.01	217	8010
4D137	0.001	131	10320
5D127	0.0001	86	12240

*Failure strengths scaled to gage section volume of 1108 mm^3, a gage section diameter of 6.35 mm, and using a room-temperature Weibull modulus equal to 9.0.

ORNL-DWG95-8945

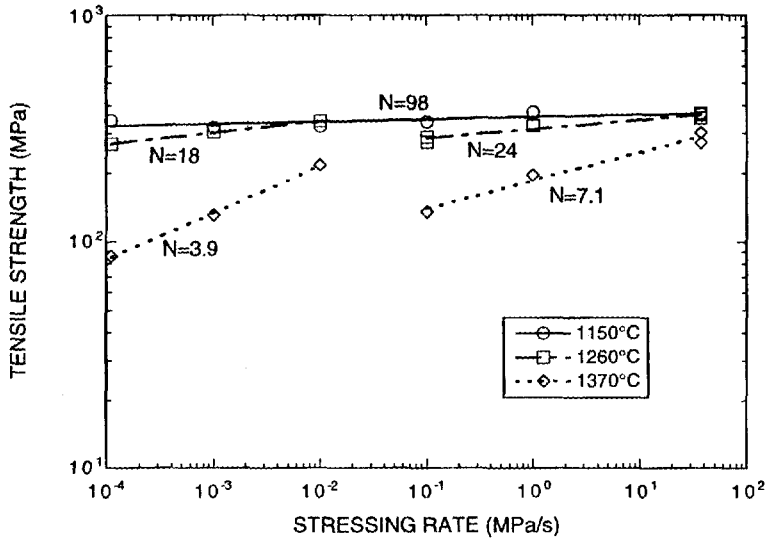

Fig. 23. Tensile strength as a function of stressing rate for PY6 at 1150, 1260, and 1370°C.

The shift of N values in dynamic fatigue curves at 1260 and 1370°C implied that there was a change of dominant failure mechanism from SCG to creep rupture with a decrease in stress rate. An apparent change in failure mechanism was also evident in the stress-strain curves from dynamic fatigue tests as shown in Fig. 24. At all stressing rates at 1150°C, the stress-strain curves exhibited an extensive linear portion (with a nearly identical slope) with nonlinearity becoming evident just prior to failure; see Fig. 24(*a*). This shift from linear to nonlinear stress-strain behavior reflected compliance changes that resulted from SCG. Similar linear to nonlinear stress-strain behavior (with a nearly identical slope in linear portions) was also observed at 1260 and 1370°C at the stress rates > 10^{-2} MPa/s; see Figs. 24(*b*) and (*c*). However, creep deformation was detected at 1260 and 1370°C at stress rates ≤ 10^{-2} MPa/s as considerably longer periods of nonlinearity in the stress-strain curves were present in this regime. Nonlinearity also increased with decreasing stressing rate. This entirely nonlinear deformation behavior may have resulted from the ongoing accumulation of creep damage (cavities and microcracks) during dynamic fatigue testing. Moreover, the failure strains for the nonlinear stress-strain curves (≤ 10^{-2} MPa/s) at 1260 and 1370°C were substantially greater than those for the linear stress-strain curves (> 10^{-2} MPa/s). No significant variation of the failure strains at all stress rates was observed at 1150°C.

ORNL-DWG95-8946

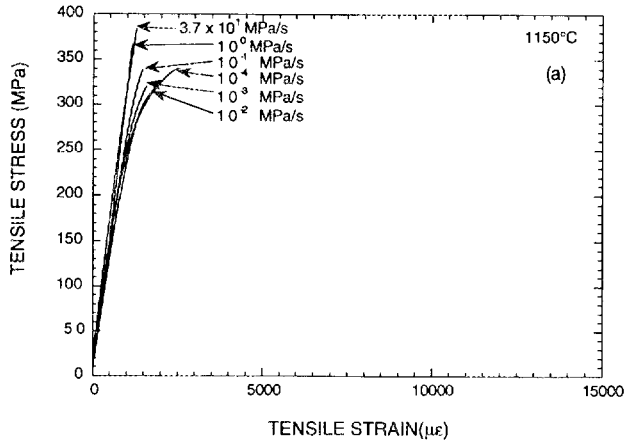

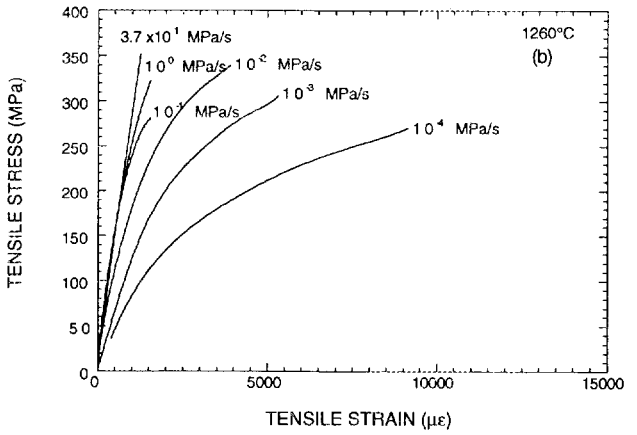

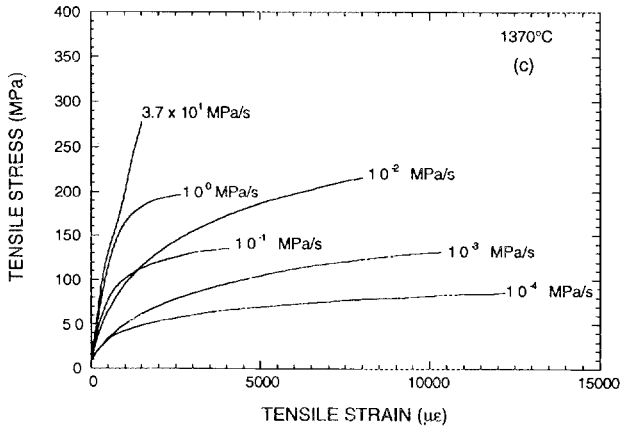

Fig. 24. Stress-strain curves generated from dynamic fatigue tests at (*a*) 1150, (*b*) 1260, and (*c*) 1370°C.

The linear to nonlinear changes in the stress-strain relations described can be qualitatively explained as follows. With the assumption that dynamic fatigue tests occurred mainly in the first section of the primary creep range, a simplified relationship for stress and strain rates based on a time-hardening or strain-hardening formulation was examined:[28]

$$\dot{\varepsilon} \cong \frac{\dot{\sigma}}{E} + D\sigma^n \quad , \tag{15}$$

where $\dot{\varepsilon}$ is the strain rate, E is the Young's modulus, D is an isothermal constant, and n is the creep (or stress) exponent. Integration of Eq. (15) generates the stress-strain relationship such that:

$$\varepsilon \cong \frac{\sigma}{E} + \frac{D\sigma^{n+1}}{(n+1)\dot{\sigma}} \quad . \tag{16}$$

Note that $\sigma = \dot{\sigma}t$ for dynamic fatigue tests. The first term on the right-hand side (RHS) of Eq. (16) is attributed to the instantaneous elastic response of the material. The second term on RHS of Eq. (16) is related to the time-dependent creep processes. In the SCG-dominated regime, the second term on the RHS of Eq. (16) is negligible or makes minor contribution to the total strain. This results in linear stress-strain behavior (with a nearly identical slope) that was observed at 1150°C as well as for the high stressing rates at 1260 and 1370°C. The minor deviation from linearity just prior to failure in these linear stress-strain curves possibly resulted from a slight decrease in the elastic modulus due to subcritical crack growth of the failure-initiating flaw.

In the creep-dominated regime, both terms on the RHS of Eq. (16) constituted significant contributions to the nonlinear stress-strain behavior observed for low stressing rates at 1260 and 1370°C. Firstly, damage accumulation by formation and growth of creep cavities and microcracks may have caused a decrease in the elastic modulus and led to an apparent nonlinear stress-strain relationship; see ref. 29 for more detailed discussion. The reduction in Young's modulus could be as much as a factor of five (ref. 30). Secondly, the nonlinear deformation from the second term on the RHS of Eq. (16) could have represented the creep processes associated with diffusion, viscous flow, or other mechanisms, or a combination thereof. The second term on the RHS of Eq. (16) also revealed the inverse relationship between stress rate and nonlinear strain (i.e., at a certain stress level reached during dynamic fatigue testing, low stressing rates would have generated more deformation than high stress rates). The experimental results did show this trend for the nonlinear

stress-strain behavior present at low stressing rates at 1260 and 1370°C. However, the first term on the RHS of Eq. (16) is also implicitly associated with stressing rate.

These dynamic fatigue results showed that SCG, crack blunting or healing, and creep damage generation were competing processes under dynamic loading conditions in the temperature range 1150 to 1370°C for PY6. It is likely that these processes were operating simultaneously, but one was found to dominate depending on the temperature and dynamic loading conditions. SCG of pre-existing flaws dominated failure for all stressing rates at 1150°C as well as for stressing rates > 10^{-2} MPa/s at 1260 and 1370°C. However, failures for stressing rates ≤ 10^{-2} MPa/s at 1260 and 1370°C were due to creep rupture. The increase in failure stress at 10^{-2} MPa/s at 1260 and 1370°C suggested that the localized defects responsible for failures at stress rates > 10^{-2} MPa/s were effectively blunted out. Otherwise, the strength would have continued to decrease as the stressing rate was lowered. Blunting was believed to be due to internal oxidation or creep-induced stress relaxation of crack-tip stresses.

3.5.3 Comparison of Static and Dynamic Fatigue

Comparison of static and dynamic fatigue behavior of PY6 at 1150, 1260, and 1370°C is shown in Figs. 25(*a*)-(*c*), respectively, with maximum stress plotted as a function of time to failure. The maximum stress is equal to the applied constant stress and tensile strength for static and dynamic fatigue, respectively. Static fatigue data were discussed in Sect. 3.3. The time to failure is the true failure time in static fatigue while in dynamic fatigue, it is set to the effective time to failure transformed by Eq. (14) with the application of N values obtained in static fatigue. Figure 25(*a*) illustrates the continuity in the data of static and dynamic fatigue tests at 1150°C by a single straight line except for 10^{-4} MPa/s (effective failure time = 37 h) in dynamic fatigue. It is implicit by this agreement that the failure mechanisms in static and dynamic fatigue at 1150°C are identical. SCG was identified as the prevailing failure mechanism in static fatigue of this HIPed silicon nitride at 1150°C suggesting that SCG is also the governing failure mechanism for dynamic fatigue at 1150°C. It is speculated that the deviation of the data at 10^{-4} MPa/s from the single straight line may reflect the transfer of failure mechanism to creep rupture or SCG with enhanced creep-assisted crack blunting. This shift in failure mechanism apparently occurred at higher stress rates (10^{-2} MPa/s) for temperatures ≥ 1260°C. One might notice the difference in N values, 22 and 98, respectively obtained from static and dynamic fatigue tests at 1150°C though SCG was the dominant failure mechanism in both fatigue conditions. This deviation could be attributed to the statistical nature as only four and six failed specimens were respectively used to determine

ORNL-DWG95-8947

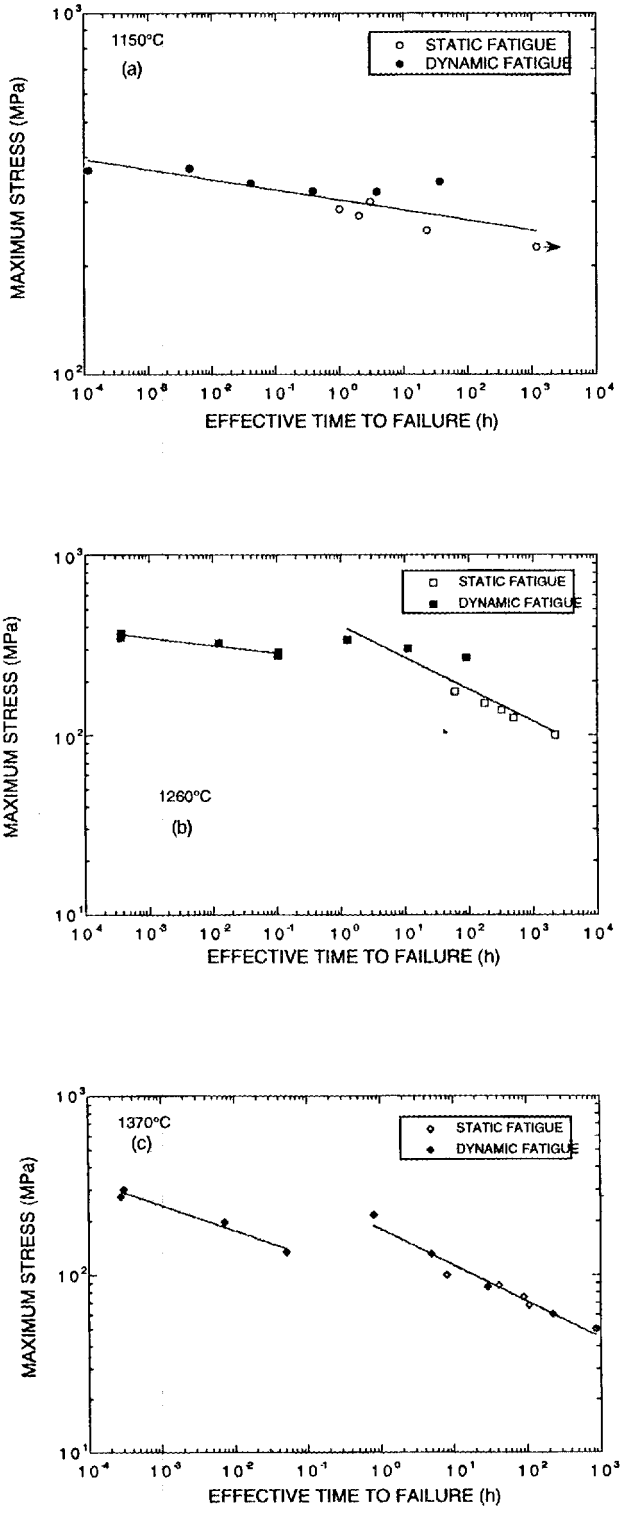

Fig. 25. Maximum stress as a function of time to failure for PY6 at (*a*) 1150, (*b*) 1260, and (*c*) 1370°C.

the N values for static and dynamic fatigue tests at 1150°C. However, the agreement of the static and dynamic fatigue data described by a single straight line in Fig. 25(*a*), as noted previously, demonstrates the general trend of a similar dominant failure mechanism (i.e., SCG) for both static and dynamic fatigue at 1150°C.

At 1260 and 1370°C, all static and dynamic fatigue data could not be represented by a single straight line; see Figs. 25(*b*) and (*c*). Two straight lines were required to satisfactorily fit all the data separated into two regions. The effective dynamic fatigue failure times with stress rates $\leq 10^{-2}$ MPa/s were found to be comparable with the static fatigue failure time [right regions in Figs. 25(*b*) and (*c*)], which indicated that there was a similarity of failure mechanisms between static fatigue and dynamic fatigue in this stressing rate region. The description of the rest of the dynamic fatigue data, at either temperature, by another straight line with different slope [regions on the left in Figs. 25(*b*) and (*c*)] implied a change of failure mechanism in dynamic fatigue for stressing rates $> 10^{-2}$ MPa/s at both 1260 and 1370°C. Creep rupture was concluded to be the dominant failure mechanism in dynamic fatigue for stressing rates $\leq 10^{-2}$ MPa/s at 1260 and 1370°C. The controlling failure mechanism in dynamic fatigue at stressing rates $> 10^{-2}$ MPa/s at either 1260 or 1370°C changed to SCG.

It may be argued that, unlike the results at 1370°C, all dynamic fatigue data at 1260°C could have been fitted by a single straight line instead of being separated into two regions. However, neither the previously described macroscopic stress-strain relations nor the microstructural analysis results could support this argument. Note that the stress-strain curves at 1260°C [see Fig. 24(*b*)] exhibited considerable nonlinearity for stressing rates $\leq 10^{-2}$ MPa/s and remained nearly linear for stressing rates $> 10^{-2}$ MPa/s. Fractographic analysis also indicated that concentrated creep cavities were present in specimens tested at stressing rates $\leq 10^{-2}$ MPa/s and not detected for stressing rates $> 10^{-2}$ MPa/s at 1260°C. In general, 1260°C was interpreted as the transition temperature for the change of dynamic fatigue failure mechanism from single mechanism (i.e., SCG) to dual mechanisms (i.e., SCG or creep rupture, depending on stress rate) for selected stressing rates.

The failure mechanism in dynamic fatigue at 1150°C was nearly insensitive to stress rate and was governed by SCG. At 1260 and 1370°C, the failure mechanism in dynamic fatigue became more stressing rate dependent and was dominated by SCG at stressing rates greater than 10^{-2} MPa/s and by creep rupture at stressing rates $\leq 10^{-2}$ MPa/s.

The failure life prediction method previously discussed is based on the assumption that static and dynamic fatigue failure mechanisms are identical and dominated by SCG of similar initial flaws to critical sizes. This assumption is valid in most ceramics at the temperatures where SCG is the major failure mechanism. However, caution is advised in the

application of this SCG model to correlate static and dynamic fatigue behavior at elevated temperatures where creep processes and crack blunting can compete with SCG. For example, the validity of using the linear-elastic fracture mechanics parameter, K_I, in the expression of crack growth rate needs to be examined. Other parameters such as C^*, the creep analog to the J-integral, may need to be considered in the description of the crack growth rate as stress relaxation occurs around the crack tip due to creep. Moreover, with the possibility of creep-assisted flaw/crack blunting or healing, creep processes could modify the flaw population initially present in the material, thereby eliminating the fundamental basis in the SCG model that fatigue failure occurs by subcritical crack growth of pre-existing flaws. These factors explain why the correlation of tensile static and dynamic fatigue of PY6 was not well defined by using only the SCG model, particularly at temperatures ≥ 1260°C. Other factors such as creep damage and crack blunting need to be implemented to refine the correlation between static and dynamic fatigue.

3.5.4 Slow Crack Growth Versus Creep Rupture

Being that there were two distinct regions existing in the dynamic fatigue data at 1260 and 1370°C, it was anticipated that the fracture surfaces would have appeared different for each region. In fact, it was found that two different types of features on the fracture surfaces were observed in dynamic fatigue specimens at various stress rates. The first feature appeared on fracture surfaces containing well-defined mirror, mist, and hackle regions for the specimens tested at stress rates > 10^{-2} MPa/s at 1260 and 1370°C; see Fig. 26(*a*). Such characteristics were present in all of the dynamic fatigue specimens tested at 1150°C. This was a typical fracture pattern dominated by the SCG mechanism which also appeared in the static fatigue specimens tested at 1150°C. The second type of fractographic feature was present at lower stressing rates (≤ 10^{-2} MPa/s) at both 1260 and 1370°C. The fracture markings revealed a transition to a small creep damage zone (region of high surface roughness) originating from the outer gage section surface; see Fig. 26(*b*). This transition was more evident at 1370 than at 1260°C. At 1370°C and 10^{-4} MPa/s [see Fig. 26(*c*)], no hackle markings were present, which suggested that the true mirror size exceeded the specimen cross-sectional dimension. The failures in these specimens likely occurred as a result of the coalescence of creep damage followed by the nucleation and growth of creep cracks. Moreover, the accumulation process for creep damage appeared to originate from the outer

ORNL-PHOTO 10591-95

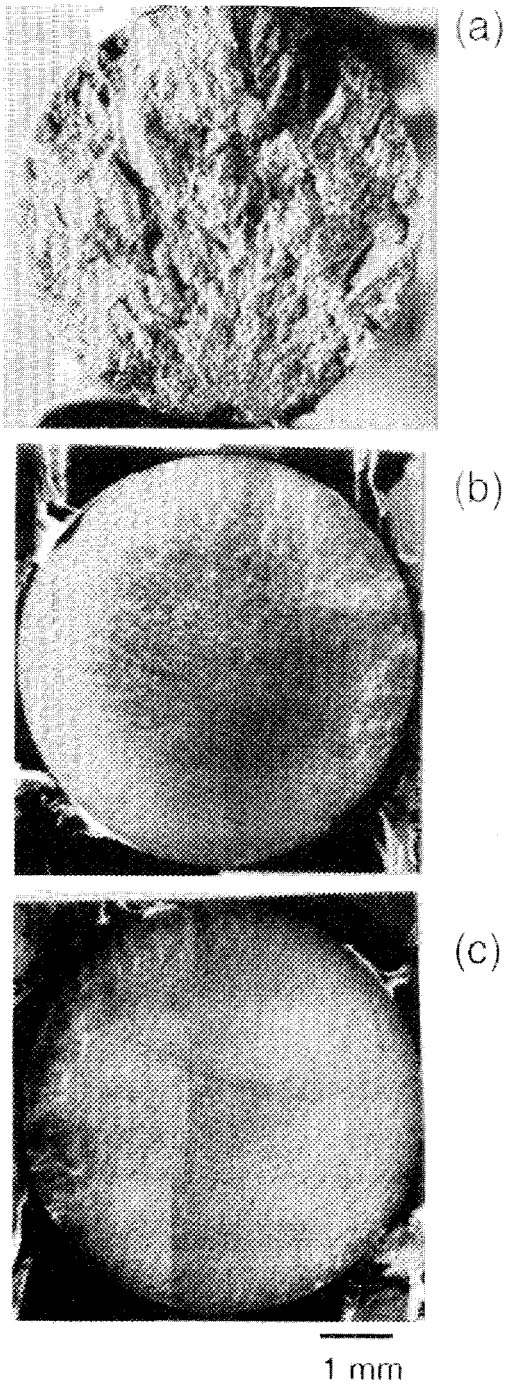

Fig. 26. Typical fracture surfaces generated in dynamic fatigue: (*a*) 37 MPa/s at 1370°C, (*b*) 10^{-3} MPa/s at 1370°C, and (*c*) 10^{-4} MPa/s at 1370°C.

surface where an oxidation scale was created. This suggested that there was an influence of oxidation in the damage coalescence stage for PY6. Creep damage zones also occurred in the static fatigue specimens at 1260 and 1370°C.

Detailed SEM examination of fracture origins and cavities along the fracture surfaces was inhibited by the presence of an oxide scale created by exposure of the fresh fracture surface to the ambient air at elevated temperature at the time of failure. However, a secondary fracture surface was generated parallel to the test fracture surface in the gage section so as to expose representative creep damage. Fractographic analysis of static fatigue specimens (see ref. 3) has indicated extensive cavitation along two-grain boundaries throughout the gage section volume in static fatigue specimens tested at 1260 and 1370°C. No such extensive creep damage was found in static fatigue specimens tested at 1150°C. Absence of extensive creep cavities was also noted in dynamic fatigue specimens tested at 1150°C, except for 10^{-4} MPa/s, as well as in those tested at 1260 and 1370°C for stressing rates > 10^{-2} MPa/s; see Fig. 27(*a*). In contrast, extensive creep cavities along the two-grain boundaries were observed in the dynamic fatigue specimens tested at 10^{-4} MPa/s and 1150°C as well as in those tested at stress rates ≤ 10^{-2} MPa/s at both 1260 and 1370°C; see Fig. 27(*b*). In the creep-dominated regime, cavity size increased with an increase in temperature. This was presumably due to the decrease in viscosity with increasing temperature. Furthermore, the creep-related damage may have blunted and healed the initial defects and restricted their growth. This would explain why the fracture strength in the creep-dominated regime (≤ 10^{-2} MPa/s) at 1260 and 1370°C was greater than the value extrapolated from the results of the SCG-dominated regime (> 10^{-2} MPa/s).

In general, the similarity of fracture surface features between dynamic and static fatigue specimens supports the argument that dynamic fatigue failures were essentially controlled by SCG at 1150°C as well as at stressing rates > 10^{-2} MPa/s at 1260 and 1370°C, and governed by creep rupture at 1260 and 1370°C for stressing rates ≤ 10^{-2} MPa/s. A comprehensive discussion of creep damage morphology has been given in a previous study on creep properties of this silicon nitride.[3] A brief description of the cavitation morphology is presented as follows. As shown in Fig. 27(*b*), the cavities were created along the two-grain boundaries and were lenticular in shape. These cavities extended into the silicon nitride grains which suggested that the growth mechanism involved solution/precipitation rather than viscous flow. Moreover, another common feature noticed on the secondary fracture surfaces

ORNL-PHOTO 10592-95

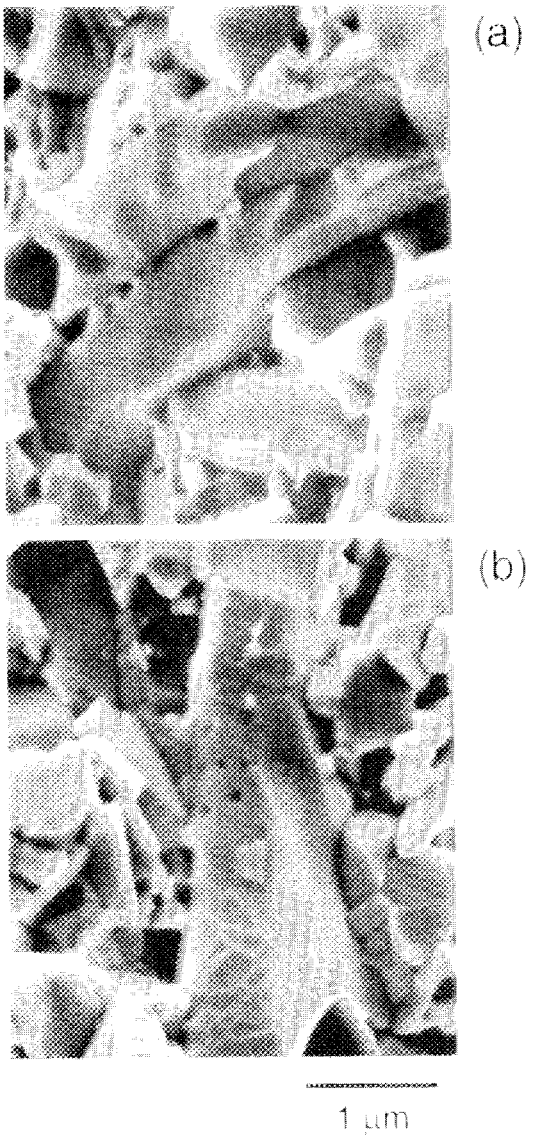

Fig. 27. Scanning electron micrographs of secondary fracture surfaces from specimens tested in dynamic fatigue: (*a*) 37 MPa/s at 1370°C, no cavitation, and (*b*) 10^{-3} MPa/s at 1370°C, cavities present along with a skeletal pattern of grain boundaries on grain facets.

for stressing rates $\leq 10^{-2}$ MPa/s at 1260 and 1370°C was the skeletal pattern of the intergranular phase outlining the interfaces between small grain clusters and a single large grain; see Fig. 27(*b*). The formed pattern may have been a consequence of grain separation by viscous flow of the boundary phase. Such deformation would lower the local fracture resistance of the intergranular phase and provide a preferred path for secondary fracture. This microstructural evidence suggested that the primary mechanism in the creep deformation was grain boundary diffusion accompanied by cavitation and grain separation by viscous flow.

The suppression of extensive creep cavitation in static and dynamic fatigue specimens at 1150°C possibly resulted from the intergranular phase having a high viscosity. The inhibition of extensive creep damage (or creep strain) in dynamic fatigue for higher stressing rates at 1260 and 1370°C resulted from the fact that the failure time by propagation of a single macrocrack was too brief to allow any appreciable creep damage.

3.6 TENSILE CYCLIC FATIGUE

3.6.1 Waveform Effects on Fatigue Performance

The objective of the tensile cyclic fatigue studies was to evaluate the tensile cyclic fatigue behavior of PY6 at 1150, 1260, and 1370°C using two frequencies and three loading waveforms. A direct comparison of cyclic and static fatigue results was used to gain insights into effects of loading mode on the failure mechanisms.

In order to examine the effects of frequency, cycle shape, and hold time at maximum stress on the cyclic fatigue behavior, cyclic fatigue tests were conducted under load control with a constant stress ratio R = 0.1 (R = minimum stress/maximum stress) with three waveforms: (1) symmetric trapezoidal wave at 0.1 Hz (0.5-s ramp and 4.5-s dwell); (2) sinusoidal wave at 10 Hz, and (3) triangular wave at 0.1 Hz. The first two waveforms were applied to tests at 1150, 1260, and 1370°C. Initially, strain was recorded only at discrete intervals for cyclic fatigue tests with 0.1-Hz trapezoidal loading due to the uncertainty of whether the movement of extensometer probe tips would generate any surface damage on the specimen and wear in the pivot points of the extensometer during continuous cyclic loading. No strain measurement was taken for the tests with 10-Hz sinusoidal loading due to the frequency limitation for operation of the contact extensometers. Only limited tests were performed with 0.1-Hz triangular loading at 1260 and 1370°C where strain was monitored continuously to provide information about the evolution of macroscopic deformation under cyclic loading conditions; more extensive testing and discussion using the triangular waveform

is found in Sect. 3.6.2. In these cases, no failures were found to be associated with extensometer contact. The results of the tension-tension cyclic fatigue tests are summarized in Tables 5 through 7.

Table 5. Summary of cyclic fatigue results for low-frequency, trapezoidal waveform. Waveform was 0.1 Hz (0.5-s load and unload, 4.5-s dwell at σ_{max} and σ_{min}), and R = 0.1

Temp. and Specimen I.D.	Maximum stress (MPa)	Cycles to failure	Time to failure (h)
1150°C			
3CF115	275	329600	915.6
1CF115	300	395700*	1099*
4CF115	313	218100	606
2CF115	325	1424	3.96
5CF115	332	6	0.017
260°C			
1CF126	150	422000*	1172*
4CF126	250	110100	306
6CF126	262	364000*	1011
2CF126	275	23630	65.6
5CF126	287	13490	37.5
3CF126	300	20	0.056
1370°C			
1CF137	75	369600*	1027*
6CF137	137	185700	516
2CF137	150	30980	86
5CF137	162	54	0.15
4CF137	175	51	0.14
3CF137	200	9	0.025

*Test interrupted; specimen did not fracture.

Table 6. Summary of cyclic fatigue results for low-frequency, triangular waveform. Waveform was 0.1 Hz and R = 0.1

Temp. and Specimen I.D.	Maximum stress (MPa)	Cycles to failure	Time to failure (h)
1260°C			
10CF126	250	6263	17
8CF126	275	110	0.3
9CF126	275	161	0.45
1370°C			
12CF137	100	406600*	1129*
11CF137	125	414	1.2

*Test interrupted; specimen did not fracture.

Table 7. Summary of cyclic fatigue results for high-frequency, sinusoidal waveform. Waveform was 10 Hz and R = 0.1

Temp. and Specimen I.D.	Maximum Stress (MPa)	Cycles to failure	Time to failure (h)
1150°C			
3HCF115	300	36000000*	1000*
2HCF115	313	287468†	8†
5HCF115	313	36150000*	1004*
1HCF115	325	28	0.001
1260°C			
1HCF126	275	10607902‡	294.7‡
4HCF126	287	372433000*	1034.5*
2HCF126	300	1228208	34.1
3HCF126	325	39	0.001
1370°C			
4HCF137	150	14546847‡	404.1‡
3HCF137	162	3928331	109.1
2HCF137	175	358016	9.94
1HCF137	200	33680	0.94

*Test interrupted; specimen did not fracture.
†Failed at the button-head radius.
‡Failure due to power outage.

3.6.1.1 Stress-Life Relation for Cyclic Fatigue

Log-log plots of maximum stress versus time to failure for cyclic fatigue tests at 1150, 1260, and 1370°C, respectively, are shown in Figs. 28(*a*)-(*c*). Each data point represents a single specimen tested to failure. Horizontal arrows in the plots indicate that failure had not occurred and that the tests were terminated. The time-delayed fracture behavior in cyclic fatigue was apparent as the time to failure for each cyclic waveform increased with decreasing stress level. At 1150°C, no significant difference in time to failure between trapezoidal and sinusoidal waveforms under the same maximum stress was observed. However, at 1260 and 1370°C, the time to failure under the same maximum stress under various loading types had the following order: sinusoidal > trapezoidal > triangular waveform. These results suggest that the cycle-shape dependence of the cyclic fatigue life for PY6 at 1150 to 1370°C increased with increasing temperature. The above comparison did not demonstrate whether the high-temperature cyclic fatigue behavior for this material was time dependent, because the cycle shape is different among selected loading waveforms. In the following section, an SCG model is applied to provide a first approximation of whether a true cyclic loading effect exists.

3.6.1.2 Correlation Between Cyclic and Static Fatigue

In conventional ceramic fatigue analysis, an SCG model (with a power-law relationship between crack growth rate and stress-intensity factor) is widely used for estimating fatigue life. With the assumption that all fatigue failures occur from growth of the initial flaws to final, critical sizes, the following relations can be obtained for uniform stress tests:

$$t_{sf} = \beta \sigma_s^{-N} \quad , \tag{17}$$

and

$$t_{cf} = \beta \sigma_{max}^{-N} \tau \left\{ \int_0^{\tau} [f(t)]^N \, dt \right\}^{-1} \quad . \tag{18}$$

In Eq. 17, t_{sf} is the time to failure for static fatigue under a constant stress, σ_s; β is a constant related to initial flaw size and geometry [see Eq. (12) and its discussion for more background]; and N is the crack growth exponent. Time to failure in cyclic fatigue, t_{cf}, is given in Eq. (18) where σ_{max} is the maximum stress, τ is the cycle period, and f(t) is a function of time

ORNL-DWG95-8948

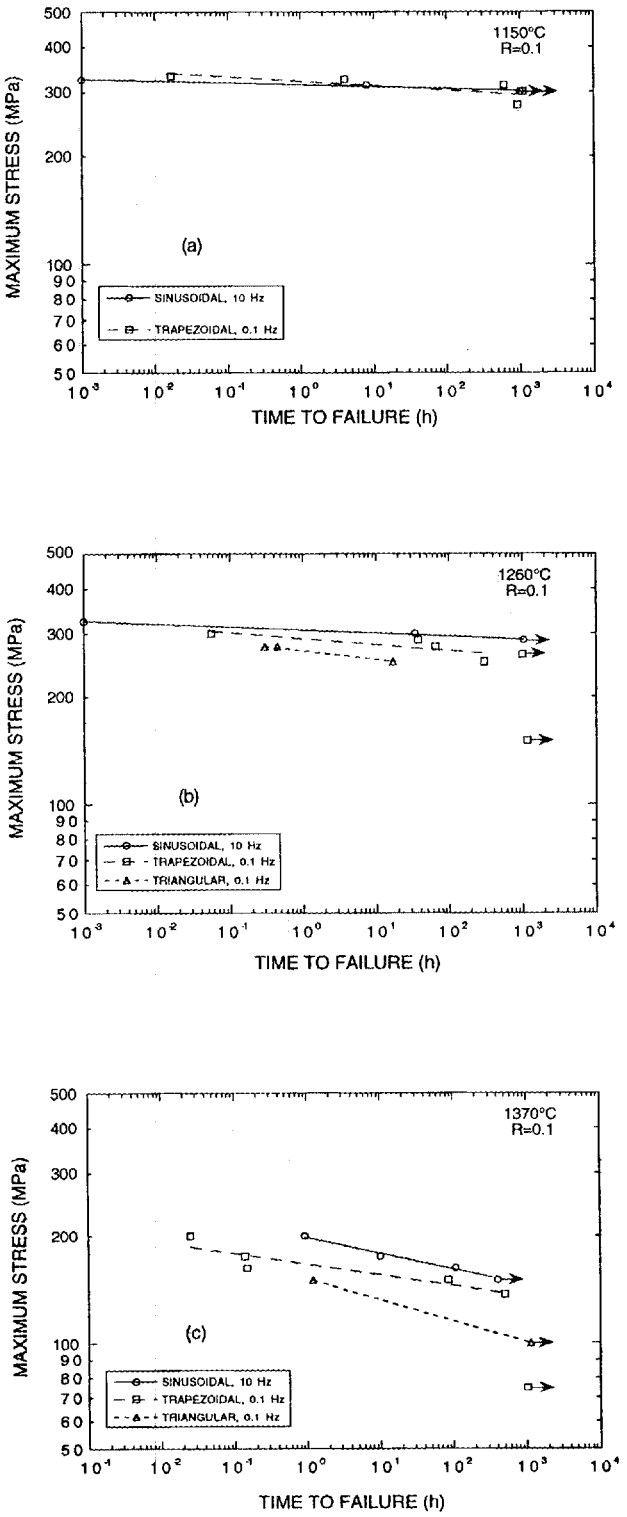

Fig. 28. Cyclic fatigue life of PY6 for various frequencies and waveforms at (*a*) 1150, (*b*) 1260, and (*c*) 1370°C.

associated with the cyclic waveform, such that the applied stress in a cycle can be described as $\sigma(t) = \sigma_{max} f(t)$. Note that the model predicts that the slopes of the static and cyclic fatigue curves are equal. Based on the stress-life relations in Eqs. (17) and (18), a so-called "effective" time approach was used to correlate static and cyclic fatigue behavior. The effective time to failure for static fatigue was equal to the actual time to failure, t_{sf}. However, the effective time to failure for cyclic fatigue is equal to the actual time to failure reduced by a factor because only a portion of the loading cycle is spent at the maximum stress in cyclic fatigue testing. The effective time to failure for cyclic fatigue can be defined as follows:

$$t_{cf,eff} = t_{cf} \tau^{-1} \left\{ \int_0^{\tau} [f(t)]^N dt \right\} . \tag{19}$$

Thus, for equivalent values of σ_{max} and σ_s, the effective time to failure in cyclic fatigue is equal to the failure time in static fatigue, provided that SCG of similar initial flaws is the primary mechanism for all failures. Therefore, making comparisons among the effective times to failure under similar maximum stresses aided in assessing whether all fatigue failures were dominated by the same SCG mechanism. With the results of such a comparison, one can obtain a first approximation whether or not there existed any cyclic loading effect on the failure mechanism.

The values of N were obtained from the stress-life relation in static fatigue [see Eq. (17)] through a power-law curve fit. Results of static fatigue tests were described in Sect. 3.3, and N was estimated to be 22 at 1150°C and 6.4 at 1260 and 1370°C. These N values were applied to Eq. (19) to convert the actual failure time to effective time to failure in cyclic fatigue. Cyclic and static fatigue results are compared in log-log plots of maximum stress versus effective time to failure in Fig. 29. The comparison indicates that the levels of maximum applied stress required to generate failures within 1 to 1000 h were greater in cyclic fatigue tests (both low and high frequency) than those in static fatigue tests. In this region, the effective failure times under cyclic loading were longer than those under static loading with the same maximum applied stresses. This difference in failure times becomes greater when the comparison is made by using the actual cyclic fatigue failure times.

The difference between static and cyclic fatigue life decreases with increasing stress level, as shown in Figs. 29(*a*)-(*c*). Although a direct comparison could not be made at high applied stresses (failure time less than 1 h) due to the absence of static fatigue data, both

ORNL-DWG95-8949

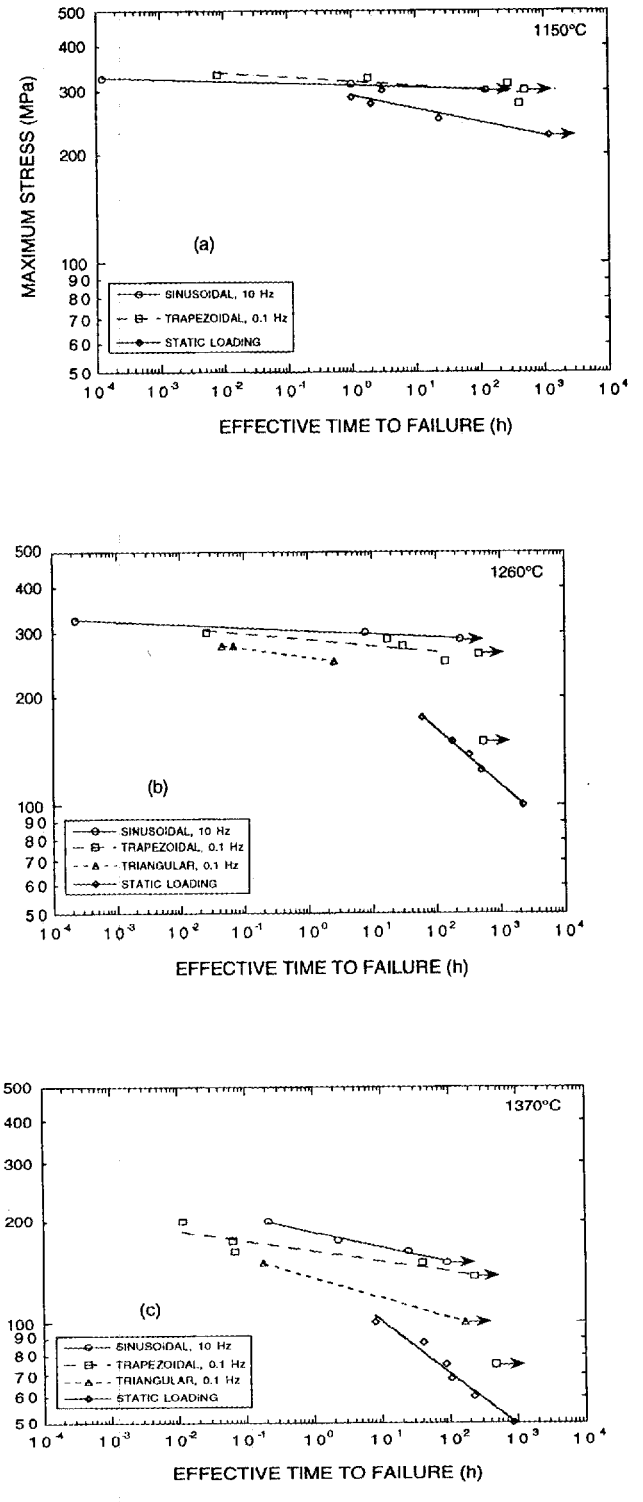

Fig. 29. Comparison of static and cyclic fatigue by an effective time-to-failure approach for data generated at (*a*) 1150, (*b*) 1260, and (*c*) 1370°C.

static and cyclic fatigue failures, at stress levels near the fast fracture strength, would result from SCG of a dominant inherent flaw. Such a transition of dominant failure mechanism from creep rupture to SCG in static fatigue at elevated temperatures has been shown in other silicon nitrides; see ref. 31 for more detailed discussion. Consequently, the cyclic effective life would be closer to the static fatigue life at higher stresses, which is consistent with the SCG model approach. However, for stresses well below the fast fracture strength, the static and cyclic fatigue life were not correlated by the SCG model, which suggested the existence of a true cyclic loading effect. More importantly, the evolution of damage under cyclic loading was much less than for static loading. Such behavior at elevated temperatures is opposite of the room-temperature fatigue behavior of some ceramics where cyclic loading has a more deleterious effect on resistance to fracture than static loading; see ref. 31 for review of this. This difference is attributed, at least in part, to the softening of the intergranular phase at elevated temperatures where the mechanisms responsible for the detrimental cyclic loading effect at room temperature become ineffective.

Figure 29 also indicated that under the same maximum applied stress, the effective cyclic fatigue life for specimens tested at 1260 and 1370°C still had the following order: sinusoidal > trapezoidal > triangular waveform. This difference in effective cyclic fatigue life between low- and high-frequency tests was as large as an order of magnitude or more, depending on the applied stress levels. This result implied that cyclic fatigue life for this PY6 silicon nitride at 1260 and 1370°C is cycle-shape or stress-rate dependent. Note that the maximum stress rates were at the orders of 10^1, 10^2, and 10^3 MPa/s for triangular, trapezoidal, and sinusoidal loading, respectively. Such dependence of cyclic fatigue life on cycle shape or stress rate might be related to the rate-sensitivity of the viscous characteristics of the secondary phase. Apparently, higher frequency or higher stress rate caused less strength degradation.

The influence of stress rate on the elevated-temperature damage mechanisms for the PY6 material was discussed in Sect. 3.5. The static fatigue failure mechanisms agreed with the dynamic fatigue failure mechanisms if it is argued that the stressing rates in static fatigue tests are infinitely slow. At 1150°C, SCG was reported as the dominant failure mechanism for static fatigue, which agreed with the fact that SCG was responsible for all the dynamic fatigue failures regardless of the stressing rate. At 1260 and 1370°C, static fatigue failures were dominated by creep rupture which also controlled the dynamic fatigue failures at slow stressing rates ($\leq 10^{-2}$ MPa/s). The absence of extensive creep damage at 1150°C in both static and dynamic fatigue was believed to be a consequence of the increased viscosity of the intergranular phase. The stressing rates in cyclic fatigue tests were so high that their

failure mechanisms were different from those in static fatigue, particularly at 1260 and 1370°C, as supported by the dynamic fatigue results.

The apparent N values (> 80 at 1150°C, > 40 at 1260°C, and > 23 at 1370°C) in cyclic fatigue are much greater than those in static fatigue, which suggested that the failure mechanisms were different between static and cyclic fatigue. The N values estimated from dynamic fatigue data were 98 for all applied stress rates at 1150°C; 24 and 7.1 for stress rates > 10^{-2} MPa/s at 1260 and 1370°C, respectively; and 18 and 3.9 for stress rates ≤ 10^{-2} MPa/s at 1260 and 1370°C, respectively. Except at 1150°C, where the N values of cyclic and dynamic fatigue were comparable, the N values of cyclic fatigue at 1260 and 1370°C were also greater than those in the SCG regime (stress rates > 10^{-2} MPa/s) of dynamic fatigue at 1260 and 1370°C. The differences in N values implied that the failure mechanisms and/or crack growth mechanisms for cyclic loading and monotonic loading (including static loading and constant stress rate loading) were not identical.

The loading/unloading in the cyclic fatigue tests appeared to inhibit the creep damage nucleation and accumulation process, in particular at 1260 and 1370°C, and decrease the crack growth rates thus allowing greater stresses to be sustained for similar failure times. This is supported by the cyclic stress-strain and strain-time behavior which will be discussed next.

3.6.1.3 Fast Frequency Hysteresis

Only discrete cyclic stress-strain behavior was recorded for tests under 0.1-Hz trapezoidal loading at 1150, 1260, and 1370°C. The typical cyclic stress-strain behavior for these cases is shown in Fig. 30. For all applied stress levels at 1150 to 1370°C, the cyclic stress-strain behavior remained linear to the final few cycles prior to the failure of specimens. Moreover, the elastic modulus did not significantly change during cyclic fatigue testing. Previous studies have indicated that damage accumulation by formation and growth of creep cavities and microcracks could cause a progressive decrease in Young's modulus and lead to an apparent nonlinear stress-strain relation; see ref. 31 for review. Therefore, the absence of measurable hysteresis in the cyclic stress-strain response implied that little, if any, creep cavitation or microcracking would occur during cyclic fatigue testing at 0.1-Hz trapezoidal loading. This was supported by the monotonic tensile stress-strain behavior in dynamic fatigue tests. At 1260 and 1370°C, nonlinear stress-strain behavior prevailed at stressing rates ≤ 10^{-2} MPa/s where creep rupture was the dominant failure mechanism. When the stressing rates became greater than 10^{-2} MPa/s at 1260 and 1370°C, the stress-strain

ORNL-DWG95-8950

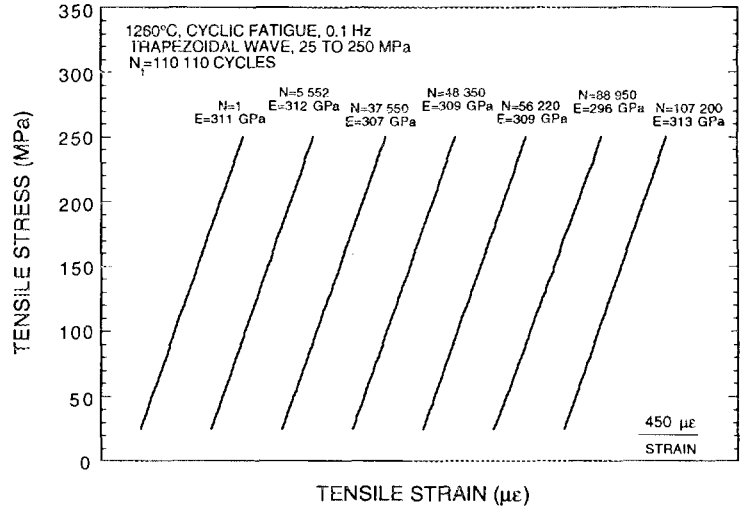

Fig. 30. Cyclic stress-strain behavior of PY6 at 0.1-Hz trapezoidal loading at 1260°C with stress of 25 to 250 MPa.

response was linear, and SCG was the dominant failure mechanism. At 1150°C, the tensile stress-strain curves under all stressing rates (from 10^{-4} to 37 MPa/s) exhibited linear behavior (with nearly identical slopes), and SCG was the prevailing failure mechanism.

Although a hold time at maximum stress was applied in each cycle during the 0.1-Hz trapezoidal loading, no measurable strain increment was observed during the 4.5-s dwell at maximum stress. Apparently, the hold time at maximum stress was shorter than the characteristic time constant for the rate sensitivity of deformation of the viscous intergranular phase, and no significant creep strain was generated; this observation was consistent with the 0.7-h relaxation time constant determined and described in Sect. 3.4.1. If the hold time at maximum stress or the cycle period was comparable with such a characteristic time constant, the true cyclic loading effect might have disappeared, and the prediction of the cyclic fatigue life from the static fatigue data might have been possible. This characteristic time constant is dependent on the viscosity of the intergranular phase and the elastic modulus of the material.

A limited number of cyclic fatigue tests were conducted under 0.1-Hz triangular loading at 1260 and 1370°C with the extensometers in continuous contact with the specimens for the entire tests. In these tests, not only the cyclic stress-strain response but also the strain-time history was obtained. Similar to the results generated at 0.1-Hz trapezoidal loading, the cyclic

stress-strain behavior obtained under 0.1-Hz triangular loading was also free of hysteresis and remained linear to the final few cycles before failure. Such similarity in cyclic stress-strain response between trapezoidal and triangular loading suggests that the loading/unloading procedure in cyclic fatigue tests appears to inhibit the nucleation and/or growth of creep cavities and microcracks no matter what waveform is applied.

The typical strain-time relation for a cyclic fatigue test (0.1-Hz triangular loading with a maximum stress of 100 MPa) compared to strain-time histories of static fatigue tests at 1370°C is shown in Fig. 31. The strain-time curve plotted in Fig. 31 for the cyclic fatigue test was taken at the minimum stress level with additional short, discrete "vertical" segments which represent the cyclic stress-strain response at that particular time. The upper peak of each segment is the corresponding strain at the maximum stress. Since the cyclic stress-strain behavior was linear throughout almost the entire cyclic fatigue test, using other strain values (e.g., those corresponding to the mean or maximum stress level) as the reference strain in strain-time history would simply translate the strain-time curve along the strain axis but would not alter its slope. In Fig. 31, the cyclic fatigue strain-time curve showed a pronounced steady-state regime (or minimum strain rate regime) and the absence of a tertiary regime as compared to the short steady-state regime and dominant tertiary regime in the static

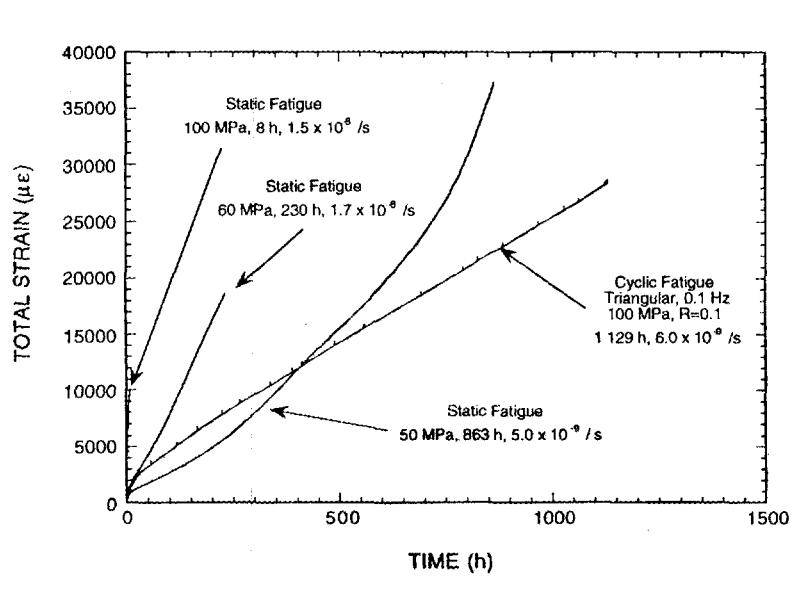

Fig. 31. Comparison of strain-time relations for static and cyclic fatigue of PY6 at 1370°C.

fatigue tests. The absence of the tertiary regime provided more evidence for the conclusion that the normal damage accumulation process in static fatigue was interrupted by the loading/unloading steps in cyclic fatigue.

Although stress-strain hysteresis was not observed during cyclic fatigue testing, an extensive amount of strain ratchetting was found; see Fig. 31. Note that strain ratchetting here refers to the time-dependent progression of the cyclic stress-strain curves along the strain axis. Creep deformation under a tensile mean stress was the first speculation as the mechanism responsible for this strain ratchetting. As shown in Fig. 31, at the early stage of the strain-time history, the cyclic fatigue curve (mean stress = 55 MPa) fell between the two static fatigue curves (applied stresses = 50 and 60 MPa, respectively). This seems to agree with the postulation. However, as no tertiary regime occurred under cyclic loading, the cyclic fatigue curve eventually fell below the static fatigue curve with an applied stress of 50 MPa, suggesting the mechanisms controlling the process of damage accumulation for static and cyclic fatigue were different. More discussion on this phenomenon will follow in Sect. 3.6.2. More evidence supporting this conclusion is presented in Fig. 32 where minimum strain rate was plotted against applied stress in log-log base for both static and cyclic fatigue (0.1-Hz triangular loading) tests. The minimum strain rate for cyclic fatigue was defined as the minimum degree of increase in the strain corresponding to the minimum stress level throughout the test. The mean stress was used as the abscissa for the cyclic fatigue tests in Fig. 32. Fitting the data given in Fig. 32 to a simple power-law relation between minimum strain rate and applied stress ($\dot{\varepsilon}_{min} = A\sigma^n$, A is a constant) yields the following n values: n = 19, 5.6, and 4.4 for static fatigue at 1150, 1260, and 1370°C, respectively, while n = 22 and 10 for cyclic fatigue tests at 1260 and 1370°C, respectively. The significant difference in the corresponding stress exponent values between static fatigue (n = 5.6 and 4.4) and cyclic fatigue (n = 22 and 10) at 1260 and 1370°C indicated the damage mechanisms were different for these two loading histories. Therefore, creep was not believed to be the primary damage mechanism leading to the final failures in cyclic fatigue specimens. The similarity of high n values between static fatigue at 1150°C (n = 19) and cyclic fatigue at 1260 and 1370°C (n = 22 and 10, respectively) suggests a damage accumulation process analogous to SCG was the dominant failure mechanism for cyclic fatigue. Note that the strain-time curves for static fatigue at 1150°C also had a dominant steady-state regime; see Sect. 3.3. In this sense, the observed strain ratchetting for cyclic fatigue at 1260 and 1370°C might have actually reflected compliance changes that resulted from the subcritical extension of a localized damage zone in a manner similar to SCG.

ORNL-DWG95-8952

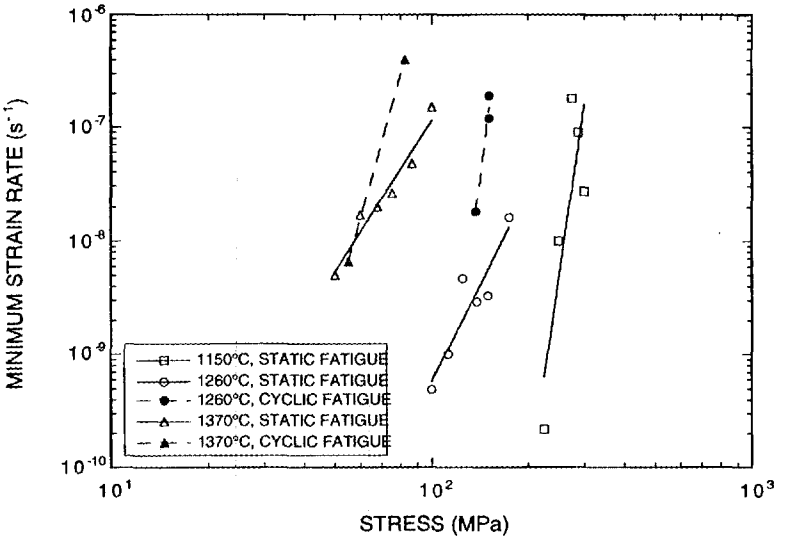

Fig. 32. Comparison of minimum strain rate for static and cyclic fatigue of PY6 at 1150 to 1370°C as a function of static or mean stress.

The minimum strain rates at high applied stress levels were higher under cyclic loading than those under static loading when comparison was made using mean stress for cyclic fatigue, as shown in Fig. 32. However, if maximum stress was employed for the comparison, the minimum strain rates would have been lower in cyclic fatigue compared to static fatigue, which agreed with the stress-life characteristics previously described. Note that using maximum stress as the abscissa for cyclic fatigue tests in Fig. 32 would not have changed the slope (stress exponent) but rather would have translated the curves horizontally toward the right along the stress axis. Therefore, in this case, making comparisons of stress exponent values would have been more useful in examining the identity of failure mechanisms between cyclic and static fatigue.

A Monkman-Grant plot[10] [$t_f = C(\dot{\varepsilon}_{min})^{-m}$; C is a constant] of the minimum strain rate versus time to failure indicated distinct curves for each test temperature of 1260 and 1370°C regardless of loading history, as shown in Fig. 33. The values of m, estimated from the data in Fig. 33, are approximately 1.5 and relatively independent of temperature. The agreement of cyclic and static fatigue data fitted in the Monkman-Grant relationship implied that stress may not be an appropriate controlling parameter for the correlation of static and cyclic fatigue life at

ORNL-DWG95-8953

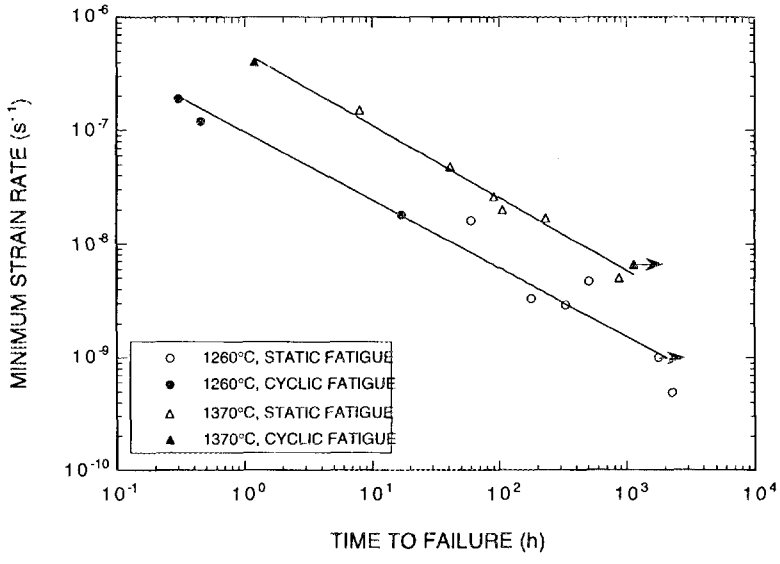

Fig. 33. Comparison of Monkman-Grant-type relations for static and cyclic fatigue of PY6.

elevated temperatures. However, this agreement appeared to contradict the fact that the failure mechanisms in static and cyclic fatigue were different. More microstructural evidence for the different failure mechanisms in cyclic and static fatigue is given next.

3.6.1.4 Fast Frequency Microstructural Changes

Typical fracture surfaces of cyclic fatigue specimens tested at 1150, 1260, and 1370°C are shown in Figs. 34(*a*)-(*c*), respectively. At 1150°C, the fracture surfaces contained well-defined mirror, mist, and hackle regions; see Fig. 34(*a*). A region of apparent SCG from a pre-existent defect was also identified within the mirror region. All of the cyclic fatigue failures at 1150°C were related to pre-existent flaws located in the volume or at the surface. Even though both static and cyclic fatigue failures at 1150°C were due to subcritical crack extension of pre-existent flaws, the comparison of stress-life relations implied that crack propagation rates were less in cyclic loading than in static loading. The lesser damage caused by cyclic fatigue relative to static fatigue in ceramics at elevated temperatures might be related to the viscous intergranular phase; this will be discussed more in Sect. 3.6.2. For example, the effect of bridging the crack surfaces by the viscous intergranular phases could be more

ORNL-PHOTO 10593-95

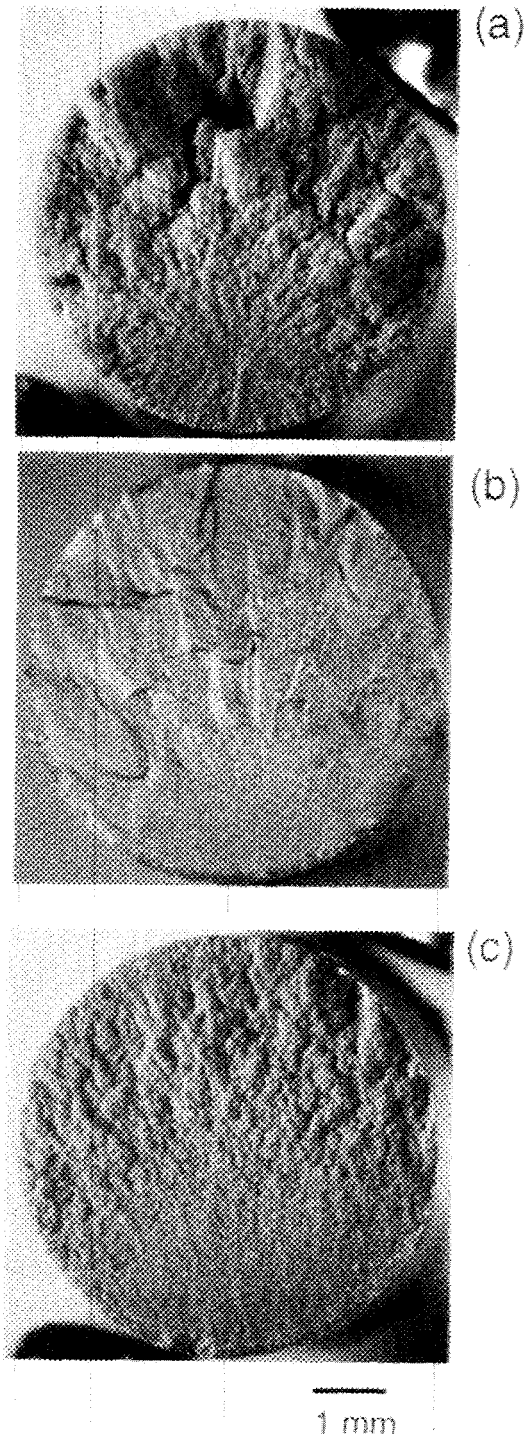

Fig. 34. Typical fracture surfaces of cyclic fatigue (0.1-Hz, trapezoidal waveform) specimens tested at (*a*) 1150°C, σ_{max} = 275 MPa, t_{cf} = 916 h; (*b*) 1260°C, σ_{max} = 250 MPa, t_{cf} = 306 h; and (*c*) 1370°C, σ_{max} = 150 MPa, t_{cf} = 86 *h*.

pronounced in cyclic loading than in static loading under certain conditions.[32] Because of the inability of the viscous ligaments behind the crack tip to relax during the high-frequency cycling, the effective stress-intensity factor at the crack tip is larger under static loading than for cyclic loading with a high frequency or a short hold time at maximum applied stress. In this sense, the crack growth rate is lower in cyclic loading than in static loading. Lower crack growth rates in cyclic loading over static loading with the same maximum applied stress-intensity factor at elevated temperatures have been reported in other ceramics; see ref. 31 for review.

For cyclic fatigue specimens tested at 1260°C, the fracture surfaces still showed the mirror-mist-hackle feature with failure originating from the surface. Only a couple of specimens tested at the highest applied stresses clearly showed the internal pre-existent flaws as the fracture origins. The majority of the specimens had surface-initiated failures, but no clear fracture origins, such as pre-existent defects, could be identified [see Fig. 34(*b*)]. A possible explanation for this phenomenon is that at temperatures ≥ 1260°C, the oxidation rate increased as evidenced by the outer, darker rings on the fracture surfaces shown in Figs. 34(*b*) and (*c*), thereby providing preferred sites for fracture initiation. As observed in other silicon nitrides [see ref. 31 for review], oxidation could have increased the strength by rounding or blunting pre-existent flaws or decreased the strength by producing new flaws such as bubbles, pits, and microcracks in the oxide scale. The effects of oxidation process and products on the mechanical properties are related to such complex factors as impurities and sintering aids, temperature, duration of oxidation, loading conditions during oxidation, and others; see ref. 31 for review. Being that most of the cyclic fatigue failures at 1260°C were initiated at or near the surfaces and their origins could not be clearly identified, it was speculated that oxidation effects generated the failure-causing defects.

The fracture surface features of cyclic fatigue specimens tested at 1370°C look similar to those generated at 1260°C except the mirror regions were larger due to the lower applied stresses; see Fig. 34(*c*). In addition, a small damage zone with greater roughness was observed within the mirror region on the fracture surfaces of a few cyclic fatigue specimens tested at 1370°C. Macroscopically, the feature of this small damage zone does not look like that of the SCG region at 1150°C but is similar to the larger creep damage zone previously identified for the static fatigue specimens tested at 1260 and 1370°C. However, microscopically, no extensive creep cavitation (lenticular, two-grain cavities) was detected throughout the gage sections of cyclic fatigue specimens tested at 1150 to 1370°C; regardless, it is believed that the strain rachetting was accommodated by multigrain junction cavitation. This was one of the major differences in the microstructure between the failed static and cyclic fatigue specimens, in particular at 1260 and 1370°C; see Figs. 35(*a*) and (*b*).

ORNL-PHOTO 10594-95

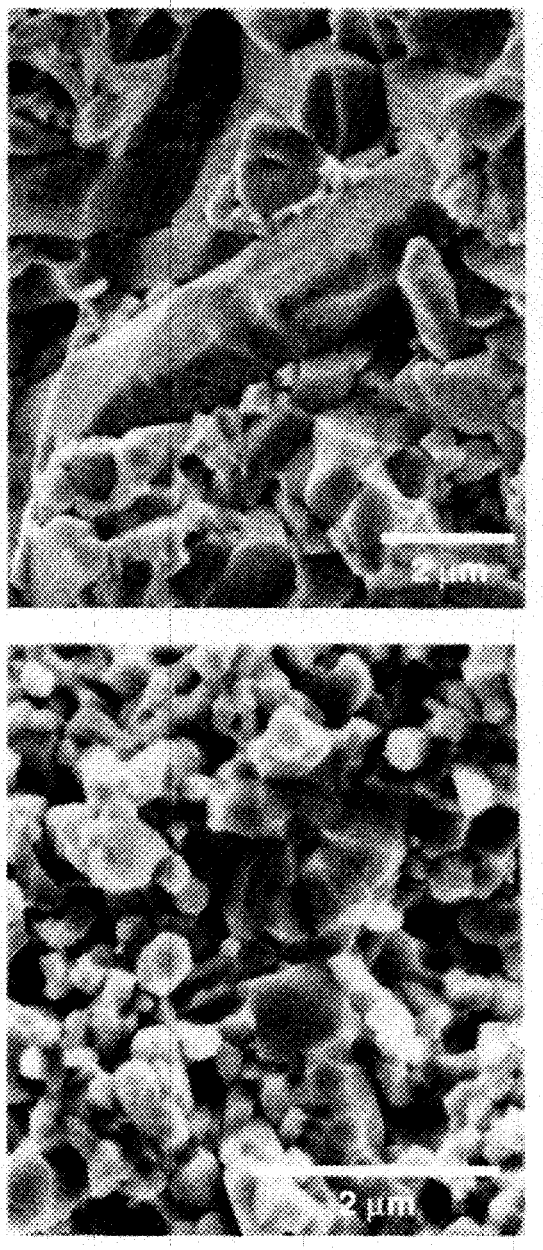

Fig. 35. Comparison of microstructures of specimens tested at 1370°C in (*a*) static fatigue, $\sigma_S = 75$ MPa, $t_{sf} = 90$ h, cavities present; and (*b*) cyclic fatigue, $\sigma_{mean} = 75$ MPa, $t_{cf} = 516$ h, no cavities present.

The origination of this small damage zone from the surface once again implies that surface oxidation might make some contributions to the fatigue failures at 1260 and 1370°C.

Based on these observed features of fracture surfaces and microstructure, a damage accumulation process analogous to SCG was determined to be the dominant failure mechanism for cyclic fatigue at 1260 and 1370°C. This damage accumulation process might have involved the subcritical extension of a localized damage zone originating from the surface, where oxidation-assisted damage or oxidation-modified pre-existent flaws would have provided favorable sites for crack nucleation. The difference of microstructural observations in cyclic and static fatigue was consistent with the macroscopic observations that cyclic fatigue data, generated at 1260 and 1370°C, demonstrated significantly higher values of crack growth exponent, N, and stress exponent, n, over those generated by static fatigue loading at the same temperatures.

The fact that cyclic fatigue specimens did not display such extensive creep cavities as observed in the static fatigue specimens tested at 1260 and 1370°C agreed with the characteristics of stress-life and strain-time results. Although the exact cyclic fatigue mechanisms at 1260 and 1370°C are not clear at the present, unloading in each cycle appeared to play an important role in either suppressing development of creep damage or retarding the accumulation of creep deformation. In Sect. 3.3, solution-precipitation of the silicon nitride in the intergranular phase was suggested as the mechanism for the development of cavities with lenticular shape along two-grain boundaries in PY6 static creep tested at 1260 and 1370°C. The driving force for a typical solution-precipitation mechanism is related to the deviatoric stress (which is the applied stress in uniaxial loading condition); see ref. 31 for review. It is possible that the endurance of such a driving force in each loading period was not long enough for nucleation and/or growth of cavities for selected cyclic loading conditions. This might have resulted from relaxation of local stress concentration at potential sites for cavity development and recovery of viscoelastic deformation during unloading. As mentioned earlier, unloading would have also enhanced the crack surface bridging effect of the viscous intergranular phase and reduced the crack growth rate in cyclic fatigue loading.

Crystallization of the intergranular glass at elevated temperatures can also influence the creep properties in ceramics. This effect is attributed to changes in the volume fraction and viscosity of the grain boundary glass; see ref. 31 for review. In particular, if creep occurred either by a solution-precipitation process or by viscous flow, then a gradual decrease of the amount of glass accompanied by a continuous increase of the viscosity in the interfacial phase would have enhanced the creep resistance. As a complete devitrification of the interfacial glass was rarely observed in silicon nitrides, this crystallization process will continuously alter the composition of retained interfacial glass during creep. Although the

intergranular phases in the triple-point grain junctions of the as-received PY6 specimens were a form of crystalline yttrium silicate, the two-grain boundaries were composed of relatively thin layers of an amorphous yttrium silicate. However, the influence of devitrification on the creep properties of PY6 silicon nitride might be a secondary factor as supported by the presence of pronounced steady-state and tertiary behavior in the strain-time curves of static fatigue results; see Sect. 3.3. In order to better quantify possible time-dependent and stress-state-dependent variations in grain boundary crystallography, more systematic experiments and TEM analyses are necessary for future work; however, PY6 is no longer commercially available, so this work would have to be conducted on another material. It is important to understand how and to what extent the devitrification affects the rate of deformation during creep and how the loading mode, in particular cyclic loading, influences the effective response of the intergranular phases in this HIPed silicon nitride.

3.6.2 Interaction of Creep and Fatigue

The waveforms and frequencies discussed in Sect. 3.6.1 showed no hysteresis on loading and unloading, yet strain rachetting was observed. An effort was made to continue with the cyclic loading studies, but the frequency was decreased (while restricting it to triangular waveforms) and the loading/unloading rate was controlled (to take advantage of the data generated from the dynamic fatigue work described in Sect. 3.5) to more methodically examine the interaction between creep and cyclic fatigue. Motivation existed to model the cyclic creep behavior by examining the utility of extending values and parameters generated from static creep and strain relaxation tests to predict cyclic loading response. The ultimate goal was to be able to take advantage of the more extensive static creep data bases to predict cyclic creep response via an appropriate model.

The methodology for this effort consisted of four subefforts: (1) extracting data that were previously generated on PY6 with static creep and strain relaxation tests, (2) describing how an existing empirical model for static creep was modified to accommodate dynamic or cyclic loading, (3) predicting the cyclic creep response using information from the static and strain relaxation test sources, and then (4) comparing it with experimentally generated cyclic creep responses. Stemming from this work, important insights were made with regard to the role of the anelastic secondary phase on the cyclic creep performance.

Tension-tension cyclic tests were conducted at 1370°C in ambient air (40 to 60% RH and 25°C). A triangular waveform was used in all tests with $\sigma_{min}/\sigma_{max} = R = 0.1$ and $\sigma_{max} = 100$ MPa. Specimens were loaded at one of several frequencies (or stressing rates) that varied over several orders of magnitude. Test frequencies were 0.1, 0.0056, 0.00056,

0.000056, and 0.0000056 Hz, which corresponded to stressing rates of 18, 1, 0.1, 0.01, and 0.001 MPa/s, respectively.

3.6.2.1 Modification of the Pao and Marin Model

The empirical Pao and Marin (PM) model[33] was chosen as the basis because it was already in a form that could readily accommodate variable stressing in its prediction of creep strain. In the PM model, the total isothermal strain (ε_t') at any time is composed of three independent terms: the elastic strain (ε_e), the anelastic or transient or recoverable nonelastic strain (ε_a), and the plastic or nonrecoverable strain (ε_p). This is represented by:

$$\varepsilon_t' = \varepsilon_e + \varepsilon_a + \varepsilon_p \tag{20}$$

where

$$\varepsilon_e = \frac{\sigma}{E} \tag{21}$$

$$\dot{\varepsilon}_a = \frac{d}{dt}(\varepsilon_a) = \alpha\,(C_1\,\sigma^n - \varepsilon_a) \tag{22}$$

and

$$\dot{\varepsilon}_p = C_2\,\sigma^n\ , \tag{23}$$

where σ is the applied stress; E is the Young's Modulus; α is a variable that is equal to the inverse of the relaxation time constant which, in turn, is representative of the viscoelastic behavior; and C_1 and C_2 are constants. Equation (22) was proposed by Pao and Marin because they argued that the transient or anelastic strain is not proportional to the stress, but to stress raised to some power. In addition, Pao and Marin acknowledged in Eq. (22) that the anelastic strain rate decreases with an increase in the anelastic strain and approaches zero when the anelastic strain reaches an asymptotic value. From Eq. (22), the relation containing ε_a can be rewritten for any function of stress that is dependent on time as:

$$\dot{\varepsilon}_a + \alpha\,\varepsilon_a = \alpha\,C_1\,\sigma^n = \alpha\,C_1\,F(t)\ , \tag{24}$$

where F(t) can be used to represent any time-dependent function of stress. Equation (24) is a first-order differential equation, and the solution can be obtained using LaPlace transforms.

The solution is:

$$\varepsilon_a = \alpha C_1 \int_0^t F(t-\xi)\, e^{-\alpha\xi}\, d\xi \quad , \tag{25}$$

where ξ is the shift or translation time (a property of the LaPlace transform). The solution to Eq. (23) is simply:

$$\varepsilon_p = \int \dot{\varepsilon}_p \, dt = C_2 \int_0^t \sigma^n \, dt \quad . \tag{26}$$

For static creep (σ = constant), the PM model represents the total creep strain as:

$$\varepsilon_{t'} = \frac{\sigma}{E} + C_1 \sigma^n \left(1-e^{-\alpha t} \right) + C_2 \sigma^n t \ . \tag{27}$$

This model may ultimately be used for static, dynamic, and cyclic stressing, as long as the correct time dependence of stress is employed. The PM model predicts that the total strain as a function of time [combining Eqs. (21), (25), and (27)] for any static or nonstatic stressing condition is:

$$\varepsilon_{t'} = \frac{\sigma}{E} + \alpha C_1 \int_0^t F(t-\xi)\, e^{-\alpha\xi}\, d\xi + C_2 \int_0^t \sigma^n \, dt \quad . \tag{28}$$

Equation (28) simplifies to Eq. (27) when a constant stress is applied.

The PM model represents the plastic component of creep as being linearly dependent with time (i.e., a viscous-like, permanent creep response that ultimately represents steady-state creep). As shown in Fig. 36, the plastic component of creep is not linear with time for this material, as reflected by the slope of the strain-time plot. Furthermore, the plastic component of creep constitutes a significant contribution to the total creep strain, especially at long times. Figure 20 showed that the magnitude of the total recovered anelastic strain, ε_{am}, becomes more insignificant as the total creep strain increases with time. This is an important observation because it reveals that the plastic strain eventually becomes the dominant contributor to the total strain at 1370°C in PY6 silicon nitride. A time exponent not equal to one and the eventual dominance of the plastic strain on the total creep strain amplify the error associated with the assumption that the plastic strain is linearly dependent with time. To

ORNL-DWG95-8954

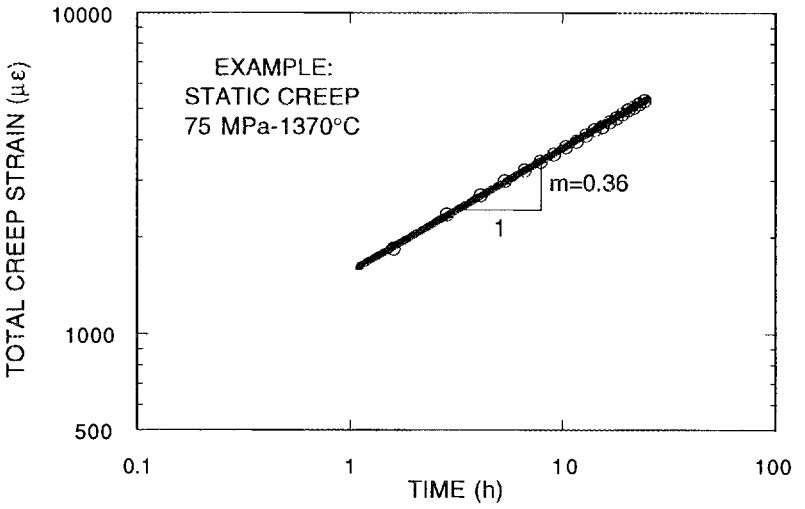

Fig. 36. The plastic component of creep was dependent on time to an exponent less than one. No single constant can be multiplied by the factor t^1 and still satisfactorily describe the experimental data throughout the duration of the test.

address these issues, the MP model was modified by introducing a time exponent (m) parameter into the plastic strain term [i.e., the third term in Eq. (28)]. The modified Pao and Marin (MPM) model then is presented as:

$$\varepsilon_t = \frac{\sigma}{E} + \alpha C_1 \int_0^t F(t-\xi)\, e^{-\alpha\xi}\, d\xi + C_2 \int_0^t \sigma^n t^m\, dt \quad , \tag{29}$$

where ε_t now represents the total strain for any time. The modified plastic term in Eq. (29) will be referred to as ε_{pm}. In addition, a different stress exponent (n') for the modified anelastic strain (ε_{am}) was also introduced to account for the possibility that the stress exponent for the anelastic strain term may not be the same as that for the plastic strain term. As an example of this for the case of an applied static stress, $n' \neq n$ in the second term of Eq. (27). Qualitative descriptions of the independent elastic, anelastic, and plastic components for the MP and the MPM models are schematically shown in Fig. 37.

Pao and Marin Representation:

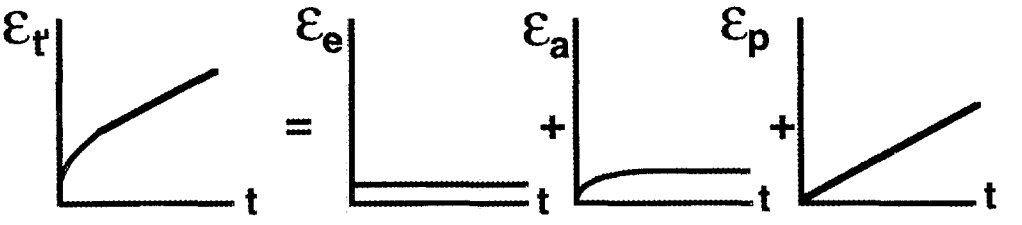

Modified Pao and Marin Representation:

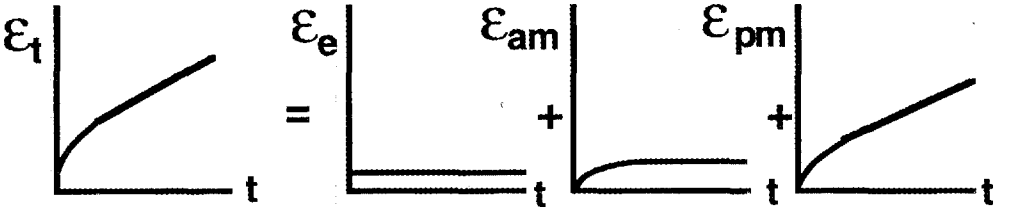

Fig. 37. The plastic term in the Pao and Marin model is linearly dependent with time [m = 1 in Eq. (29)] while it is dependent with time raised to some exponent [m < 1 in Eq. (29)] in the modified Pao and Marin model.

3.6.2.2 Creep During Cyclic Loading

Data obtained from strain relaxation testing need to be incorporated into the analysis. The relaxation time constant, q, was known from Sect. 3.4.1, and α, n', and the constant C_1 were subsequently determined. Alpha, α, is simply the inverse of q (i.e., $\alpha = 1/q$); q = 0.7 h = 2500 s so that $\alpha = 1.4\ h^{-1} = 0.0004\ s^{-1}$. C_1 was determined to be $2.6 \times 10^{-3}/\alpha$ using the information in Fig. 19 and Eq. (25). These obtained values for α, n', and C_1 were used in Eq. (29) for all analyses.

The strain-time histories for the five cyclic fatigue tests are shown in Fig. 38 and compared with previously generated static creep histories. The test matrix, number of cycles, and times to failure are listed in Table 8. As the frequency was slowed, the general trend was toward more extensive total creep strain. Specimens PY6-1 and PY6-2 were tested at the two fastest frequencies, and their strain-time histories fell between the range of the static creep histories of specimens tested at 50 and 60 MPa. The average tensile stress of the triangular waveform used in this study was 55 MPa, so it is not altogether surprising that the

ORNL-DWG95-8955

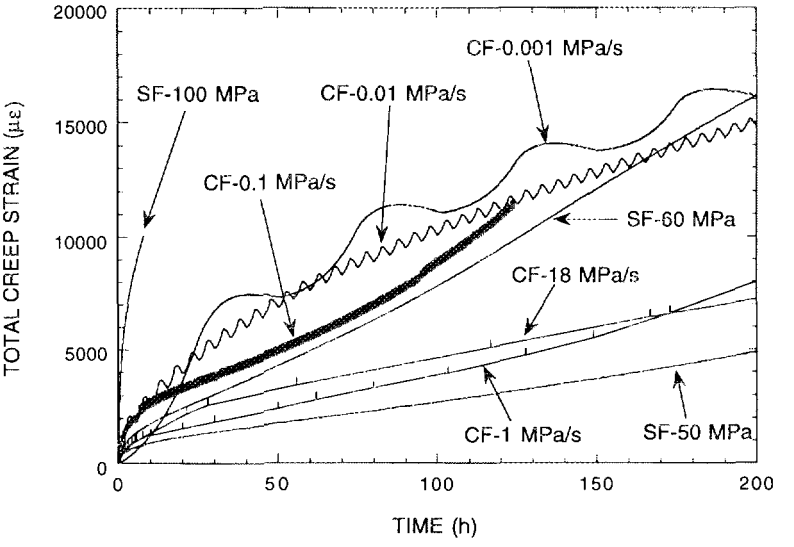

Fig. 38. Strain-time histories of cyclic fatigue (CF) tests are compared with static fatigue (SF) strain histories.

Table 8. Test matrix and cyclic fatigue results. Triangular waveform described by R = 0.1 and σ_{max} = 100 Mpa

Specimen I.D.	Frequency (Hz)	Stessing rate (Mpa/s	No. of cycles to failure	Time to failure (h)
PY6-1	0.1	19	406600*	1129*
PY6-2	0.0056	1	4939	247
PY6-3	0.000056	0.1	248	247
PY6-4	0.000056	0.01	149.5	747.5
PY6-5	0.0000056	0.001	8.4	419

*Test interrupted; specimen did not fail.

strain-time histories of at least some of the tested specimens fell within this range. Specimens PY6-3, PY6-4, and PY6-5 exhibited more total creep than the static creep test at 60 MPa, even though their average stresses were still 55 MPa.

To determine the values of the parameters associated with ε_{pm}, multilinear regression (MLR) was employed on static creep data previously generated on PY6. MLR on creep strain as a function of stress and time was performed on the natural logarithm of the integrand in the third term in Eq. (29) or,

$$\ln(\varepsilon_{pm}) = \ln(C_2) + n \ln(\sigma) + m \ln(t) \ , \qquad (30)$$

for four static creep stresses of 50, 68, 75, and 100 MPa. It was determined that C_2 = 0.000104, n = 3.256, and m = 0.324. It was noteworthy that the stress dependence on the total creep strain was found to be 3.256, while the stress dependence on the minimum creep rate was previously determined to be 4.7 for PY6 at 1370°C, as described in Sect. 3.3. The time exponent of 0.324 is quite close to the one-third predicted by the classical Andrade analysis.[34] The experimental data and the fitted curves are shown in Fig. 39. Even though the total strain is plotted as the ordinate in Fig. 39, the use of it (versus *just* the plastic strain) does not affect the slope determination of the plastic creep time exponent (i.e., m) on the log-log plot because the elastic and anelastic contributions are small and effectively constant over the life of the test. These three values of C_2, n, and m were used in Eq. (29) for analyses.

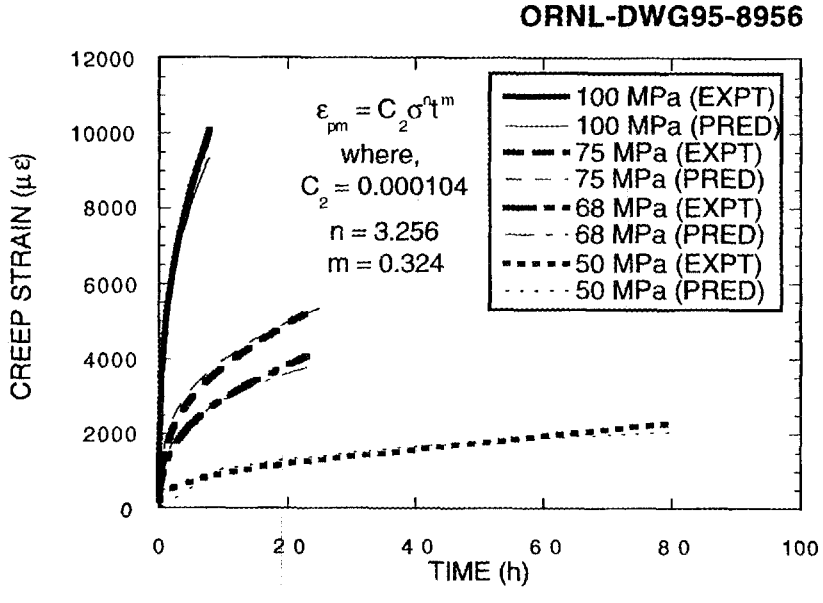

Fig. 39. The variables C_2, n, and m were determined from multilinear regression of total creep strain versus time from static creep histories.

The MPM model described by Eq. (29) was used to numerically fit the experimental data. The values of the parameters used in the analysis were: $\alpha = 1/q = 0.0004\ s^{-1}$, $C_1 = 0.0026/\alpha$, $n' = 1$, $E = 300$ GPa (43.5×10^6 psi), $C_2 = 0.000104$, $n = 3.256$, and $m = 0.324$. As an illustrative example, Figs. 40(*a*) and (*b*) show an arbitrary triangular waveform and the prediction of elastic, anelastic, and plastic strain, and their sum, for one cycle of an arbitrary triangular waveform. Units of MPa and με (or μm/m) were used consistently throughout the analysis.

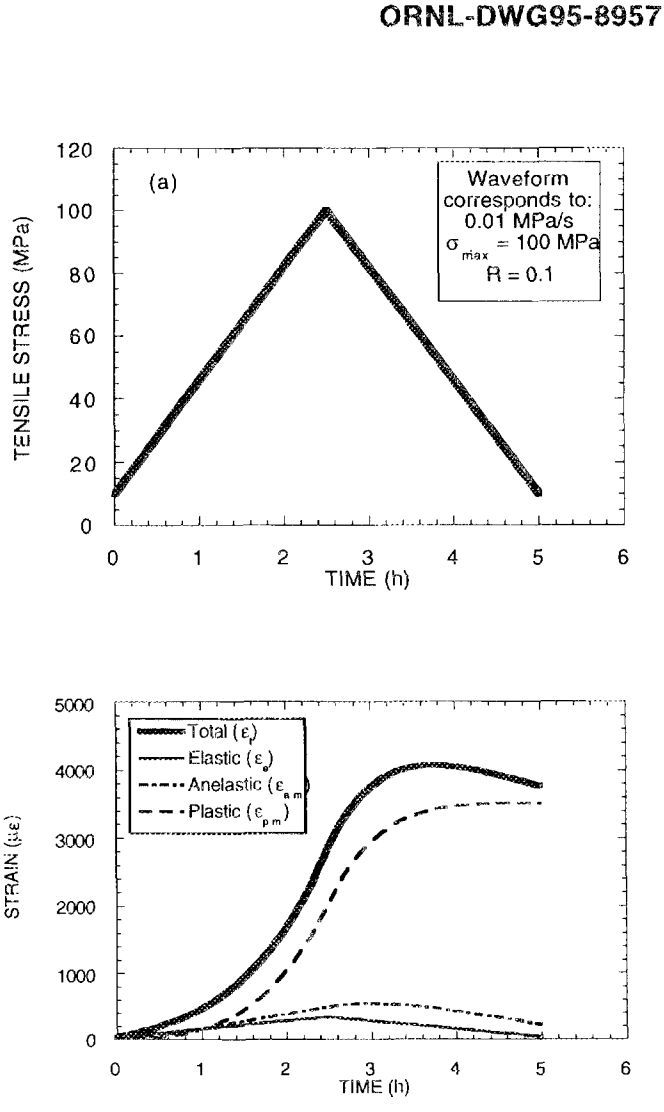

Fig. 40. For an arbitrary triangular waveform (*a*), examples of elastic, anelastic, plastic, and total strain are predicted (*b*) for one cycle using Eq. (29).

The predicted fits for the five specimens tested in this study are shown in Fig. 41 along with the experimental creep strain-time curves. The experimental cyclic creep curves exhibit continued increases in their total strain indicative of creep-rachetting behavior.[35] A large discrepancy between experimental and predicted cyclic response was observed at shorter frequencies or faster stressing rates. This discrepancy lessened as the test frequency was decreased, but it remained substantial for stressing rates equal to and above 0.1 MPa/s, as shown in Figs. 41(*a*)-(*c*). The magnitudes of total creep strain predicted for 0.01 MPa/s were approximately equal to those of the experiment, as shown in Fig. 41(*d*), although the creep rates were dissimilar throughout the test duration. The prediction of the cyclic creep response was quite good for the 0.001 MPa/s test, as shown in Fig. 41(*e*). The predicted total creep strain profile was coincident with the experimental data up to approximately 175 h, but the overall increase in the experimental creep rate after 175 h suggested an onset of tertiary creep. Tertiary creep behavior is a phenomenon that is not addressed in the MPM model.

A reason why the MPM model overpredicts the cyclic creep strain at faster test frequencies and stressing rates is in connection with the changing nature of the material's elastic stress limit. The elastic limit is a function of the stressing rate for PY6 silicon nitride and decreases with decreasing stressing rate at 1370°C. The present reference to an "elastic limit" is somewhat of a misnomer because at elevated temperatures where anelasticity is active, the strain limit describing the onset of nonlinearity is due to elastic plus anelastic effects;[36] however, for the sake of convenience, this limit in the present study is referred to as the "elastic limit."

To illustrate the stressing rate dependence on the elastic limit, the first 800 με (or 0.08% strain) of Fig. 24(*c*) are shown in Fig. 42. Four of the five stressing rates shown match rates used in the present cyclic fatigue study; 37 MPa/s was included as a comparison to show a faster stressing rate response. Although it is somewhat of a subjective determination, the effective elastic limit is somewhere between ≅ 80 to 100 MPa for 1 MPa/s and as low as ≅ 30 MPa for 0.001 MPa/s. Note that these stressing rates were used in the cyclic fatigue tests for specimens PY6-2 and PY6-5, respectively. The MPM model predicts a plastic contribution to the total strain for *all* stresses during each cycle; whereas in the experimental case, there may only be a plastic strain contribution for stresses *above* the elastic limit for that corresponding stressing rate. For cyclic tests PY6-1, PY6-2, and PY6-3, the frequencies or stressing rates were *fast enough* that there was not an appreciable amount of time above the elastic limit for each stressing rate to accumulate the total strain predicted by the MPM

ORNL-DWG95-8958

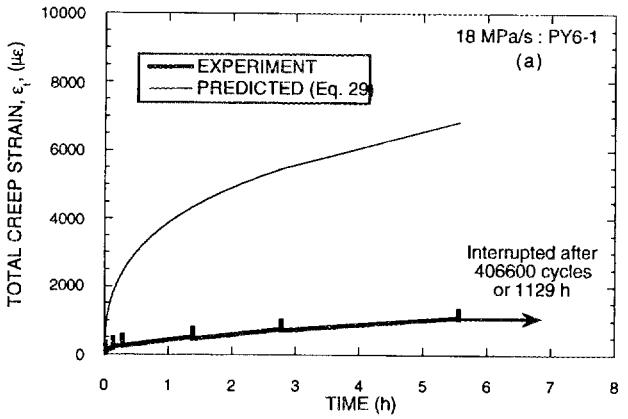

(*a*)

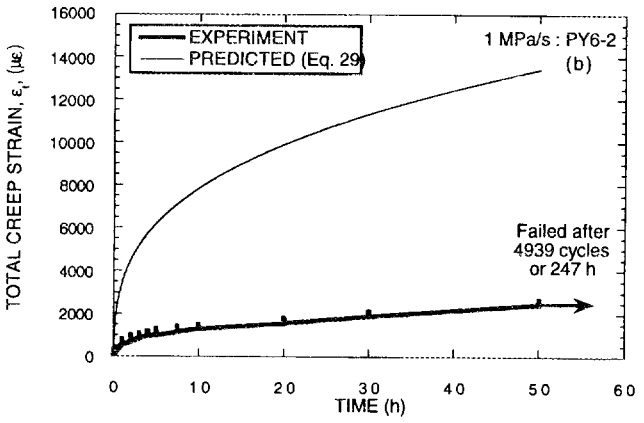

(*b*)

Fig. 41. Experimental cyclic creep strain as a function of time is compared with data predicted using the MPM model for specimens (*a*) PY6-1, 0.1 Hz, 18 MPa/s; (*b*) PY6-2, 0.0056 Hz, 1 MPa/s; (*c*) PY6-3, 0.00056 Hz, 0.1 MPa/s; (*d*) PY6-4, 0.000056 Hz, 0.01 MPa/s; and (*e*) PY6-5, 0.0000056 Hz, 0.001 MPa/s.

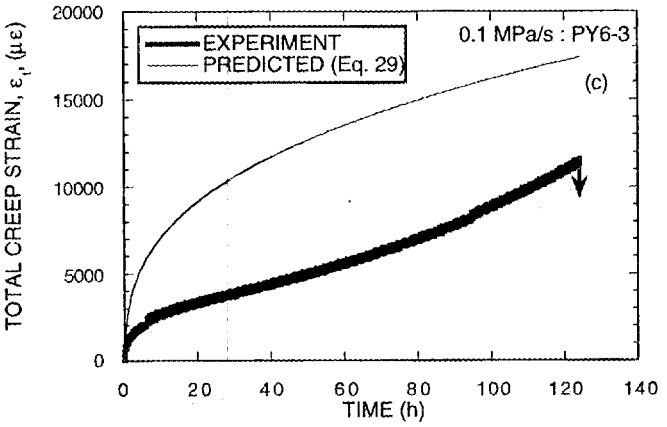

(*c*)

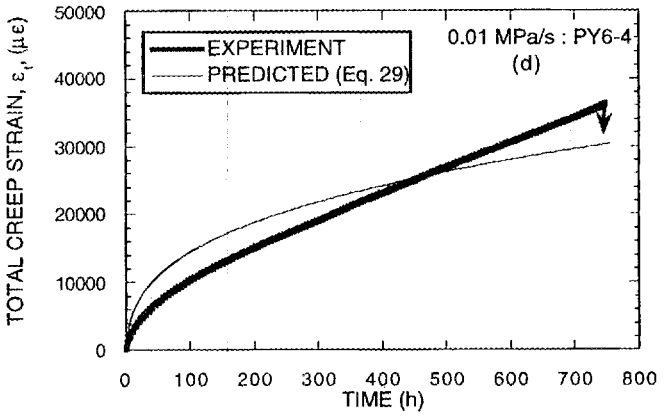

(*d*)

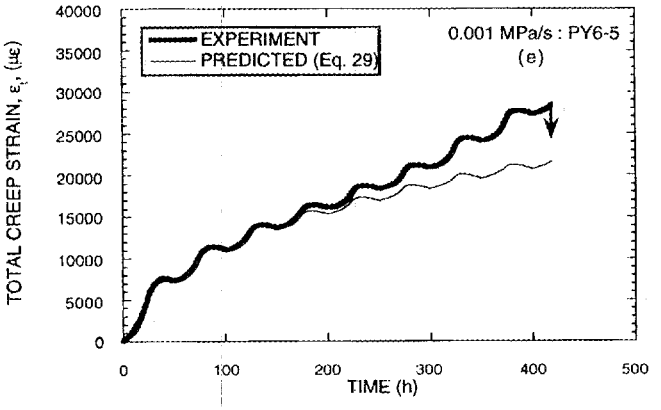

(*e*)

Fig. 41. (Continued)

ORNL-DWG95-8960

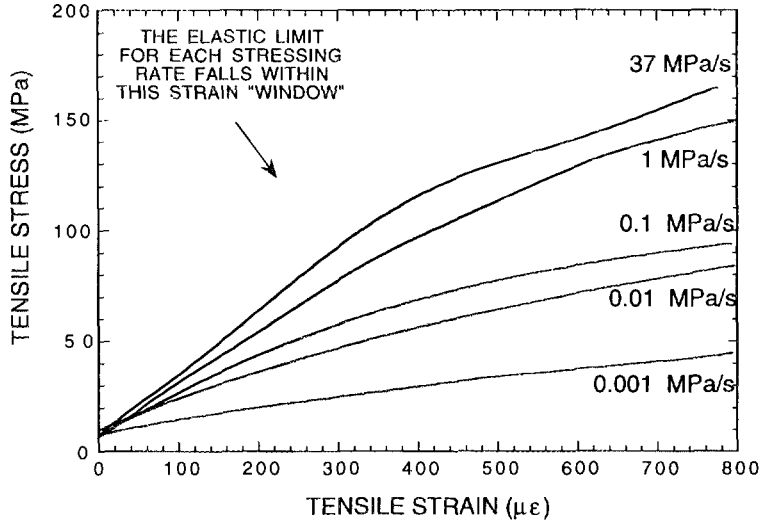

Fig. 42. The elastic limit of PY6 silicon nitride is a function of the stressing rate. As the stressing rate is decreased, the elastic stress limit decreases and plastic creep occurs at lower stresses. Curves shown are taken from Fig. 24(*c*).

model. This lack of acknowledgment of the elastic limit will cause the MPM model to consistently overpredict the total cyclic creep strain at faster frequencies or stressing rates. At the slower stressing rates of 0.01 and 0.001 MPa/s, the relatively low elastic limit, coupled with the long times that the stress in each cycle is in excess of it, results in more representative predictions of total cyclic creep strain.

Instead of a critical or elastic stress limit argument, the perspective of a critical strain to explain the cyclic creep behavior also may be used. In this case, plastic strain only accumulates if ε_{am} is saturated or reaches some threshold anelastic strain (i.e., ε_{pm} increases only if $\varepsilon_{am} = \varepsilon_{a'}$ or $\varepsilon_{am} = \text{constant} \bullet \varepsilon_{a'}$). The basis for this comes from at least two sources. In Sect. 3.6.1, it was experimentally found that cyclic loading at 0.1 and 10 Hz at 1370°C always yielded less accumulated creep strain and longer lifetimes than static loading at comparable stresses. It was speculated that the viscoelastic or anelastic nature of the secondary phase acted in concert with the fast cyclic loading and unloading to slow the normal accumulation of creep damage. In a second study, cavitation (a permanent or plastic damage mechanism) was shown to account for as much as 85% of the total creep strain;[37] however, the attainment of a small amount of accumulated strain was necessary before cavities were

detected. Both these studies support the claim that a critical strain (in this case, an anelastic strain) needs to be attained in order for plastic deformation to become active. This critical strain may indeed be stress dependent in a similar fashion to the dependence of ε_a' on the $\Delta\sigma$ from the strain relaxation studies discussed in Sect. 3.4.1. If the anelastic strain is saturated, then no more anelastic strain can be accommodated, and high local stress intensities may develop which act to nucleate cavities. The MPM model does not take into account that the onset of plastic deformation requires a threshold of anelastic strain to be met; consequently, it will overpredict the plastic strain at faster frequencies or stressing rates where the critical strain is not attained. Indeed, there is *some* accumulation of plastic strain evident in Figs. 41(*a*)-(*c*) for the faster frequencies; therefore, for this argument to be valid, an anelastic strain threshold must have been met for each cycle although the corresponding accumulation of plastic creep was relatively small. Of the arguments based on the plastic strain first requiring the attainment of a critical stress or strain, the latter is more versatile because it can more easily reconcile plastic deformation under fast-frequency cyclic and static loading conditions. More detail on this discussion may be found in ref. 38.

3.7 FLEXURAL DYNAMIC FATIGUE

3.7.1 Motivation of Testing in Air and Inert Environments

From Sect. 3.5, SCG was reported as the dominant mechanism at stressing rates greater than or equal to 10^{-1} MPa/s, while the evolution of a damage region was the time-dependent failure mechanism when the stressing rates were slower than or equal to 10^{-2} MPa/s. This damage region was examined on tensile creep-rupture specimens tested at 1370°C described in Sect. 3.3. The failures were reported to initiate at the surface of the specimen, suggesting that oxidation was associated with its formation. In Sect. 3.3, this mechanism was referred to as a creep damage zone; however, this terminology is misleading for it was likely that its formation was also a result of oxidation effects. The formation of this damage zone was recreated in flexural dynamic fatigue testing at 1370°C, and it became defined as a *stress-corrosion cracking (SCC) damage zone* and includes the sum of all effects that result from stress and oxidation or corrosion.

The present effort specifically examined the relationship between oxidation and the evolution of an SCC damage zone in PY6. The primary goal was to examine if and how the inhibition of oxidation affects the evolution of damage, which may have included mechanisms such as creep and SCG. To fulfill this, parallel flexure dynamic fatigue tests were conducted in ambient air and inert environments at 1370°C in an effort to characterize the evolution and nature of this SCC damage zone in the presence or absence of oxidation.

The stressing rates were calculated by taking into account both the specimen geometry and a computer-controlled constant loading rate. Bend bar dimensions were 3 × 4 × 50 mm, and the tensile side edges were beveled. Flexural dynamic fatigue tests were conducted at 1370°C in flexure and in ambient air (25°C, 30 to 50% RH); argon; and nitrogen using four-point bend fixtures with SiC loading pins (diam = 6.35 mm). Specimens were loaded to failure with one of the following stressing rates: 37 MPa/s (air, Ar, and N_2); 1 MPa/s (air); 0.1 MPa/s (air, Ar, and N_2); 0.01 MPa/s (air); 0.001 MPa/s (air, Ar, and N_2); 0.00036 MPa/s (Ar and N_2); and 0.0001 MPa/s (air).

The environmental flexure testing was conducted within an alumina retort (diam = 100 mm) surrounded by a resistively heated clamshell furnace. The whole unit was vertically mounted on a universal testing machine. The supplied inert gases were 99.999% pure, and this was independently verified with an oxygen analyzer that continually measured the oxygen content of the inert gas that entered the retort during the test (400 to 800 ppb O_2 measured). A slight positive pressure of approximately 2 kPa was maintained in the chamber while the flow rate of the inert gas was adjusted to approximately 0.5 mL/s. The chamber was purged a minimum of three times for each test. The atmospheric conditions described were in effect by the time the chamber and specimen were heated to 300 to 350°C.

Fractography was undertaken after testing and included both optical microscopy and SEM. The fracture surfaces of specimens tested in ambient air tended to oxidize at 1370°C, which inhibited microstructural studies. This was overcome by refracturing the tested bend bars at room temperature at their centers. Post-testing specimen curvature was identified through the use of an optical compactor to determine whether or not the specimen had undergone creep.

The flexure strength, S_{flex}, of the specimens was calculated according to beam bending theory:

$$S_{flex} = (3/2) \cdot P \cdot (S_O - S_i) / (b\, h^2) \quad , \tag{31}$$

where P is the maximum sustained load; S_O and S_i are the outer and inner spans of the four-point bend fixtures (40 and 20 mm, respectively); b is the specimen width; and h is the specimen height. If permanent curvature was identified in the tested specimen, then the flexure strength described in Eq. (31) was adjusted after the analysis of Hollenberg et al.:[39]

$$S_{flex}' = S_{flex} \cdot (2n+1) / (3n) \quad , \tag{32}$$

where S_{flex}' is the adjusted flexure strength for crept specimens, and n is the flexure creep exponent. It must be emphasized that this adjustment represents only a first approximation; uncertainty may be introduced because of neutral axis shifting and beam deflections which may be excessive.[39] In spite of this uncertainty, a flexure creep exponent for this silicon nitride material at 1370°C has been measured to be 3.1 (ref. 3) and was used in Eq. (32).

If a material is susceptible to SCG, then its strength will decrease with decreasing stressing rate. By appropriately applying fracture mechanics with dynamic loading, SCG parameters may be determined that will mathematically represent this susceptibility. The crack velocity (V) during SCG is often described in the power-law form: $V = A (K_I / K_{IC})^N$, where K_I is the applied stress intensity, K_{IC} is the critical stress intensity, and A and N are constants. When combined with the Griffith criterion ($\sigma = Y \bullet K_{IC} \bullet c^{-1/2}$, where σ is the applied stress, Y is a specimen geometry/crack shape parameter, and c is the crack length), an equation that relates flexure strength and stressing rate may be derived, namely:

$$S_{flex}'^{(N+1)} = C \dot{\sigma} \quad , \tag{33}$$

where S_{flex}' is the adjusted flexure strength from Eq. (32), $\dot{\sigma}$ is the stressing rate, N is the SCG exponent, and C is a constant. Equation (33) is quite similar to Eq. (13) that was used for the tensile dynamic fatigue analysis. The adjusted flexure strengths were plotted as a function of stressing rate on a log-log scale with the slope equaling 1/(N + 1). Lower values of N describe greater SCG susceptibility.

3.7.2 Effect of Oxidation on Stressed Components

The results[40] of the adjusted flexure strengths as a function of stressing rate for the three test environments are shown in Fig. 43. The flexure strengths of the specimens tested in argon and nitrogen were satisfactorily fitted by a single curve. The curve's horizontal nature signifies that the PY6 was not susceptible to SCG in these two environments. Conversely, the flexure strengths of PY6 specimens tested in ambient air exhibited stressing rate dependence, represented by the relatively small values of the SCG exponents. A single, fitted curve did not adequately describe the adjusted flexure strengths over the whole range of stressing rates, a phenomenon which was similar to that described in Sect. 3.5.

ORNL-DWG95-8961

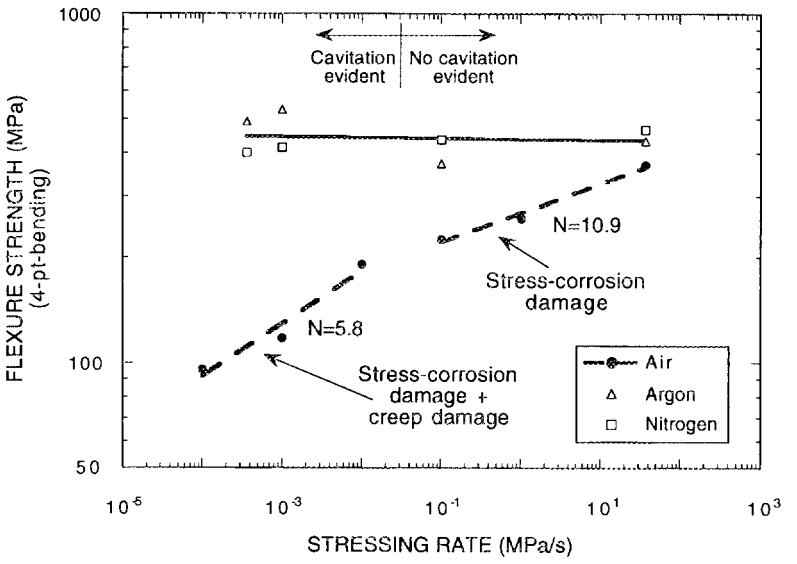

Fig. 43. The adjusted flexure strength of PY6 silicon nitride at 1370°C was found to be independent and dependent of the stressing rate in inert environments and ambient air, respectively.

Optical fractography showed evidence of the production of an SCC damage zone on all the specimens tested in ambient air. The SCC damage zone originated at the tensile side of each bend bar. The transition region from this SCC damage zone to fast fracture on a specimen tested at 10^{-4} MPa/s in ambient air is shown in Fig. 44. This SCC damage zone typically was quite large (≅ 0.1 to 2 mm) and should not be confused with a passive oxidation layer (≅ 3 to 4 μm thick) observed on the surfaces of specimens tested in ambient air. At the scale shown in Fig. 44, the rough topography of the stress-oxidation damage zone is quite different from the smooth surface where fast fracture had occurred. At higher magnifications (> 1000×) however, no conclusive differences were observed in the microstructures in that they both predominantly exhibited intergranular fracture. These observations were consistent in all the specimens tested in ambient air.

A word of caution is worth mentioning at this point. The SCG exponent, N, is used in the present study to show qualitative trends between adjusted flexure strengths and stressing rates for the three test environments. However, the SCG model reflected by

ORNL-PHOTO 10595-95

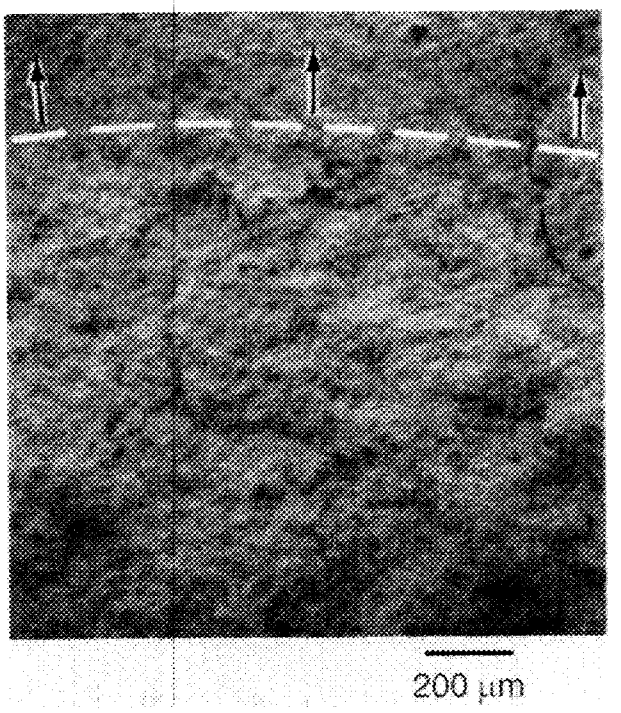

Fig. 44. The transition from the stress-corrosion cracking (SCC) damage zone (lower half) to fast fracture (upper half) is shown on the specimen tested in ambient air at 10^{-4} MPa/s. Note the rough versus smooth topography of the SCC damage and fast fracture zones, respectively. The surface shown was etched, and the arrows describe the crack propagation direction.

Eq. (33) is usually associated with subcritical crack propagation stemming from an intrinsic flaw, whereas the SCC damage zone observed in these specimens tested in ambient air appears to initiate along the whole tensile side of each bend bar and *not* from a singular intrinsic flaw. In this sense, the N values cited above reveal qualitative and not quantitative trends.

The advancement or extent of the SCC damage zone increased with decreasing stressing rates, and the resulting strengths dropped accordingly. The fracture surfaces of specimens tested at 10^{-2} and 10^{-4} MPa/s are shown in Fig. 45 and had adjusted flexure strengths of 191 and 96 MPa, respectively. Although it is not seen at the magnification in

ORNL-PHOTO 10596-95

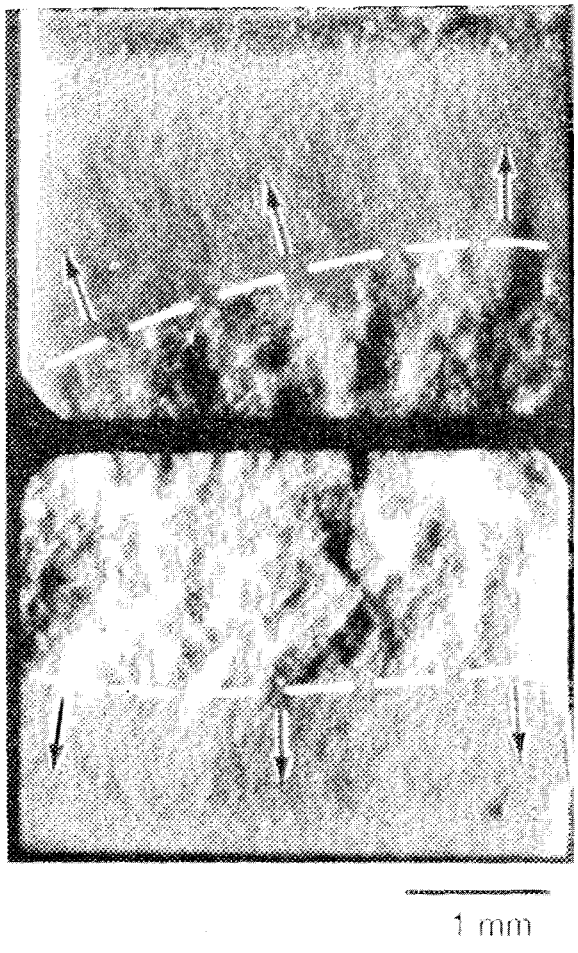

Fig. 45. A stress-corrosion cracking (SCC) damage zone was observed on the fracture surfaces of all specimens tested in ambient air at 1370°C. The top and bottom specimens shown were tested at 10^{-2} and 10^{-4} MPa/s, with adjusted flexure strengths of 191 and 96 MPa, respectively. Tensile sides are beveled, and arrows show crack propagation direction.

Fig. 39, both these samples contained creep damage *within* the SCC damage zone. The SCC damage zone in these specimens was quite obvious and typically extended upwards along the whole tensile side of the fracture surface.

The SCC damage zone present on specimens tested in ambient air was not identified during fractography on those specimens tested in inert environments. A comparison of fracture surfaces of specimens tested at 10^{-3} MPa/s in air and argon is shown in Fig. 46. The SCC damage zone on the specimen tested in ambient air is quite evident in Fig. 46. The fracture surfaces of specimens tested in inert atmospheres typically contained flaws that ultimately produced fast fracture markings; note the corresponding adjusted flexure strengths of the specimens. It is evident that the production of this stress-oxidation damage zone in ambient air severely diminished the flexure strength of this material.

Polished cross sections of flexure specimens tested in ambient air exhibited a ring similar to that observed on polished tensile specimens (see Sect. 3.3.2). The ring is presumably due to long-term oxidation of the silicon nitride with the ambient environment. This statement is justified because flexure specimens tested in an inert environment *did not* show an analogous ring. A polished cross section of a bend bar tested in ambient air is compared with another bend bar that was tested in argon at 1370°C in Fig. 47. Consistent with the presence or absence of an outer ring for specimens tested in ambient air or argon, respectively, was the fact that SCC damage was only observed in specimens tested in ambient air. It is speculated that this outer ring contains a volume of material that has microstructurally changed due to the long-term oxidation with the ambient air. SCC appears to grow in this same volume of changed material. This suggests that if the effects of long-term oxidation can be slowed, then SCC will, in turn, be slowed, and higher strengths of PY6 should be the result in ambient air.

Creep damage was commonly observed at a microscopic scale in the form of cavitation near the tensile faces of the bend bars. Lenticular-shaped, two-grain junction cavities were typically observed and ranged in size up to 200 nm. Multigrain junction cavities were observed also and tended to be two to five times larger than the lenticular-shaped cavities. Cavitation was evident on all bend bars tested at stressing rates slower than 10^{-1} MPa/s. In addition, the specimen tested in air at 10^{-1} MPa/s did show some evidence of cavitation, but only after a lengthy search. The content of cavitation was not quantified, but it was merely identified in order to show that a creep damage mechanism was active.

It is apparent that cavity formation in this material at 1370°C will only occur if some minimum tensile strain is exceeded for a sufficient amount of time; this is consistent with the strain-saturation argument posed in Sect. 3.6.2. Since the Monkman-Grant-type relationship

ORNL-PHOTO 10597-95

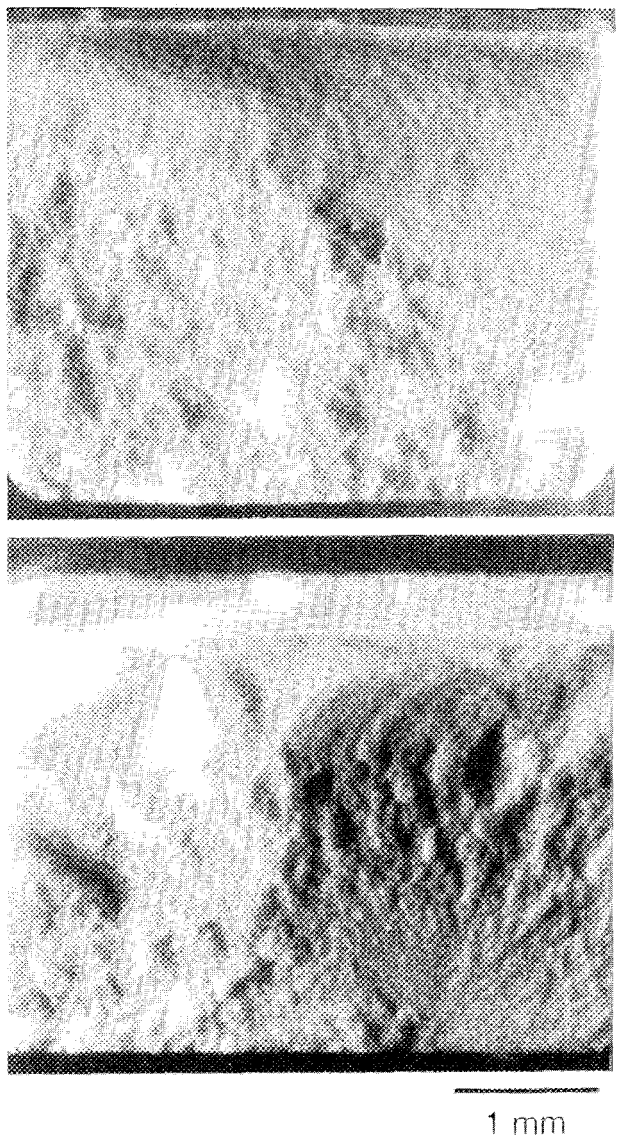

Fig. 46. The stress-corrosion cracking damage zone was formed when specimens were tested in ambient air (top) but not when tested in inert atmospheres (argon tested - bottom). Specimens shown were tested at 10^{-3} MPa/s, and the adjusted flexure strengths were 118 and 530 MPa, respectively. Under similar conditions, the specimen tested in nitrogen had a strength of 413 MPa. Tensile sides are beveled.

ORNL-PHOTO 10598-95

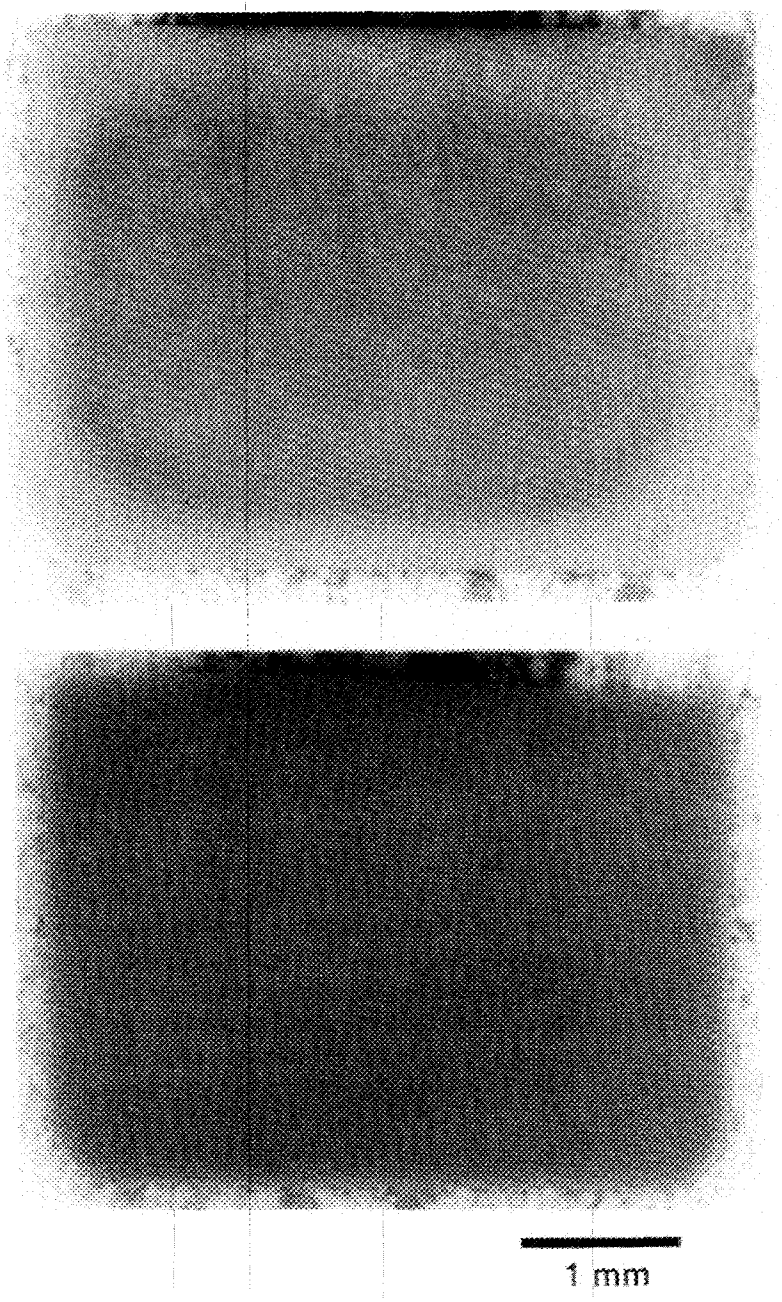

Fig. 47. Flexure specimens tested in ambient air showed a lightly shaded ring around their perimeters (top), while specimens tested in argon showed no analogous ring (bottom). Specimens shown were tested at 0.001 MPa/s.

was shown to provide a good description of the strain rate dependence of fatigue life for PY6 tested in tension at 1370°C, it is suggested that, at the slower stressing rates where cavitation was produced, the creep damage mechanism may provide an added contribution to the formation of the SCC damage zone and further reduce the specimen lifetime as a consequence. This phenomenon is supported by the lower N values for specimens tested in ambient air at stressing rates slower than 10^{-1} MPa/s.

The validity of the reported stressing rates used in flexure was examined. The stressing rates were initially calculated using the specimen geometry and a constant loading rate, with the assumption that the specimen elastically responded to an applied loading rate. The onset of creep (and its effect on the stressing rates) effectively reduces the magnitude of the reported stressing rates according to the Hollenberg ratio (see ref. 39). This ratio was previously used to adjust the flexure strengths as described in Eq. (32). For those specimens that crept, the applied stressing rates were effectively reduced by $\cong$ 22% for the duration of their creep deformation using a flexure creep exponent of 3.1. In terms of stressing rates, this 22% reduction is insignificant when viewed on a logarithmic scale such as that used in Fig. 43.

Cavitation is shown in Fig. 48 on the specimen tested in nitrogen at a stressing rate of 10^{-3} MPa/s; specimens tested in air and argon at 10^{-3} MPa/s contained similar cavitation. All three specimens showed creep behavior, as evidenced by this creep damage, but only the specimen tested in air also contained the macroscopic stress-oxidation damage zone. The fact that all three specimens crept, but only the specimen tested in air had this stress-oxidation damage zone, is strong evidence that oxidation ultimately caused the formation of this stress-oxidation damage zone, which consequently reduced the flexure strength.

4. SUMMARY OF PROGRAM

The tensile strength of the PY6 exhibited little temperature sensitivity for temperatures below 1000°C. However, the strength decreased sharply at temperatures above 1000°C.

The stress dependencies of the creep rates measured at 1260 and 1370°C were consistent with a diffusional creep mechanism accompanied by cavitation, grain separation by viscous flow, and possibly grain boundary sliding. The creep rates at 1260 and 1370°C exhibited a very strong temperature sensitivity as reflected by the high activation energy of 1102 kJ/mole. This temperature sensitivity was attributed to either a large temperature dependency of the viscosity or the activation of additional volume-generating mechanisms as the temperature increased from 1260 to 1370°C.

ORNL-PHOTO 10599-95

Fig. 48. Lenticular cavitation was observed in specimens when $\dot{\sigma} < 0.1$ MPa/s. The microstructure of a nitrogen-tested specimen stressed at 10^{-3} MPa/s is shown. Specimens tested in air and argon at this stressing rate showed similar cavitation. Specimens were refractured at room temperature after testing but prior to microscopy in order to reveal the microstructure.

The tensile fatigue data revealed two distinct failure mechanisms. At 1150°C, failure was controlled by an SCG mechanism. At 1260 and 1370°C, the accumulation of creep damage in the form of grain boundary cavities dominated the fatigue behavior. Oxidation also appeared to play a significant role in the damage accumulation process. In this temperature regime, the fatigue life was controlled by the minimum creep in accordance with a Monkman-Grant-type relation.

Estimates of n and Q_C based upon the flexural creep data were significantly less than those generated from tensile tests. This poor agreement was attributed to the simplified assumption of sign-independent creep rates used to calculate the flexural creep strains. As a

consequence of this, the validity of many of the early flexural creep studies on silicon nitride, which neglected the differences between the tension and compression creep response, is questionable.

A modified Monkman-Grant relationship was developed that acknowledges and predicts temperature dependence of the relationship between time to failure and minimum creep rate (i.e., temperature-dependent stratification). The analysis also permits the consideration that the activation energies for static creep and fatigue may not be equivalent.

The Sherby-Dorn temperature-compensated time to failure and minimum creep rate parameters were obtained from static creep tests at 1150, 1260, and 1370°C. A bilinear fit of the data was found to be necessary. Prediction of time to failure and minimum creep rate at 1200°C was made using this information and was compared with actual times to failure and minimum creep rates from confirmatory static creep tests, and the match was found to be very good.

Strain relaxation (creep recovery) testing was used to determine that the relaxation time constant of PY6 at 1370°C was 0.7 h. This information is needed for prediction of accumulated dynamic or cyclic strain. The total amount of recoverable strain was found to be linear with the change in stress of unloading and followed the relation $\varepsilon_a \approx 6 \cdot \Delta\sigma$ for 54 MPa $\leq \Delta\sigma \leq$ 90 MPa, where ε_a is in units of microstrain. For a PY6 specimen that is static creep tested at 1370°C, the anelastic contribution to the total creep strain becomes more insignificant with time.

Stress relaxation tests conducted on PY6 at 1370°C showed that this technique may be used with caution to describe creep rate-stress relationships. The methodology of this technique is mathematically elegant. However, caution must be exercised when comparing creep rate-stress data that this technique generates with similar data generated via static creep tests. Minimum creep rates for static creep tests are commonly reported while the creep rates determined using stress relaxation testing will depend on the value (and its proximity in the primary or secondary creep regime) of the strain held constant during the stress relaxation test. For a sense of how the stress in PY6 relaxes, a test conducted with an initial stress of 85 MPa at 420 με at 1370°C relaxed to an asymptotic stress of 25 ± 5 MPa in about 1 to 2 h.

Dynamic fatigue results showed that the fatigue susceptibility of PY6 increased with temperature in the range of 1150 to 1370°C. Comparison of effective time to failure and microstructural observations indicated that static and dynamic fatigue results at 1150°C can be correlated in terms of an SGC model. A transition in the fatigue failure mechanism from SCG to creep rupture appeared to occur at stressing rates $\leq 10^{-2}$ MPa/s for 1260 and 1370°C. The existence of this transition is supported by macroscopic nonlinear stress-strain curves and

microscopic fractographic evidence. Caution is advised in the application of the SCG model to correlate static and dynamic fatigue behavior in ceramics at elevated temperatures where creep processes and crack blunting can compete with SCG.

Comparison of stress-life relations between static and cyclic fatigue indicated that cyclic loading provided more extensive time to failure for PY6 at 1150 to 1370°C. The tensile static and cyclic fatigue data could not be described by a universal SCG model at temperatures ≥ 1150°C. Caution is advised in applying the SCG model to predict the stress-life relation for cyclic fatigue based on static fatigue data. This is especially pertinent at elevated temperatures where mechanisms other than SCG, such as creep processes, viscoelastic effects, and oxidation, may contribute to the final failure.

The lack of measurable hysteresis in cyclic stress-strain behavior implied that little, if any, creep damage such as cavitation and microcracking was generated during cyclic fatigue testing. In this sense, strain ratchetting observed during cyclic fatigue testing was probably caused by a damage accumulation process analogous to SCG. This conclusion is supported by the greater values of crack growth exponent, N, and stress exponent, n, for cyclic fatigue over those generated by static fatigue at 1260 and 1370°C where creep rupture was the dominant failure mechanism. Moreover, microstructural analyses provide no evidence of extensive creep cavities in cyclic fatigue specimens.

Cyclic loading of PY6 at elevated temperatures generated failures whose kinetics could not be interpreted in terms of static tests. Unloading might play a significant role in extending the time to failure for cyclic fatigue over static fatigue under the same maximum applied stress. The act of unloading could inhibit development of creep damage or retard accumulation of creep deformation resulting from the relaxation of local stress concentration and recovery of viscoelastic strain. As supported by the microstructural observations, it is likely that the primary failure mechanism for cyclic fatigue at 1260 and 1370°C might involve the subcritical extension of a localized damage zone originating from the specimen surface where oxidation-assisted damage or oxidation-modified pre-existent flaws provided a favorable site for crack nucleation.

The amount of tension-tension cyclic creep strain was found to increase as the frequency or stressing rate of a triangular waveform (σ_{max} = 100 MPa and R = 1, average stress of cycle = 55 MPa) decreased for PY6 at 1370°C. For frequencies of 0.1 and 5.6×10^{-3} Hz (stressing rates of 18 and 1 MPa/s, respectively), the amount of cyclic creep strain fell within a range bounded by static creep responses of 50 and 60 MPa. The total cyclic creep strain increased continually for comparable times for frequencies of 5.6×10^{-4}, 5.6×10^{-5}, and 5.6×10^{-6} Hz (stressing rates of 0.1, 0.01, and 0.001 MPa/s, respectively).

An MPM model was successful at predicting representative low-frequency, cyclic creep responses from data and creep parameters extended from static creep and strain relaxation tests. The model predicted cyclic creep strains similar to those experimentally determined for 5.6×10^{-5} Hz. It very accurately predicted the cyclic creep response for 5.6×10^{-6} Hz.

The MPM model did not satisfactorily predict cyclic creep response at frequencies equal to and faster than 5.6×10^{-4} Hz. The model overpredicted the cyclic creep strains at these faster frequencies. The model predicts the contribution of plastic strain for all stresses in the cyclic waveform used; however, it is evident that an elastic stress limit or an anelastic strain threshold needs to be attained *prior* to the accumulation of plastic strain.

The flexure strength of PY6 significantly decreased with decreasing stressing rates in ambient air at 1370°C. Fractography showed that an SCC damage zone had formed in the fracture plane on all tested specimens. It was evident that oxidation, and not creep damage, ultimately initiated the formation of an SCC damage zone in PY6 which significantly weakened it. Creep damage was observed on those specimens tested at stressing rates slower than 10^{-1} MPa/s and appeared to exacerbate the already deleterious effects of the stress-oxidation damage zone.

The flexure strength of this PY6 exhibited stressing rate independence at 1370°C in argon and nitrogen atmospheres. Specimens contained evidence of creep damage (i.e., cavitation) at stressing rates slower than 10^{-1} MPa/s. No SCC damage zone was observed for any of the specimens tested in either of these two environments.

Flexural dynamic fatigue results suggested that manufacturers or end users of silicon nitride components can greatly reduce the deleterious effects which stem from the formation of SCC by appropriately suppressing oxidation in ambient air.

5. REFERENCES

1. A. E. Pasto and S. Natansohn, *Development of Improved Processing Methods for High Reliability Structural Ceramics for Advanced Heat Engines*, ORNL/Sub/89-SD548/1, Martin Marietta Energy Systems, Inc., Oak Ridge Natl. Lab., July 1992.

2. A. A. Wereszczak, T. P. Kirkland, K. Breder, M. K. Ferber, and P. Khandelwal, "High Temperature Dynamic Fatigue Performance of a Hot Isostatically Pressed Silicon Nitride," *Mater. Sci. Eng.* **A191**, 257-66 (1995).

3. M. K. Ferber and M. G. Jenkins, "Evaluation of the Strength and Creep-Fatigue Behavior of a HIPed Silicon Nitride," *J. Am. Ceram. Soc.* **75** (9), 2453-62 (1992).

4. N. L. Hecht, *Environmental Effects in Toughened Ceramics-Final Report*, UDR-TR-91-15, University of Dayton Research Institute, Dayton, Ohio, February 1991.

5. H. Riedel, *Fracture at High Temperatures*, Springer-Verlag, Berlin, Heidelburg, 1987.

6. W. R. Cannon and T. G. Langdon, "REVIEW: Creep of Ceramics, Part 1, Mechanical Characteristics," *J. Mater. Sci.* **18**, 1-50 (1983).

7. G. D. Quinn, "Static Fatigue Resistance of Hot Pressed Silicon Nitride," pp. 319-32 in *Fracture Mechanics of Ceramics*, Vol. 8, ed. R. C. Bradt, A. G. Evans, D. P. H. Hasselmann, and F. F. Lange, Plenum Press, New York, 1989.

8. M. K. Ferber and M. G. Jenkins, "Rotor Data Base Generation," pp. 340-61 in *Ceramic Technology for Advanced Heat Engines Project Semiannual Progress Report for October 1990 Through March 1991*, ORNL/TM-11859, Martin Marietta Energy Systems, Inc., Oak Ridge Natl. Lab., July 1991.

9. D. C. Cranmer, B. J. Hockey, S. M. Wiederhorn, and R. Yeckley, "Creep and Creep-Rupture of HIPed Si_3N_4," *Ceram. Eng. Sci. Proc.* **12**, 1862-72 (1991).

10. F. C. Monkman and N. J. Grant, "An Empirical Relationship between Rupture Life and Minimum Creep Rate in Creep-Rupture Tests," *Proc. ASTM* **56**, 593-620 (1956).

11. F. F. Lange, "Non-Elastic Deformation of Polycrystals with a Liquid Phase," pp. 361-81 in *Deformation of Ceramic Materials*, ed. R. C. Bradt and R. E. Tressler, Plenum Press, New York, 1975.

12. J. E. Marion, A. G. Evans, and M. D. Drory, "High Temperature Failure Initiation in Liquid Phase Sintered Materials," *Acta Metall.* **31**, 1445-57 (1983).

13. S. S. Suresh and J. R. Brockenbrough, "A Theory for Creep by Interfacial Flaw Growth in Ceramics and Ceramic Composites," *Acta Metall. Mater.* **38**(1), 55-68 (1990).

14. R. Raj and P. E. D. Morgan, "Activation Energies for Densification, Creep, and Grain-Boundary Sliding in Nitrogen Ceramics," *J. Am. Ceram. Soc.* **64**(10), C143-C145 (1981).

15. J. A. Todd and Zhi-Yue Xu, "The High-Temperature Creep Deformation of Si_3N_4-$6Y_2O_3$-$2Al_2O_3$," *J. Mater. Sci.* **27**, 4443-52 (1989).

16. K. L. Luthra, "Some Perspectives on Oxidation of Silicon Carbide and Silicon Nitride," *J. Am. Ceram. Soc.* **74**(5), 1095-103 (1991).

17. R. K. Govila, "Uniaxial Tensile and Flexural Stress Rupture Strength of Hot-Pressed Si_3N_4," *J. Am. Ceram. Soc.* **65**(1), 15-21 (1982).

18. B. J. Dalgleish, E. B. Slamovich, and A. G. Evans, "Duality in the Creep Rupture of a Polycrystalline Alumina," *J. Am. Ceram. Soc.* **68**(11), 575-81 (1985).

19. G. E. Dieter, *Mechanical Metallurgy*, 3rd ed., McGraw-Hill, Inc., New York, 1986.

20. M. N. Menon, H. T. Fang, D. C. Wu, M. G. Jenkins, and M. K. Ferber, "Creep and Stress Rupture Behavior of an Advanced Silicon Nitride: Part II, Creep Rate Behavior," *J. Am. Ceram. Soc.* **77**(5), 1228-34 (1994).

21. A. A. Wereszczak, T. P. Kirkland, and M. K. Ferber, "Stress and Strain Relaxation Behaviour in HIPed Silicon Nitrides," *J. Mater. Sci. Lett.* **13**, 1469-71 (1994).

22. F. F. Lange, D. R. Clarke, and B. I. Davis, "Compressive Creep of Si_3N_4/MgO Alloys, Part 2, Source of Viscoelastic Effect," *J. Mater. Sci.* **15**, 611-15 (1980).

23. R. M. Arons and J. K. Tien, "Creep and Strain Recovery in Hot-Pressed Silicon Nitride," *J. Mater. Sci.* **15**, 2046-58 (1980).

24. E. W. Hart, "A Phenomenological Theory for Plastic Deformation of Polycrystalline Metals," *Acta Metall.* **18**, 599-610 (1970).

25. D. A. Woodford, D. R. VanSteele, and M. J. Hyder, "Tensile Stress Relaxation of Alumina at High Temperatures," *J. Am. Ceram. Soc.* **74**(12), 3142-44 (1991).

26. S. M. Wiederhorn, "Subcritical Crack Growth in Ceramics," pp. 623-46 in *Fracture Mechanics of Ceramics*, Vol. 2, ed. R. C. Bradt, D. P. H. Hasselman, and F. F. Lange, Plenum Press, New York, 1974.

27. J. E. Ritter, "Engineering Design and Fatigue Failure of Brittle Materials. pp. 667-86 in *Fracture Mechanics of Ceramics*, Vol. 4, ed. R. C. Bradt, D. P. H. Hasselman, and F. F. Lange. Plenum Press, New York, 1978.

28. T. Fett and D. Munz, "Determination of Crack Growth Parameter N in Ceramics Under Creep Conditions," *J. Test. Eval.* **3**, 143-51 (1985).

29. C.-K. J. Lin, M. G. Jenkins, and M. K. Ferber, "Tensile Dynamic and Static Fatigue Relations for a HIPed Silicon Nitride at Elevated Temperatures," *J. Euro. Ceram. Soc.* **12**, 3-13 (1993).

30. A. Venkateswaran, K. Y. Donaldson, and D. P. H. Hasselman, "Role of Intergranular Damage-Induced Decrease in Young's Modulus in the Nonlinear Deformation and Fracture of an Alumina at Elevated Temperatures," *J. Am. Ceram. Soc.* **71**, 565-76 (1988).

31. C.-K. J. Lin, M. G. Jenkins, and M. K. Ferber, "Cyclic Fatigue of Hot Isostatically Pressed Silicon Nitride at Elevated Temperatures," *J. Mater. Sci.* **29**, 3517-26 (1994).

32. C.-K. J. Lin, D. F. Socie, Y. Xu, and A. Zangvil, "Static and Cyclic Fatigue of Alumina at High Temperatures: II, Failure Analysis," *J. Am. Ceram. Soc.* **75**, 637-48 (1992).

33. Y-H. Pao and J. Marin, "An Analytical Theory of the Creep Deformation of Materials," *J. Appl. Mech.* **6**, 245-52 (1953).

34. E. N. da C. Andrade, "The Viscous Flow in Metals and Allied Phenomena," *Proc. R. Soc. London* **A90**, 329 (1914).

35. H. Kraus, *Creep Analysis*, John Wiley & Sons, New York, 1980.

36. J. D. Lubahn, "The Role of Anelasticity in Creep, Tension, and Relaxation Behavior," *Trans. Am. Soc. Met.* **45**, 787-838 (1953).

37. W. Luecke, S. M. Wiederhorn, B. J. Hockey, and G. G. Long, "Cavity Evolution During Tensile Creep of Si_3N_4," pp 455-60 in *Silicon Nitride Ceramics–Scientific and Technological Advances*, Vol. 287, ed. I-W. Chen, P. F. Becher, M. Mitomo, G. Petzow, and T-S. Yen, Materials Research Society, Pittsburgh, 1993.

38. A. A. Wereszczak, M. K. Ferber, T. P. Kirkland, and C.-K. J. Lin, "Effect of Cyclic Loading on the Creep Performance of Silicon Nitride," to be published in ASME Turbo Expo '95 Proceedings, Houston, Texas, June 1995.

39. G. W. Hollenberg, G. R. Terwilliger, and R. S. Gordon, "Calculation of Stresses and Strains in Four-Point Bending Creep Tests," *J. Am. Ceram. Soc.* **54**(4), 196-99 (1971).

40. A. A. Wereszczak, K. Breder, and M. K. Ferber, "Role of Oxidation in Time-Dependent Failure Behavior of HIPed Silicon Nitride at 1370°C," *J. Am. Ceram. Soc.* **76**(11), 2919-22 (1993).

6. PUBLICATIONS STEMMING FROM THIS WORK

1. M. G. Jenkins and M. K. Ferber, "Determination of High-Temperature Creep Parameters in Structural Ceramics from Constant-Displacement, Stress-Relaxation Tests," pp. 94-101 in *Proceedings of the 1991 SEM Spring Conference on Experimental Mechanics, Milwaukee, Wisconsin June 9-13, 1991,* Society for Experimental Mechanics, Bethel, Conn., 1991.
2. M. G. Jenkins and M. K. Ferber, "Stress-Relaxation Tests Used to Determine the Elevated-Temperature Creep Parameters of Structural Ceramics," pp. 539-53 in *Fracture Mechanics of Ceramics,* Vol. 10, ed. R. C. Bradt, D. P. H. Hasselman, and F. F. Lange, Plenum Press, New York, 1992.
3. M. K. Ferber and M. G. Jenkins, "Evaluation of the Strength and Creep-Fatigue Behavior of a HIPed Silicon Nitride," *J. Am. Ceram. Soc.* **75**(9), 2453-62 (1992).
4. M. K. Ferber and M. G. Jenkins, "Evaluation of the High-Temperature Mechanical Reliability of a HIPed Silicon Nitride," pp. 281-91 in *Proceedings of the Annual Automotive Technology Development Contractors' Meeting, P-256, Dearborn, Michigan, October 28-31, 1991,* Society of Automotive Engineers, Warrendale, Pa., 1992.
5. M. K. Ferber and M. G. Jenkins, "Empirical Evaluation of Tensile Creep and Creep Rupture in a HIPed Silicon Nitride," pp. 81-90 in *Creep: Characterization, Damage and Life Assessment*, ed. D. A. Woodford, C. H. A. Townley, and M. Ohhnami, ASM International, Materials Park, Ohio, 1992.

6. M. G. Jenkins, M. K. Ferber, and J. A. Salem, "Creep and Slow Crack Growth Mechanisms Related to Macroscopic Creep Behaviour of a Silicon Nitride Ceramic at Elevated Temperatures," pp. 1566-74 in *Proceedings of the 1992 SEM Spring Conference on Experimental Mechanics, Las Vegas, Nevada, June 8-11, 1992,* Society of Experimental Mechanics, Bethel, Conn., 1992.

7. C.-K. J. Lin, M. G. Jenkins, and M. K. Ferber, "Tensile Dynamic and Static Fatigue Relations for a HIPed Silicon Nitride at Elevated Temperatures," *J. Euro. Ceram. Soc.* **12**, 3-13 (1993).

8. C.-K. J. Lin, M. G. Jenkins, and M. K. Ferber, "Evaluation of Tensile Static, Dynamic, and Cyclic Fatigue Behavior for a HIPed Silicon Nitride at Elevated Temperatures," pp. 455-60 in *Silicon Nitride Ceramics–Scientific and Technological Advances*, Vol. 287, ed. I-W. Chen, P. F. Becher, M. Mitomo, G. Petzow, and T.-S. Yen, Materials Research Society, Pittsburgh, 1993.

9. M. G. Jenkins, M. K. Ferber, and C.-K. J. Lin, "Apparent Enhanced Fatigue Behavior Under Cyclic Tensile Loading for a HIPed Silicon Nitride," *J. Am. Ceram. Soc.* **76**(3), 788-92 (1993).

10. A. A. Wereszczak, K. Breder, M. K. Ferber, T. P. Kirkland, and P. Khandelwal, "Environmental Effects on the Flexure Strength of HIPed Silicon Nitride at Elevated Temperatures," pp. 686-87 in *Extended Abstracts, Vol. 93-2, Fall Meeting of the Electrochemical Society*, Electrochemical Society, Pennington, N.J., 1993.

11. A. A. Wereszczak, K. Breder, and M. K. Ferber, "Role of Oxidation in Time-Dependent Failure Behavior of HIPed Silicon Nitride at 1370°C," *J. Am. Ceram. Soc.* **76**(11), 2919-22 (1993).

12. A. A. Wereszczak, M. K. Ferber, and T. P. Kirkland, "Effects of Oxidation and Creep Damage Mechanisms on Creep Behavior in HIPed Silicon Nitrides," *Ceram. Eng. Sci. Proc.* **15**, 49-56 (1994).

13. C.-K. J. Lin, M. G. Jenkins, and M. K. Ferber, "Cyclic Fatigue of Hot Isostatically Pressed Silicon Nitride at Elevated Temperatures," *J. Mater. Sci.* **29**, 3517-26 (1994).

14. A. A. Wereszczak, T. P. Kirkland, and M. K. Ferber, "Stress and Strain Relaxation Behaviour in HIPed Silicon Nitrides," *J. Mater. Sci. Lett.* **13**, 1469-71 (1994).

15. A. A. Wereszczak, M. K. Ferber, T. P. Kirkland, and C.-K. J. Lin, "Effect of Cyclic Loading on the Creep Performance of Silicon Nitride," to be published in ASME Turbo Expo '95 Proceedings, Houston, Texas, June 1995.

INTERNAL DISTRIBUTION

Central Research Library
Document Reference Section
Laboratory Records Department
Laboratory Records, ORNL-RC
ORNL Patent Office
M&C Records Office
R. L. Beatty
P. F. Becher
K. Breder (5)
C.R. Brinkman
S. C. Deevi
M. K. Ferber (5)
C. Huseh
M. G. Jenkins (5)
J. O. Kiggans, Jr.
O. F. Kimball
T. P.Kirkland (5)
D. R. Johnson
H. Lin
C.-K. J. Lin (5)
T. A. Nolan
A. E. Pasto
J. H. Schneibel
L. L. Snead
J. P. Strizak
T. N. Tiegs
A. A. Wereszczak (5)
C. G. Westmoreland
D. F. Wilson
I. G. Wright
S. J. Zinkle
H. W. Foglesong (Consultant)
E. L. Menger (Consultant)
J. G. Simon (Consultant)
E. K. Spear (Consultant)

EXTERNAL DISTRIBUTION

James H. Adair
University of Florida
Materials Science and Engineering
317 MAE Bldg.
Gainesville, FL 32611-2066

Donald F. Adams
University of Wyoming
Mechanical Engineering Department
P.O. Box 3295
Laramie, WY 82071

Ilhan A. Aksay
Princeton University
A313 Engineering Quadrangle
Princeton, NJ 08544-5263

Joseph E. Amaral
Instron Corporation
Corporate Engineering Office
100 Royale Street
Canton, MA 02021

Edward M. Anderson
Aluminum Company of America
N. American Industrial Chemical
P.O. Box 300
Bauxite, AR 72011

Frank Armatis
3M Company
Building 60-1N-01
St. Paul, MN 55144-1000

Everett B. Arnold
Detroit Diesel Corporation
Mechanical Systems Technology
13400 Outer Drive West
Detroit, MI 48239-4001

Dennis Assanis
University of Michigan
Dept. of Mechanical Engineering
321 W. E. Lay, N.C.
Ann Arbor, MI 48109

V. S. Avva
North Carolina A&T State Univ.
Dept. of Mechanical Engineering
Greensboro, NC 27411

Bob Baker
Ceradyne, Inc.
3169 Redhill Avenue
Costa Mesa, CA 92626

Frank Baker
Aluminum Company of America
Alcoa Technical Center
Alcoa Center, PA 15069

Clifford P. Ballard
AlliedSignal Aerospace Company
Ceramics Program
P.O. Box 1021
Morristown, NJ 07962-1021

Donald F. Baxter, Jr.
ASM International
Advanced Materials & Processes
Materials Park, OH 44073-0002

M. Brad Beardsley
Caterpillar, Inc.
Technical Center Bldg. E
P.O. Box 1875
Peoria, IL 61656-1875

Tom Bernecki
Northwestern University
1801 Maple Avenue
Evanston, IL 60201-3135

Ram Bhatt
NASA Lewis Research Center
21000 Brookpark Road
Cleveland, OH 44135

Deane I. Biehler
Caterpillar, Inc.
Engineering Research Materials
P.O. Box 1875, Bldg. E
Peoria, IL 61656-1875

Keith A. Blakely
Advanced Refractory Technologies, Inc.
699 Hertel Avenue
Buffalo, NY 14207

Bruce Boardman
Deere and Company Technical Ctr.
3300 River Drive
Moline, IL 61265

Tom Booth
AlliedSignal, Inc.
AiResearch Los Angeles Division
2525 West 190th Street
Torrance, CA 90509-2960

J.A.M. Boulet
University of Tennessee
Engineering Science and Mechanics
Knoxville, TN 37996-2030

Michael C. Brands
Cummins Engine Company, Inc.
P.O. Box 3005, Mail Code 50179
Columbus, IN 47201-3005

Raymond J. Bratton
Westinghouse Science & Technology
1310 Beulah Road
Pittsburgh, PA 15235

John J. Brennan
United Technologies Corporation
Silver Lane, MS:24
East Hartford, CT 06108

Sherman D. Brown
University of Illinois
Materials Science and Engineering
105 South Goodwin Avenue
Urbana, IL 61801

S. L. Bruner
Ceramatec, Inc.
2425 South 900 West
Salt Lake City, UT 84119

Bill Bustamante
AMERCOM, Inc.
8928 Fullbright Avenue
Chatsworth, CA 91311

Oral Buyukozturk
Massachusetts Institute of Technology
77 Massachusetts Ave., Room 1-280
Cambridge, MA 02139

David A. Caillet
Ethyl Corporation
451 Florida Street
Baton Rouge, LA 70801

David Carruthers
Kyocera Industrial Ceramics Company
P.O. Box 2279
Vancouver, WA 98668-2279

Ronald H. Chand
Chand Kare Technical Ceramics
2 Coppage Drive
Worcester, MA 01603-1252

Robert E. Chaney
EG&G Idaho, Inc.
Idaho National Engineering Lab.
P.O. Box 1625
Idaho Falls, ID 83415-3525

Nam S. Chang
Chrysler Corporation
12000 Chrysler Drive
Highland Park, MI 48288-0001

Frank Childs
EG&G Idaho, Inc.
Idaho National Engineering Lab.
P.O. Box 1625
Idaho Falls, ID 83415-3527

William J. Chmura
Torrington Company
59 Field Street
Torrington, CT 06790-4942

Tsu-Wei Chou
University of Delaware
201 Spencer Laboratory
Newark, DE 19716

Joel P. Clark
Massachusetts Institute of Technology
Room 8-409
Cambridge, MA 02139

William C. Connors
Sundstrand Aviation Operations
Materials Science & Engineering
4747 Harrison Avenue
Rockford, IL 61125-7002

John A. Coppola
Carborundum Company
Niagara Falls R&D Center
P.O. Box 832
Niagara Falls, NY 14302

Normand D. Corbin
Norton Company
SGNICC/NRDC
Goddard Road
Northboro, MA 01532-1545

Douglas Corey
AlliedSignal, Inc.
2525 West 190th Street, MS:T52
Torrance, CA 90504-6099

Keith P. Costello
Chand/Kare Technical Ceramics
2 Coppage Drive
Worcester, MA 01603-1252

Ed. L. Courtright
Pacific Northwest Laboratory
MS:K3-59
Richland, WA 99352

Art Cozens
Instron Corporation
3414 Snowden Avenue
Long Beach, CA 90808

M. J. Cronin
Mechanical Technology, Inc.
968 Albany-Shaker Road
Latham, NY 12110

Gary M. Crosbie
Ford Motor Company
20000 Rotunda Drive
MD-2313, SRL Building
Dearborn, MI 48121-2053

John Cuccio
AlliedSignal Engines
P.O. Box 52180, MS:1302-2Q
Phoenix, AZ 85072-2180

Raymond A. Cutler
Ceramatec, Inc.
2425 South 900 West
Salt Lake City, UT 84119

Stephen C. Danforth
Rutgers University
P.O. Box 909
Piscataway, NJ 08855-0909

Frank Davis
AlliedSignal Aerospace Company
7550 Lucerne Drive, #203
Middleburg Heights, OH 44130

Robert F. Davis
North Carolina State University
Materials Engineering Department
P.O. Box 7907
Raleigh, NC 27695

George C. DeBell
Ford Motor Company
Scientific Research Lab
P.O. Box 2053, Room S2023
Dearborn, MI 48121-2053

Gerald L. DePoorter
Colorado School of Mines
Metallurgical & Materials Engrg.
Golden, CO 80401

L. R. Dharani
University of Missouri-Rolla
224 M.E.
Rolla, MO 65401

Kenneth C. Dreitlein
United Technologies Research Ctr.
Silver Lane
East Hartford, CT 06108

Robin A.L. Drew
McGill University
3450 University Street
Montreal Quebec H3A 2A7
CANADA

Ernest J. Duwell
3M Abrasive Systems Division
3M Center
St. Paul, MN 55144-1000

Robert J. Eagan
Sandia National Laboratories
Engineered Materials & Processes
P.O. Box 5800
Albuquerque, NM 87185-5800

Jeffrey Eagleson
Lanxide Corporation
1001 Connecticut Avenue, N.W.
Washington, DC 20036

Harry E. Eaton
United Technologies Corporation
Silver Lane
East Hartford, CT 06108

Harvill C. Eaton
Louisiana State University
240 Thomas Boyd Hall
Baton Rouge, LA 70803

Christopher A. Ebel
Carborundum Company
Technology Division
P.O. Box 832
Niagara Falls, NY 14302-0832

J. J. Eberhardt
U.S. Department of Energy
Office of Transportation Matls.
EE-34, Forrestal Building
Washington, DC 20585

Jim Elder
Eaton Corporation
26201 Northwestern Highway
P.O. Box 766
Southfield, MI 48037

G. A. Eisman
Dow Chemical Company
Ceramics and Advanced Materials
52 Building
Midland, MI 48667

Jeff Epstein
Ceramic Technologies, Inc.
12739 Ashford Knoll
Houston, TX 77082

Kenneth A. Epstein
Dow Chemical Company
2030 Building
Midland, MI 48674

Art Erdemir
Argonne National Laboratory
9700 S. Cass Avenue
Argonne, IL 60439

John N. Eustis
U.S. Deparment of Energy
Industrial Energy Efficiency Div.
EE-221, Forrestal Building
Washington, DC 20585

W. L. Everitt
Kyocera International, Inc.
8611 Balboa Avenue
San Diego, CA 92123

John W. Fairbanks
U.S. Department of Energy
Offie of Propulsion Systems
EE-322, Forrestal Building
Washington, DC 20585

Tim Fawcett
Dow Chemical Company
Advanced Ceramics Laboratory
1776 Building
Midland, MI 48674

Robert W. Fawley
Sundstrand Power Systems
Div. of Sundstrand Corporation
P.O. Box 85757
San Diego, CA 92186-5757

Larry Ferrell
Babcock & Wilcox
Old Forest Road
Lynchburg, VA 24505

Thomas F. Foltz
Textron Specialty Materials
2 Industrial Avenue
Lowell, MA 01851

Edwin Frame
Southwest Research Institute
P.O. Drawer 28510
San Antonio, TX 78284

Marc R. Freedman
NASA Lewis Research Center
21000 Brookpark Road, MS:49-3
Cleveland, OH 44135

Brian R.T. Frost
Argonne National Laboratory
9700 S. Cass Avenue, Bldg. 900
Argonne, IL 60439

Lawrence R. Frost
Instron Corporation
100 Royall Street
Canton, MA 02021

J. P. Gallagher
University of Dayton Research Institute
300 College Park, JPC-250
Dayton, OH 45469-0120

John Ghinazzi
Coors Technical Ceramics Company
1100 Commerce Park Drive
Oak Ridge, TN 37830

Robert Giddings
General Electric Company
P.O. Box 8
Schenectady, NY 12301

G. A. Graves
University of Dayton Research Institute
300 College Park
Dayton, OH 45469-0001

Robert E. Green, Jr.
Johns Hopkins University
Materials Science and Engineering
Baltimore, MD 21218

Lance Groseclose
Allison Engine Company
P.O. Box 420, MS:W-5
Indianapolis, IN 46206

Thomas J. Gross
U.S. Department of Energy
Office of Transportation Technologies
EE-30, Forrestal Building
Washington, DC 20585

John P. Gyekenyesi
NASA Lewis Research Center
21000 Brookpark Road, MS:6-1
Cleveland, OH 44135

Nabil S. Hakim
Detroit Diesel Corporation
13400 Outer Drive West
Detroit, MI 48239

Philip J. Haley
Allison Engine Company
P.O. Box 420, MS:T12A
Indianapolis, IN 46236

Judith Hall
Fiber Materials, Inc.
Biddeford Industrial Park
5 Morin Street
Biddeford, ME 04005

Y. Hamano
Kyocera Industrial Ceramics Corp.
5713 E. Fourth Plain Blvd.
Vancouver, WA 98661-6857

Norman H. Harris
Hughes Aircraft Company
P.O. Box 800520
Saugas, CA 91380-0520

Alan M. Hart
Dow Chemical Company
1776 Building
Midland, MI 48674

Pat E. Hart
Battelle Pacific Northwest Lab.
Ceramics and Polymers Development
P.O. Box 999
Richland, WA 99352

Michael H. Haselkorn
Caterpillar Inc.
Technical Center, Building E
P.O. Box 1875
Peoria, IL 61656-1875

Debbie Haught
U.S. Department of Energy
Office of Transportation Materials
EE-34, Forrestal Building
Washington, DC 20585

N. B. Havewala
Corning, Inc.
SP-PR-11
Corning, NY 14831

Norman L. Hecht
University of Dayton Research Institute
300 College Park
Dayton, OH 45469-0172

Peter W. Heitman
Allison Engine Company
P.O. Box 420, MS:W-5
Indianapolis, IN 46206-0420

Thomas P. Herbell
NASA Lewis Research Center
21000 Brookpark Road, MS:49-3
Cleveland, OH 44135

Marlene Heroux
Rolls-Royce, Inc.
2849 Paces Ferry Road, Suite 450
Atlanta, GA 30339-3769

Hendrik Heystek
Bureau of Mines
Tuscaloosa Research Center
P.O. Box L
University, AL 35486

Robert V. Hillery
GE Aircraft Engines
One Neumann Way, M.D. H85
Cincinnati, OH 45215

Arthur Hindman
Instron Corporation
100 Royall Street
Canton, MA 02021

Tommy Hiraoka
NGK Locke, Inc.
1000 Town Center
Southfield, MI 48075

Fu H. Ho
General Atomics
P.O. Box 85608
San Diego, CA 92186-9784

Clarence Hoenig
Lawrence Livermore National Lab.
P.O. Box 808, Mail Code L-369
Livermore, CA 94550

Thomas Hollstein
Fraunhofer-Institute fur
Werkstoffmechanik
Wohlerstrasse 11
D-79108 Freiburg
GERMANY

Richard Holt
National Research Council Canada
Structures and Materials Lab
Ottawa Ontario K1A OR6
CANADA

Woodie Howe
Coors Technical Ceramics Company
1100 Commerce Park Drive
Oak Ridge, TN 37830

Harold A. Huckins
Princeton Advanced Technology
4 Bertram Place
Hilton Head, SC 29928

Michael S. Inoue
Kyocera International, Inc.
8611 Balboa Avenue
San Diego, CA 92123-1580

Said Jahanmir
NIST
Materials Bldg., Room A-237
Gaithersburg, MD 20899

Curtis A. Johnson
General Electric Company
P.O. Box 8
Schenectady, NY 12301

Sylvia Johnson
SRI International
333 Ravenswood Avenue
Menlo Park, CA 94025

Thomas A. Johnson
Lanxide Corporation
P.O. Box 6077
Newark, DE 19714-6077

W. S. Johnson
Indiana University
One City Centre, Suite 200
Bloomington, IN 47405

Tom Kalamasz
Norton/TRW Ceramics
7A-4 Raymond Avenue
Salem, NH 03079

Nick Kamiya
Kyocera Industrial Ceramics Corp.
25 Northwest Point Blvd., #450
Elk Grove Village, IL 60007

Keith R. Karasek
AlliedSignal Aerospace Company
50 E. Algonquin Road
Des Plaines, IL 60017-5016

Martha R. Kass
U.S. Department of Energy
Oak Ridge Operations
Building 4500N, MS 6269
Oak Ridge, TN 37831-6269

Robert E. Kassel
Ceradyne, Inc.
3169 Redhill Avenue
Costa Mesa, CA 92626

Allan Katz
Wright Laboratory
Metals and Ceramics Division
Wright-Patterson AFB, OH 45433

R. Nathan Katz
Worcester Polytechnic Institute
100 Institute Road
Worcester, MA 01609

Frederick L. Kennard, III
AC Rochester
1300 N. Dort Highway
Flint, MI 48556

Thomas Ketcham
Corning, Inc.
SP-DV-1-9
Corning, NY 14831

Pramod K. Khandelwal
Allison Engine Company
P.O. Box 420, MS:T10B
Indianapolis, IN 46206

Jim R. Kidwell
AlliedSignal Engines
P.O. Box 52180
Phoenix, AZ 85072-2180

W. C. King
Mack Truck, Z-41
1999 Pennsylvania Avenue
Hagerstown, MD 21740

Tony Kirn
Caterpillar, Inc.
Defense Products Department, JB7
Peoria, IL 61629

James D. Kiser
NASA Lewis Research Center
21000 Brookpark Road, MS:49-3
Cleveland, OH 44135

Stanley J. Klima
NASA Lewis Research Center
21000 Brookpark Road, MS:6-1
Cleveland, OH 44135

Albert S. Kobayashi
University of Washington
Mechanical Engineering Department
Mail Stop:FU10
Seattle, WA 98195

Joseph A. Kovach
Eaton Corporation
32500 Chardon Road
Willoughby Hills, OH 44094

Waltraud M. Kriven
University of Illinois
105 S. Goodwin Avenue
Urbana, IL 61801

Dave Kupperman
Argonne National Laboratory
9700 S. Cass Avenue
Argonne, IL 60439

Hari S. Lamba
General Motors Corporation
9301 West 55th Street
LaGrange, IL 60525

James Lankford
Southwest Research Institute
6220 Culebra Road
San Antonio, TX 78228-0510

S. K. Lau
Carborundum Company
Technology Division
P.O. Box 832, B-100
Niagara Falls, NY 14302

J. Lawrence Lauderdale
Babcock & Wilcox
1850 "K" Street, Suite 950
Washington, DC 20006

Jean F. LeCostaouec
Textron Specialty Materials
2 Industrial Avenue
Lowell, MA 01851

Burtrand I. Lee
Clemson University
Olin Hall
Clemson, SC 29634-0907

Stan Levine
NASA Lewis Research Center
21000 Brookpark Road, MS:49-3
Cleveland, OH 44135

David Lewis, III
Naval Research Laboratory
Code 6370
Washington, DC 20375-5343

Robert H. Licht
Norton Company
SGNICC/NRDC
Goddard Road
Northboro, MA 01532-1545

E. Lilley
Norton Company
SGNICC/NRDC
Goddard Road
Northboro, MA 01532-1545

Laura J. Lindberg
AlliedSignal Aerospace Company
Garrett Fluid Systems Division
P.O. Box 22200
Tempe, AZ 85284-2200

Bill Long
Babcock & Wilcox
P.O. Box 11165
Lynchburg, VA 24506

L. A. Lott
EG&G Idaho, Inc.
Idaho National Engineering Lab.
P.O. Box 1625
Idaho Falls, ID 83415-2209

James W. MacBeth
Carborundum Company
Structural Ceramics Division
P.O. Box 1054
Niagara Falls, NY 14302

George Maczura
Aluminum Company of America
3450 Park Lane Drive
Pittsburgh, PA 15275-1119

Tai-il Mah
Universal Energy Systems, Inc.
4401 Dayton-Xenia Road
Dayton, OH 45432

John Mangels
Ceradyne, Inc.
3169 Redhill Avenue
Cosa Mesa, CA 92626

William R. Manning
Champion Aviation Products Div.
P.O. Box 686
Liberty, SC 29657

Ken Marnoch
Amercom, Inc.
8928 Fullbright Avenue
Chatsworth, CA 91311

Robert A. Marra
Aluminum Company of America
Alcoa Technical Center
Alcoa Center, PA 15069

Steve C. Martin
Advanced Refractory Technologies
699 Hertel Avenue
Buffalo, NY 14207

James P. Mathers
3M Company
3M Center, Bldg. 201-3N-06
St. Paul, MN 55144

F. N. Mazadarany
General Electric Company
Bldg. K-1, Room MB-159
P.O. Box 8
Schnedtady, NY 12301

James W. McCauley
Alfred University
Binns-Merrill Hall
Alfred, NY 14802

B. J. McEntire
Norton Company
10 Airport Park Road
East Granby, CT 06026

Thomas D. McGee
Iowa State University
110 Engineering Annex
Ames, IA 50011

Carol McGill
Corning, Inc.
Sullivan Park, FR-02-08
Corning, NY 14831

James McLaughlin
Sunstrand Power Systems
4400 Ruffin Road
P.O. Box 85757
San Diego, CA 92186-5757

J. C. McVickers
AlliedSignal Engines
P.O. Box 52180, MS:9317-2
Phoenix, AZ 85072-2180

Michael D. Meiser
AlliedSignal, Inc.
Ceramic Components
P.O. Box 2960, MS:T21
Torrance, CA 90509-2960

Ken Michaels
Chrysler Motors Corporation
P.O. Box 1118, CIMS:418-17-09
Detroit, MI 48288

Carl E. Miller
AC Rochester
1300 N. Dort Highway, MS:32-31
Flint, MI 48556

Michele V. Mitchell
AlliedSignal, Inc.
Ceramic Components
P.O. Box 2960, MS:T21
Torrance, CA 90509-2960

Howard Mizuhara
WESGO
477 Harbor Boulevard
Belmont, CA 94002

Helen Moeller
Babcock & Wilcox
P.O. Box 11165
Lynchburg, VA 24506-1165

Francois R. Mollard
Concurrent Technologies Corp.
1450 Scalp Avenue
Johnstown, PA 15904-3374

Geoffrey P. Morris
3M Company
3M Traffic Control Materials
Bldg. 209-BW-10, 3M Center
St. Paul, MN 55144-1000

Jay A. Morrison
Rolls-Royce, Inc.
2849 Paces Ferry Road, Suite 450
Atlanta, GA 30339-3769

Joel P. Moskowitz
Ceradyne, Inc.
3169 Redhill Avenue
Costa Mesa, CA 92626

Brij Moudgil
University of Florida
Materials Science & Engineering
Gainesville, FL 32611

Theresa A. Mursick-Meyer
Norton Company
SGNICC/NRDC
Goddard Road
Northboro, MA 01532-1545

Malcolm Naylor
Cummins Engine Company, Inc.
P.O. Box 3005, Mail Code 50183
Columbus, IN 47202-3005

Fred A. Nichols
Argonne National Laboratory
9700 S. Cass Avenue
Argonne, IL 60439

H. Nickel
Forschungszentrum Juelich (KFA)
Postfach 1913
D-52425 Juelich
GERMANY

Dale E. Niesz
Rutgers University
Center for Ceramic Research
P.O. Box 909
Piscataway, NJ 08855-0909

Paul W. Niskanen
Lanxide Corporation
P.O. Box 6077
Newark, DE 19714-6077

David M. Nissley
United Technologies Corporation
Pratt & Whitney Aircraft
400 Main Street, MS:163-10
East Hartford, CT 06108

Robert Orenstein
General Electric Company
55-112, River Road
Schenectady, NY 12345

Pellegrino Papa
Corning, Inc.
MP-WX-02-1
Corning, NY 14831

E. Beth Pardue
MPC
8297 Williams Ferry Road
Lenoir City, TN 37771

Soon C. Park
3M Company
Building 142-4N-02
P.O. Box 2963
St. Paul, MN 55144

Vijay M. Parthasarathy
Caterpillar/Solar Turbines
2200 Pacific Highway
P.O. Box 85376
San Diego, CA 92186-5376

James W. Patten
Cummins Engine Company, Inc.
P.O. Box 3005, Mail Code 50183
Columbus, IN 47202-3005

Robert W. Pepper
Textron Specialty Materials
2 Industrial Avenue
Lowell, MA 01851

Peter Perdue
Detroit Diesel Corporation
13400 Outer Drive West
Speed Code L-04
Detroit, MI 48239-4001

John J. Petrovic
Los Alamos National Laboratory
Group MST-4, MS:G771
Los Alamos, NM 87545

Bruce J. Pletka
Michigan Technological University
Metallurgical & Materials Engrg.
Houghton, MI 49931

John P. Pollinger
AlliedSignal, Inc.
Ceramic Components
P.O. Box 2960, MS:T21
Torrance, CA 90509-2960

Bob R. Powell
General Motors Corporation
Metallurgy Department
Box 9055
Warren, MI 48090-9055

Karl M. Prewo
United Technologies Research Ctr.
411 Silver Lane, MS:24
East Hartford, CT 06108

George Quinn
NIST
Ceramics Division, Bldg. 223
Gaithersburg, MD 20899

Ramas V. Raman
Ceracon, Inc.
1101 N. Market Boulevard, Suite 9
Sacramento, CA 95834

Charles F. Rapp
Owens Corning Fiberglass
2790 Columbus Road
Granville, OH 43023-1200

Dennis W. Readey
Colorado School of Mines
Metallurgy and Materials Engr.
Golden, CO 80401

K. L. Reifsnider
VPI & SU
Engineering Science and Mechanics
Blacksburg, VA 24061

Paul E. Rempes
McDonnel Douglas Aircraft Co.
P.O. Box 516, Mail Code:0642263
St. Louis, MO 63166-0516

Gopal S. Revankar
John Deere Company
3300 River Drive
Moline, IL 61265

David W. Richerson
2093 E. Delmont Drive
Salt Lake City, UT 84117

John E. Ritter
University of Massachusetts
Mechanical Engineering Department
Amherst, MA 01003

W. Eric Roberts
Advanced Ceramic Technology, Inc.
990 "F" Enterprise Street
Orange, CA 92667

Barry Rossing
Lanxide Corporation
P.O. Box 6077
Newark, DE 19714-6077

Robert Ruh
Wright Laboratory
WL/MLLM
Wright-Patterson AFB, OH 45433

Jon A. Salem
NASA Lewis Research Center
21000 Brookpark Road
Cleveland, OH 44135

W. A. Sanders
NASA Lewis Research Center
21000 Brookpark Road
Cleveland, OH 44135

J. Sankar
North Carolina A&T State Univ.
Dept. of Mechanical Engineering
Greensboro, NC 27406

Yasushi Sato
NGK Spark Plugs (U.S.A.), Inc.
1200 Business Center Drive, #300
Mt. Prospect, IL 60056

Maxine L. Savitz
AlliedSignal, Inc.
Ceramic Components
P.O. Box 2960, MS:T21
Torrance, CA 90509-2960

David W. Scanlon
Instron Corporation
100 Royall Street
Canton, MA 02021

James Schienle
AlliedSignal Engines
P.O. Box 52180, MS:1302-2P
Phoenix, AZ 85072-2180

Gary Schnittgrund
Rocketdyne, BA05
6633 Canoga Avenue
Canoga Park, CA 91303

Robert B. Schulz
U.S. Department of Energy
Office of Transportation Matls.
EE-34, Forrestal Building
Washington, DC 20585

Peter Schwarzkopf
SRI International
333 Ravenswood Avenue
Menlo Park, CA 94025

W. D. Scott
University of Washington
Materials Science Department
Mail Stop:FB10
Seattle, WA 98195

Thomas M. Sebestyen
U.S. Department of Energy
Advanced Propulsion Division
EE-322, Forrestal Building
Washington, DC 20585

Kish Seth
Ethyl Corporation
P.O. Box 341
Baton Rouge, LA 70821

Richard K. Shaltens
NASA Lewis Research Center
21000 Brookpark Road, MS:302-2
Cleveland, OH 44135

Dinesh K. Shetty
University of Utah
Materials Science and Engineering
Salt Lake City, UT 84112

Richard Silberglitt
FM Technologies, Inc.
10529-B Braddock Road
Fairfax, VA 22032

Mary Silverberg
Norton Company
SGNICC/NRDC
Goddard Road
Northboro, MA 01532-1545

Gurpreet Singh
Department of the Navy
Code 56X31
Washington, DC 20362-5101

Maurice J. Sinnott
University of Michigan
5106 IST Building
Ann Arbor, MI 48109-2099

John Skildum
3M Company
3M Center
Building 224-2S-25
St. Paul, MN 55144

Jay R. Smyth
AlliedSignal Engines
111 S. 34th Street, MS:503-412
Phoenix, AZ 85034

Boyd W. Sorenson
DuPont Lanxide Composites
1300 Marrows Road
Newark, DE 19711

Charles A. Sorrell
U.S. Department of Energy
Advanced Industrial Concepts
EE-232, Forrestal Building
Washington, DC 20585

Allen Spizzo
Hercules, Inc.
Hercules Plaza
Wilmington, DE 19894

Richard M. Spriggs
Alfred University
Center for Advanced Ceramic
Technology
Alfred, NY 14802

Charles Spuckler
NASA Lewis Research Center
21000 Brookpark Road, MS:5-11
Cleveland, OH 44135-3191

Gordon L. Starr
Cummins Engine Company, Inc.
P.O. Box 3005, Mail Code:50182
Columbus, IN 47202-3005

Tom Stillwagon
AlliedSignal, Inc.
Ceramic Components
P.O. Box 2960, MS:T21
Torrance, CA 90509-2960

Paul D. Stone
Dow Chemical USA
1776 "Eye" Street, N.W., #575
Washington, DC 20006

Thomas N. Strom
NASA Lewis Research Center
21000 Brookpark Road, MS:86-6
Cleveland, OH 44135

Willard H. Sutton
United Technologies Corporation
Silver Lane, MS:24
East Hartford, CT 06108

David F. Thompson
Corning Glass Works
SP-DV-02-1
Corning, NY 14831

T. Y. Tien
University of Michigan
Materials Science and Engineering
Dow Building
Ann Arbor, MI 48103

D. M. Tracey
Norton Company
SGNICC/NRDC
Goddard Road
Northboro, MA 01532-1545

Marc Tricard
Norton Company, WGTC
1 New Bond Street
Worcester, MA 01615-0008

W. T. Tucker
General Electric Company
P.O. Box 8, Bldg. K1-4C35
Schenectady, NY 12301

Donald L. Vaccari
Allison Gas Turbines
P.O. Box 420, Speed Code S49
Indianapolis, IN 46206-0420

John F. Vander Louw
3M Company
3M Center, Bldg. 60-1N-01
Saint Paul, MN 55144

Michael Vannier
Washington University, St. Louis
520 S. Kings Highway
St. Louis, MO 63110

V. Venkateswaran
Carborundum Company
Niagara Falls R&D Center
P.O. Box 832
Niagara Falls, NY 14302

John D. Volt
E. I. DuPont de Nemours & Co., Inc.
P.O. Box 80262
Wilmington, DE 19880

John B. Wachtman
Rutgers University
P.O. Box 909
Piscataway, NJ 08855

Shigetaka Wada
Toyota Central Research Labs
Nagakute Aichi, 480-11
JAPAN

Janet Wade
AlliedSignal Engines
P.O. Box 52180, MS:1303-2
Phoenix, AZ 85072-2180

Richard L. Wagner
Ceramic Technologies, Inc.
537 Turtle Creek South Dr., #24D
Indianapolis, IN 46227

Ron H. Walecki
AlliedSignal, Inc.
Ceramic Components
P.O. Box 2960, MS:T21
Torrance, CA 90509-2960

Robert M. Washburn
ASMT
11203 Colima Road
Whittier, CA 90604

Gerald Q. Weaver
Carborundum Speciality Products
42 Linus Allain Avenue
Gardner, MA 01440-2478

Kevin Webber
Toyota Technical Center, U.S.A.
1410 Woodridge, RR7
Ann Arbor, MI 48105

Karen E. Weber
Detroit Diesel Corporation
13400 Outer Drive
Detroit, MI 48239-4001

James K. Weddell
DuPont Lanxide Composites, Inc.
P.O. Box 6100
Newark, DE 19714-6100

R. W. Weeks
Argonne National Laboratory
MCT-212
9700 S. Cass Avenue
Argonne, IL 60439

James Wessel
Dow Corning Corporation
1800 "M" Street, N.W., #325 South
Washington, DC 20036

Thomas J. Whalen
1845 Cypress Pointe Court
Ann Arbor, MI 48108

Sheldon M. Wiederhorn
NIST
Building 223, Room A329
Gaithersburg, MD 20899

John F. Wright
Alfred University
McMahon Building
Alfred, NY 14802

D. S. Wilkinson
McMaster University
1280 Main Street, West
Hamilton Ontario L8S 4L7
CANADA

James C. Williams
General Electric Company
Engineering Materials Technology
One Neumann Way, Mail Drop:H85
Cincinnati, OH 45215-6301

Craig A. Willkens
Norton Company
SGNICC/NRDC
Goddard Road
Northboro, MA 01532-1545

Roger R. Wills
Ohio Aerospace Institute (OAI)
22800 Cedar Point Road
Brook Park, OH 44142

David Gordon Wilson
Massachusetts Institute of
Technology
77 Massachusetts Ave., Room 3-455
Cambridge, MA 02139

William T. Wintucky
NASA Lewis Research Center
Terrestrial Propulsion Office
21000 Brookpark Road, MS:86-6
Cleveland, OH 44135

Thomas J. Wissing
Eaton Corporation
Engineering and Research Center
P.O. Box 766
Southfield, MI 48037

James C. Withers
MER Corporation
7960 S. Kolb Road
Building F
Tucson, AZ 85706

Dale E. Wittmer
Southern Illinois University
Mechanical Engineering Department
Carbondale, IL 62901

Warren W. Wolf
Owens Corning Fiberglass
2790 Columbus Road, Route 16
Granville, OH 43023

Egan E. Wolff
Caterpillar, Inc.
Technical Center
P.O. Box 1875
Peoria, IL 61656-1875

George W. Wolter
Howmet Turbine Components Corp.
Technical Center
699 Benson Road
Whitehall, MI 49461

James C. Wood
NASA Lewis Research Center
21000 Brookpark Road, MS:86-6
Cleveland, OH 44135

John F. Wosinski
Corning, Inc.
ME-2 E-5 H8
Corning, NY 14830

Bernard J. Wrona
Advanced Composite Materials Corp.
1525 S. Buncombe Road
Greer, SC 29651

Carl C.M. Wu
Naval Research Laboratory
Ceramic Branch, Code 6373
Washington, DC 20375

John C. Wurst
University of Dayton Research Institute
300 College Park
Dayton, OH 45469-0101

Neil Wyant
ARCH Development Corp.
9700 S. Cass Avenue, Bldg. 202
Argonne, IL 60439

Roy Yamamoto
Texaco, Inc.
P.O. Box 509
Beacon, NY 12508-0509

John Yamanis
AlliedSignal Aerospace Company
P.O. Box 1021
Morristown, NJ 07962-1021

Harry C. Yeh
AlliedSignal, Inc.
Ceramic Components
P.O. Box 2960, MS:T21
Torrance, CA 90509-2960

Thomas M. Yonushonis
Cummins Engine Company, Inc.
P.O. Box 3005, Mail Code 50183
Columbus, IN 47202-3005

Thomas J. Yost
Corning, Inc.
Technical Products Div., 21-1-2
Corning, NY 14831

Jong Yung
Sundstrand Aviation Operations
4747 Harrison Avenue
Rockford, IL 61125

A. L. Zadoks
Caterpillar, Inc.
Technical Center, Building L
P.O. Box 1875
Peoria, IL 61656-1875

Avi Zangvil
University of Illinois
104 S. Goodwin Avenue
Urbana, IL 61801

Carl Zweben
General Electric Company
P.O. Box 8555, VFSC/V4019
Philadelphia, PA 19101

Department of Energy
Oak Ridge Operations Office
Asst. Manager for Energy
Research and Development
P.O. Box 2001
Oak Ridge, TN 37831-8600

Department of Energy
Office of Scientific and
Technical Information
Office of Information Services
P.O. Box 62
Oak Ridge, TN 37831